Nanostructured Electroactive Polymeric Composites for Energy Storage and Separation Applications

By

Wenda Tian

B.S. Chemical Engineering, University of California, Berkeley, 2011

M.S. Chemical Engineering Practice, Massachusetts Institute of Technology, 2014

Submitted to the Department of Chemical Engineering

in partial fulfillment of the requirements for the degree of

Doctor of Philosophy in Chemical Engineering

at the

MASSACHUSETTS INSTITUTE OF TECHNOLOGY

June 2018

Signature redacted

Signature of Author.....
Department of Chemical Engineering
May 2, 2018

Signature redacted

Certified by.....
T. Alan Hatton
Ralph Landau Professor of Chemical Engineering
Thesis Supervisor

Signature redacted

Certified by.....
Gregory C. Rutledge
Lammot du Pont Professor of Chemical Engineering
Thesis Supervisor

Signature redacted

Accepted by.....
Patrick S. Doyle
Singapore Research Professor of Chemical Engineering
Chairman, Committee for Graduate Student

Nanostructured Electroactive Polymeric Composites for Energy Storage and Separation Applications

Wenda Tian

Submitted to the Department of Chemical Engineering

in partial fulfillment of the requirements for the degree of

Doctor of Philosophy in Chemical Engineering

Abstract

Electroactive polymeric materials have garnered considerable interest due to their potential applications in advancing electrochemical energy storage, sensing, catalysis, and separations systems. Electroactive polymers include conducting polymers with π-conjugated backbones and redox polymers with localized redox-responsive moieties. The electro-responsive property of both conjugated and redox polymers is highly impacted by the efficient transport of counter-ions within polymers to maintain charge neutrality. The interactions at the molecular interface between the polymer and target entities ultimately dictate the performance of electroactive materials in the aforementioned applications. Nanostructures provide a shortened diffusion path for the transport of electrolyte ions or target molecules during a reversible redox process. The large interfacial area arising from an improved morphology allows efficient utilization of polymeric materials. Consequently, the union of nanostructures and electro–responsiveness has proven to be a powerful strategy to enhance the merit of electroactive polymers in the design of next generation energy storage devices, sensors, catalysts and separation platforms.

In this thesis, we focused on developing novel synthesis strategies for nanostructured electroactive polymeric composites. Two different synthesis approaches for the polymeric component were realized by exploiting the inter-molecular interactions between monomeric units and other entities during an electrochemical polymerization process. In the first approach, a nanostructured polyvinylferrocene /polypyrrole hybrid was fabricated via a co-deposition method as a result of the π-π stacking interactions between the aromatic pyrrole monomers and the metallocene moieties of polyvinylferrocene. The hybrid has a highly porous morphology with a significantly increased surface area compared to its bulk counterpart. The synergistic effects between polyvinylferrocene and polypyrrole lead to enhanced ionic and electronic conductivity and, consequently, a higher specific capacitance as a supercapacitor electrode material.

The second approach was a diffusion-controlled electrochemical method facilitated by the interactions between pyrrole monomers and the carbamate groups in CO_2-bound polyamines. As a result, a porous polypyrrole coating consisting of nanofibrous structures was synthesized and deposited on a carbon microfiber substrate. This composite material demonstrated enhanced electrochemical properties and adsorption capability towards aldehydes as a result of its porous morphology and high surface area. We later applied this composite material in achieving electrochemically modulated adsorption of polynucleotides. The adsorption process was found to have a strong dependence on the oxidation states of the composite due to the electrostatic interactions between positively charged polypyrrole backbones and negatively charged phosphate groups in DNAs.

Thesis Supervisor: T. Alan Hatton
Title: Ralph Landau Professor of Chemical Engineering,
Director, David. H. Koch School of Chemical Engineering Practice

Thesis Supervisor: Gregory C. Rutledge
Title: Lammot du Pont Professor of Chemical Engineering

Acknowledgements

My time at MIT will forever be most memorable because of the people who inspired and supported me.

First and foremost, with tremendous gratitude, I'd like to thank my thesis advisors, Prof. T. Alan Hatton and Prof. Gregory C. Rutledge. With his heartfelt warmth, Alan has given me unwavering support in my explorative research directions. His mentoring philosophy and patience allowed me to learn through failing and pivoting, and to eventually develop independence as a scientific researcher. Throughout my PhD study, Greg constantly challenged me to question research problems to a greater depth and provided me the needed clarity in untangling the most intriguing problems at hand. His genuine passion in solving scientific problems has truly inspired me to stay scrupulous in scientific investigation and remain ingenuously curious in life.

I would also like to sincerely thank my thesis committee members, Prof. Fikile Richard Brushett and Prof. Bradley Olsen for their scientific insight and guidance throughout my PhD study. The discussions with them have always been enlightening and tremendously helpful in shaping the direction of this thesis.

The start of my PhD research would have been significantly harder without Xianwen Mao, who has been both an exceptional mentor and a fun friend. Xianwen gave selflessly of his time to teach me various laboratory techniques and inspired me to always remain optimistic and motivated. I was also extremely privileged to work with colleagues from two research groups and benefitted immensely from their wealth of expertise. My thesis would not have been possible without the help of my collaborators and friends, Paul Brown, Andong Liu, Xiao Su, Yinying Ren, Tonghan Gu, and Takuya Harada, who represent only a small number of the people that made my time at MIT a truly humbling experience.

I'd like to also thank Bill DiNatale and Steven Kooi from ISN for going out of their way to assist with my experiments. The completion of my thesis work has been due in no small part to their help. A big thank you to Beth Tuths and Gwen Wilcox who have been incredible in providing the administrative help during my time at MIT.

Last but not least, I owe my success in completing my dissertation to my family. I would not have been here without my grandparents and uncle, who undoubtedly shaped my value and personality. My parents have unconditionally made sacrifices in supporting me in pursuing my interests. My husband has been the tireless champion throughout graduate school. The birth of my daughter gave me an opportunity to appreciate deeply the meaning of life, love, and sacrifice.

Table of Contents

List of Figures

List of Tables

Chapter 1. Introduction

1.1. Motivations and Thesis Overview

Electroactive polymers are a class of functional polymers with π-conjugated backbones or redox-active groups, and therefore possess unique electro-responsive properties that draw great interests in the scientific community. By applying an electrical stimulus, a wealth of properties within such polymers, such as charge property, conductivity, electric field, molecular structure, and ion/electronic transport process, can be easily modulated. The electro-responsive properties allow electroactive polymers to be widely and extensively studied for applications in energy storage[1], sensing[2], and separations.[3]

Among materials used in energy storage, the π-conjugated backbones or redox centers in electroactive polymers can undergo fast Faradic reactions by accepting or loosing electrons upon oxidation or reduction, resulting in an excellent charge storage capability. Therefore, supercapacitors with electroactive polymer-modified electrodes can achieve a higher energy density compare to electrochemical double layer capacitors. As organic polymeric materials, electroactive polymers also offer the advantages of design flexibility, structural diversity, and easy synthesis methods, which render electroactive polymers as a superior alternative to other electrode material, such as metal oxides and doped carbonaceous materials.

Electroactive polymers have also been widely used in separation and sensing technologies by relying on their specific interactions with target molecules and transducing properties. The ion-exchange properties of conducting polymer were applied in separating ionic compounds.[4] The tunable charge properties allow redox polymers to be used as a redox-responsive platform for separating organics,[5] ionic species,[6] and proteins.[7] The induced changes in electronic, optical and

magnetic properties by adsorbed molecules enable conducting polymers to detect analytes at low concentrations in a liquid or gas environment.[2a]

The electro-responsive properties of those polymers largely depend on their interactions with the environment. The organic polymeric nature allows small molecules and ions to diffuse within electroactive polymer bulk. Nanostructured polymeric materials possess large surface areas and shortened transport pathways, and therefore can interact efficiently with other species. In the case of pseudocapacitors, a large surface area gives a large polymer/electrolyte interface, allowing a higher utilization of the electroactive material. The shortened transport pathway can reduce ion diffusion limitations and increase the access to electrolyte ions. The advantages of nanostructured morphology were even more prominent in separations. The adsorption of target species largely depends on their accessibility to the adsorption sites at the interface. Consequently, developing a simple and versatile nanostructuring approach for electro-active polymers plays a paramount role in its advancement for removing target contaminants of environment and biological interests.

Despite the crucial role polymer morphology plays in various applications, current nanostructuring strategies for electroactive polymers have inherent limitations. Methods involving hard or soft templates are commonly adopted, but suffer time-consuming and labor-intensive template removal process. Nanostructures can also be altered under those harsh post-synthesis treatments. From this particular angle, my thesis aims to develop novel nanostructuring methods for electroactive polymer composites by exploiting synergistic effects and interactions between monomeric molecules and other entities in the electrochemical polymerization process. The effects of morphological changes on polymer performance in energy storage and separations were also studied. In particular, the engineering and nanostructuring of electroactive polymer materials were explored in three directions. I firstly aimed to develop polymer materials with improved

morphology through a simple electrochemical method. We achieved this by exploiting the synergistic effects between conducting polymers and redox polymers to fabricate a highly porous polyvinylferrocene (PVF)/polypyrrole (PPy) hybrid with significantly improved electrochemical performance. However, the presence of heavy metals in the polymer hybrid and the use of organic solvents posed restrictions on applying the PVF/PPy hybrid in separation applications of environmental and biological interests. Therefore, my second goal was to developed an aqueous nanostructuring strategy for metal-free electroactive polymers. This was achieved by developing a multiphase-diffusion-controlled synthesis approach by relying on the interactions between pyrrole monomers and the carbamate groups in CO_2-bound polyamines. As a result, a porous PPy film consisting of nanofibrous structures was synthesized. Lastly, we focused on engineering the conductive deposition substrate by incorporating electrospun carbon nanofibers (ECNFs). The conductive substrate serves as both a working electrode and an initiator in electrochemical polymerizations, and, as a consequence, plays a decisive role in the advancement of electroactive polymer composites. We adopted electrospinning and subsequent thermal treatments to fabricate ECNFs. A simple dip-coating method was developed to construct an ECNF/carbon microfiber (CMF) composite.

The objectives of my thesis are thereupon outlined as:

1) Develop a facile approach to synthesize nanostructured conducting polymer/redox polymer hybrid. The synergistic effects between PVF and PPy were exploited to improve the electrochemical properties of the hybrid.
2) Develop an aqueous synthesis approach for fabricating nanostructured metal-free conducting polymer materials. We focused on developing a diffusion-controlled method to fabricate a porous coatings consisting of polypyrrole nanofibers.

3) Engineer the structure of carbon substrates by introducing carbon nanofiber materials.
4) Evaluate the performance of the nanostructured PVF/PPy hybrid as an electrode material for supercapacitors. Study the effect of morphological changes on the properties and performance of porous PPy film in adsorption towards neutral and charged molecules.

1.2. Introduction to Electroactive Polymers

Electroactive polymers possess molecular structures that enable responsiveness to an electrochemical stimulus. This unique property stems from either a π-conjugated backbone or localized redox groups, and have attracted great interests in the design and engineering of electroactive polymers. Two main categories of electroactive polymers are conducting polymers and redox polymers. Conducting polymers are a group of polymeric materials containing π-conjugated backbones. The conjugated molecular structure can carry and delocalize positively charged defects or negatively charged electrons through a process called doping. The molecular structures of commonly studied conducting polymers are listed in ***Figure 1-1*****Figure 1-1**. Depending on the doping level, the conductivity can range from 10^{-10} S/cm to 10^{4} S/cm.[8] When undoped, neutral conjugated polymers have a conductivity in the low range of 10^{-10} S/cm to 10^{-5} S/cm.[8] When reduced or oxidized, the reversible doping process introduces negative or positive charges into the conducting polymer backbone. The charge carriers are transported within the polymer by delocalizing along the conjugated backbones. Simultaneously, counter-ions with opposite charges diffuse into the polymer to maintain charge neutrality (**Figure 1-2**). The conductivity can be increased to 1 to 10^{4} S/cm.[9] In this fashion, conducting polymers can be reversibly switched into insulators, semiconductor, and conductors. The insertion and release of ions during the reversible doping process can lead to the swelling and de-swelling of conducting

polymers. The control of the volume change by an electrochemical stimuli renders conducting polymers as suitable materials for artificial muscles[10] and actuators.[11] In addition to its tunable conductivity, conducting polymers also possess the advantages of traditional polymers, such as easy synthesis, excellent durability, low weight, low cost, structural diversity and flexibility.

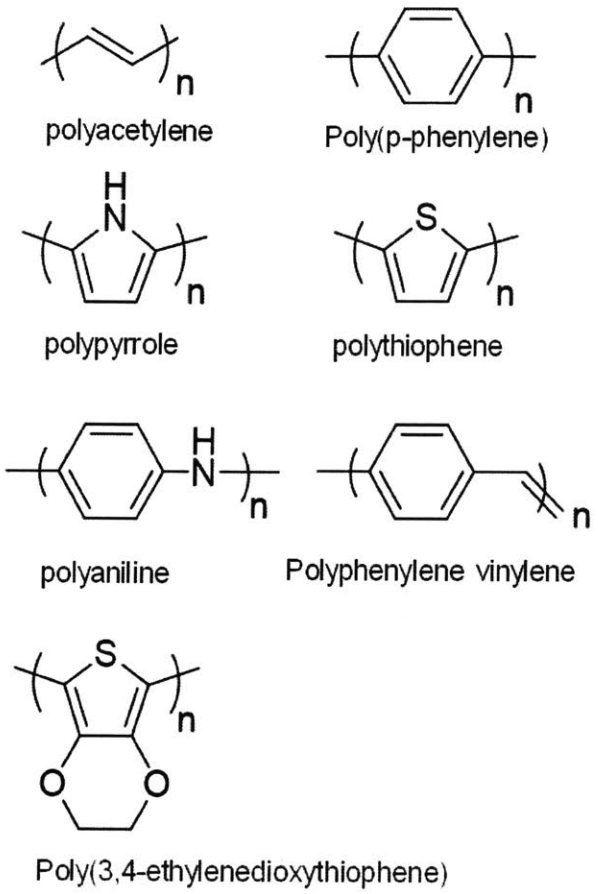

Figure 1-1. The molecular structures of commonly studied conducting polymers.

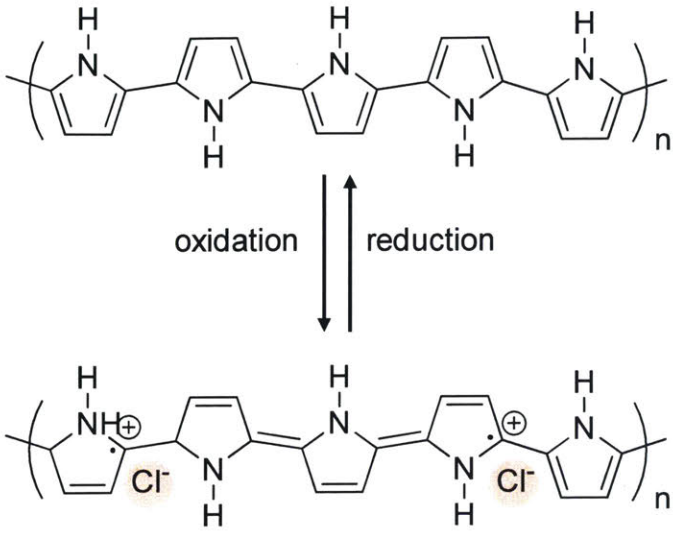

Figure 1-2. Schematic shows the oxidation of conducting polymers results in the doping of the conjugated backbone and the inserting of counter ions (Cl^-).

In contrast to conducting polymers, the electroactive properties of redox polymers are due to the redox-responsive groups or sites that are spatially and electrostatically localized and isolated. The redox –responsive groups can be oxidized (loosing electrons) or reduced (accepting electrons). Electron transfer in redox polymers undergoes a different charge propagation mode. Instead of being delocalized along the backbone, electrons are transported via a much slower hopping mechanism between neighboring redox centers. Therefore, redox polymers have low intrinsic conductivity and cannot be easily synthesized via electrochemical polymerization. The molecular structures of commonly studied redox polymers are shown in **Figure 1-3**.

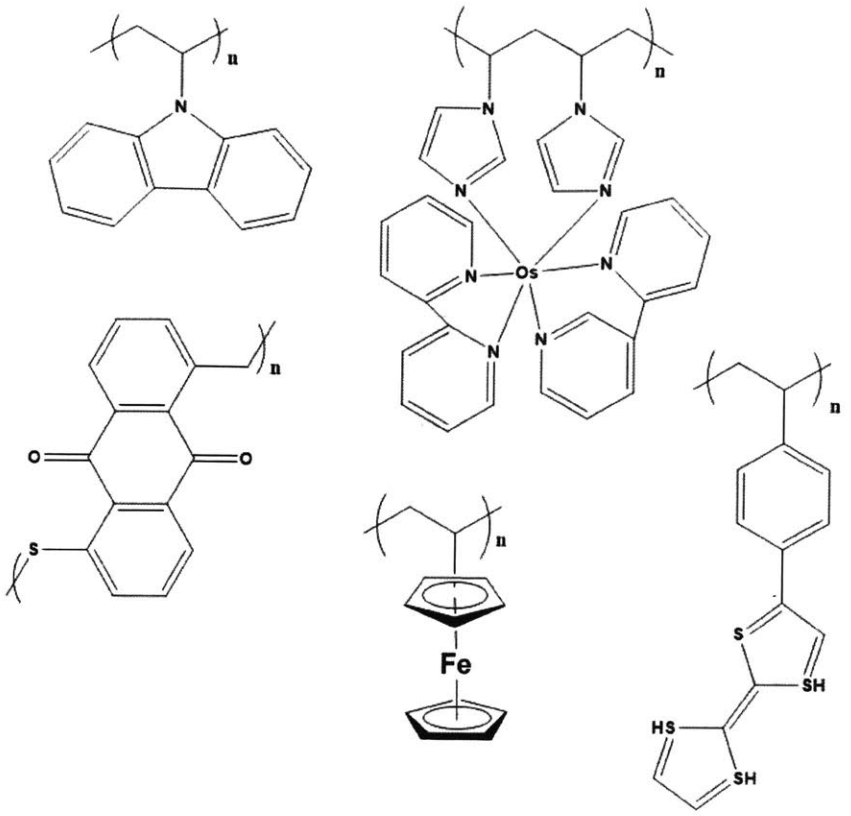

Figure 1-3. The molecular structures of commonly studied redox polymers.

1.3. Synthesis of Conducting Polymers

Conducting polymers can be easily synthesized via radical polymerization, involving an oxidative initiation, a chain propagation, and a termination step. For example, the polymerization of pyrrole starts with pyrrole monomers being oxidized and converted to pyrrole radical cations. The reactive radical can attack another pyrrole monomer to form a new radical, or couple with another radical to form a bipyrrole upon deprotonation.[12] The bipyrrole continues to grow by further oxidation and coupling with more radicals. Eventually, the polymerization ends with complete consumption of reactive radicals. The oxidation process can be initiated using a chemical

oxidizing agent, an applied electrochemical potential, or photochemical oxidation. Chemical oxidizing agents such as $FeCl_3$, $Fe_2(SO_4)_3$, phosphomolybdic, and potassium peroxidisulfate, were used in solution phase polymerization to form bulk conducting polymers. Electrochemical polymerization involves using a conductive material as the working electrode near which the oxidation of monomers occurs. The synthesized conducting polymers are often precipitate onto the conductive substrate as a thin film. The process parameters of electrochemical polymerization can be easily varied to control the properties of the formed polymer film, such as thickness, morphology, and conductivity. Because of the easy synthesis process of conducting polymers, nanostructuring and morphology optimization have been focused on this category of electroactive polymers.

1.4. Review of Strategies to Synthesize Conducting Polymer Nanostructures

Application of conducting polymers replies on their molecular interactions with specific target molecules in the external environment. Solid state conducting polymers generally allows permeation of small molecules into its bulk. The diffusion of molecules in bulk conducting polymers is often slow, therefore limiting such intermolecular interactions. When engineered into nanostructures, such as nanoparticles, nanofibers, nanowires, nanotubes[13] and nanospheres, conducting polymers can have large surface areas, shortened ion diffusion path, and high carrier mobility, leading to improved performance in various applications. The crucial role polymer morphology plays has resulted in extensive research efforts in developing nanoscale polymeric materials. Current nanostructuring methods include template methods involving either hard templates or soft templates, and template-free methods, such as mechanical stretching and electrospinning.

Hard templates are insoluble solid templates that are commonly made from anodized alumina,[14] opals,[15] and polycarbonate.[14b, 16] Hard templates are pre-engineered with high densities of pores or channels with a range of sizes. Precursors or monomers fill the pores before polymerization. Upon the introduction of a chemical oxidizing agent or a positive potential, monomers are polymerized into polymer nanostructures with shapes defined by the pores or channels of the template. This method allows complete control on the size, shape and orientation of the nanostructures. In addition to templates with pre-engineered pores, colloidal particles can be used as a hard template where polymers grow within the interstitial voids of assembled particles.[17] Soft templates typically are long range ordered structures made of polymer, surfactants,[18] micelles,[13, 19] polyacids,[20] *etc*. They were utilized to direct the growth of polymer nanowires, nanofibers, and nanotubes, by selectively controlling the self-assembly process driven by non-covalent interactions. Non-covalent interactions such as hydrophobic, π-π stacking, van der Waals, electrostatic interactions, and hydrogen bonding drive monomeric molecules to self-assemble into specific shapes. Upon oxidation, the nanostructures are preserved in the polymer form. In those template methods, post-synthesis purification is often required to remove the template material. Procedures that involve removing hard templates commonly require harsh conditions. The preservation of the formed nanostructure under those harsh conditions becomes another challenge. In cases where simple solvent wash can achieve removal of ionic template materials, the additional steps can become cost inhibitive in scale-up synthesis.

In addition to template synthesis approaches, various template-free methods have been developed. Uniform polyaniline nanofibers were fabricated through an aqueous/organic interfacial synthesis approach.[21] Polymer nanostructures can also grow from an existing nanostructure. Metal oxidized nanowires served as both the physical template and the chemical oxidative initiator to

seed the growth of conducting polymer 1D nanostructures.[22] Physical methods, such as mechanical stretching[23] and electrospinning[24] were utilized to make polyaniline nanofibers.

1.5. Introduction to Electrospinning as a Polymer Nanofiber Fabrication Technique

Electrospinning is a versatile and robust electrostatic fiber fabrication method based on applying a strong electric field on polymer solutions or melts to generate fibers with diameters in the submicron to nanometer range. The versatility of this technique allows it to produce a great variety of polymeric fibers by using various polymer precursors. The simplicity of the process enables the easy optimization and customization of the spin conditions. Process parameters, such as applied potential, electrospinning setup design, flow rate, *etc.*, have been studied to generate fiber mats with various properties. During electrospinning, a polymer precursor blend is extruded through a metal needle via a syringe pump. Charges are introduced to the polymer blend by an applied high electric potential. The strong electrical repulsive forces introduced by the charges eventually overcome the surface tension in the charged polymer solution or melt. As a result, a charged jet of polymer blend ejects from the tip of the Taylor cone and is accelerated and stretched while undergoing a whipping motion towards the grounded collector plate.[25] During the process, the solvent of polymer precursor evaporates and leaves only polymer fibers, forming a porous non-woven mat.

The small diameters and high surface areas of electrospun polymer fiber mats provide advantages for their applications in tissue engineering,[26] filtration,[27] and drug delivery.[28] Electrospun polymer fibers can be converted to carbon nanofibers via subsequent thermal treatments. Electrospun carbon fibers fabricated via this approach were widely used in energy

storage and biosensing.[29] The thermal treatment process consists of a stabilization and a carbonization step. The stabilization step involves heating the polymer fiber samples to between 200 °C and 300 °C in air. Subsequent carbonization heats the sample up to 2800 °C under an inert gas, such as nitrogen or argon.

Chapter 2. An Electrochemical Co-Deposition Strategy for Synthesizing Nanostructured Conducting Polymer/Redox Polymer Hybrid with Synergy for Energy Storage

The work reported in this thesis chapter was previously published as "Electrochemically Nanostructured Polyvinylferrocene / Polypyrrole Hybrids with Synergy for Energy Storage", by Wenda Tian, Xianwen Mao, Paul Brown, Gregory C. Rutledge, and T. Alan Hatton. It was adapted with permission from Advanced Functional Materials (2015).

Unconjugated redox polymers, such as polyvinylferrocene (PVF), have rarely been used for energy storage due to their low intrinsic conductivity. Conducting polymers with conjugated backbones, though conductive, may suffer from insufficient exposure to the electrolyte due to the often formed non-porous structures. The work present in this chapter overcomes this limitation via simultaneous electro-polymerization of pyrrole and electro-precipitation of PVF on electrode surfaces. This synthesis method relies on the π-π stacking interactions between the aromatic pyrrole monomers and the metallocene moieties of PVF. This fabrication process results in a highly porous polymer film, which enhances the ion accessibility to polypyrrole (PPy). PPy serves as a "molecular wire", improving the electronic conductivity of the hybrid and the utilization efficiency of ferrocene. The PVF/PPy hybrid exhibited a specific capacitance of 514.1 F g^{-1}, which significantly exceeds those of PPy (27.3 F g^{-1}) and PVF (79.0 F g^{-1}), respectively. This approach offers an alternative to nanocarbon materials for improving the electronic conductivity of polymer hybrids, and suggests a new strategy for fabricating nanostructured polymer hybrids. This strategy can potentially be applied to various polymers with π-conjugated backbones and redox polymers with metallocene moieties for applications such as energy storage, sensing, and catalysis.

2.1. Introduction

Driven by the staggering demands for sustainable and efficient energy storage solutions, extensive research efforts have focused on the furtherance of pseudocapacitors with high power density to bridge the gap between batteries and dielectric capacitors.[30] Instead of relying only on ion adsorption at the electrode surface, pseudocapacitors store charges via fast reversible surface/near-surface redox reactions, typical of electroactive materials such as metal oxides and conducting polymers.[30b] Redox polymers with non-conjugated backbones such as polyvinylferrocene (PVF) are localized-state conductors[31] with discrete electron donor/acceptor sites. Electron hopping between neighboring redox centers on PVF, for instance, can induce redox reactions under an electrochemical stimulus. Despite its stable one-electron redox electrochemistry, flat charge/discharge profile, and electrochemical reversibility, PVF has not been widely reported as a medium for energy storage applications, for two reasons. First, the diffusion-like[32] electron transport mechanism in PVF renders a poor intrinsic conductivity of only 10^{-5}-10^{-7} S cm^{-1}.[33] Second, while close packing of polymers can increase the redox center concentration and hence reduce the inter-site distance for fast electron hopping, it usually also results in a nonporous structure with limited polymer/electrolyte interface that hinders ion diffusion.[32d] The compromise between electronic and ionic conductivity lowers the redox center utilization efficiency and makes it challenging to achieve the theoretical specific capacitance.[32c] In only a handful of efforts to date have attempts been made to address this limitation, by incorporating conductive nanocarbon materials into PVF films. It was found that the introduction of dispersed graphite powders can increase the electronic conductivity of PVF-modified electrodes, with a resulting high charge capacity of 126.4 mAh g^{-1}.[34] Mao *et al.* combined carbon nanotubes with PVF to increase the utilization efficiency of ferrocene and achieved a specific capacitance of 418.8 F g^{-1}.[35] In contrast

to PVF, whose non-conjugated backbone mainly serves as an insulated structural support, conducting polymers such as polypyrrole (PPy) allow charge transport along their extensively conjugated backbones via doping/de-doping.[31b, 36] In particular, PPy is electroactive over the redox potential range of PVF, with an intrinsic conductivity routinely above 10 S cm^{-1}.[37] Conducting polymers also offer great design flexibility and are easy to prepare, low cost, light weight, and sustainable.[38] With PPy as the conductive medium, neither surfactants nor additional sonication steps are required for dispersing precursors, such as graphite powders or carbon nanotubes prior to functionalization of the electrodes, which allows the fabrication process to be achieved in a single step, and to be readily scalable. However, a major limitation of using a bulk conducting polymer directly is insufficient exposure to the electrolyte solution due to the non-porous structure that is often formed. Previous efforts to engineer polymers into nanoporous structures have often involved multiple steps, where sacrificial materials used during polymerization are subsequently removed to introduce porosity.[39]

Here we report a facile synthesis strategy for the preparation of a highly porous electroactive hybrid in which we exploit the π-π stacking interactions between pyrrole and the ferrocene moieties of PVF. In this hybrid, PPy chains serve as molecular wires for the spatially isolated ferrocene moieties, increasing the utilization efficiency of ferrocene. PPy also increases the charge storage capacity via redox reactions in its bulk. This approach addresses the challenges to achieve a high specific capacitance with PVF, and offers an alternative to conventional nanocarbon materials for improving the electronic conductivity of polymer hybrids. This new strategy for fabricating nanoporous polymer hybrids via exploiting the intermolecular interactions between constituent molecules can potentially be applied to a variety of conducting polymers with π-conjugated backbones and redox polymers with various metallocene moieties.[40]

2.2. Results and Discussion

2.2.1. Morphological Characterization

Polymer modified electrodes were fabricated with commercial carbon fiber papers as the substrate. Although limited in surface area compared to carbon nanofibers, commercial carbon fiber papers are convenient, provide a relatively greater surface area for polymer deposition as compared to flat sheets, and maintain a porous electrode architecture at a large scale. The various electrodes prepared in this work are identified using the nomenclature "substrate"-"deposited polymer"; for example, CF-PVF refers to electrodes comprising PVF deposited on carbon fibers (CF). For simplicity, CF-Codep refers to the electrodes comprising PVF and PPy co-deposited on carbon fibers. Pristine carbon fibers showed clean surfaces with longitudinal striation patterns characteristic of Toray fibers (**Figure 2-1a**). Pyrrole in solution, upon oxidation, can undergo oxidative polymerization to form PPy (**Figure 2-1b**). The electrochemically polymerized PPy formed a segmented and densely grown film on each carbon fiber (**Figure 2-1c, d**). This morphology was consistent with the homogenous, closely packed, and globular-shaped structure of PPy reported previously.[41] Ferrocene units in PVF can be oxidized to ferrocenium under an appropriate electrochemical potential. The induced positive charge on ferrocenium increases the hydrophilicity of the polymer chain, driving PVF to precipitate onto the carbon fibers from the hydrophobic organic solvent (**Figure 2-1e**).[42] This electro-precipitated PVF coated each carbon fiber conformally and exhibited a nonporous, but relatively rough, morphology (**Figure 2-1f, g**). In contrast to the pure PVF or PPy polymer films, the polymer hybrid fabricated via simultaneous electro-deposition and electro-precipitation (**Figure 2-1h**) had a highly porous film structure (**Figure 2-1i, j**). This interconnected porous morphology was observed consistently throughout the entire carbon fiber framework (**Figure 2-1i**). A close examination via HR-SEM revealed that the

co-deposited film consisted of nanoscale polymeric spherical clusters with diameters of 50-100 nm (**Figure 2-1k**). These nanospheres adhered randomly to each other, forming an interconnected porous film with carbon fibers as the retaining framework. Within the polymer/carbon fiber composite, a dual scale porosity was observed, consisting of nano-sized pores within the polymer film and micropores between the fibers. This morphology provided a large interfacial area between the polymer and the electrolyte, which facilitated diffusion of ions and rendered excellent electrochemical properties. To confirm that this dual scale porous morphology was indeed a result of the co-deposition process, sequentially deposited bilayer polymer films were fabricated. CF-PVF/PPy, with PVF as the inner layer and PPy as the outer layer, had a grainy and nonporous surface morphology, resulting from the thick outer layer of PPy **(Figure 2-10a)**. In comparison, the CF-PPy/PVF fabricated via the opposite order of deposition exhibited more roughness at the surface, while maintaining its dense film structure (**Figure 2-10b**). The different morphological properties of the hybrid and bilayer polymer films were due to the two different electro-deposition processes, and motivated our detailed investigation of the co-deposition process (see section 2.6).

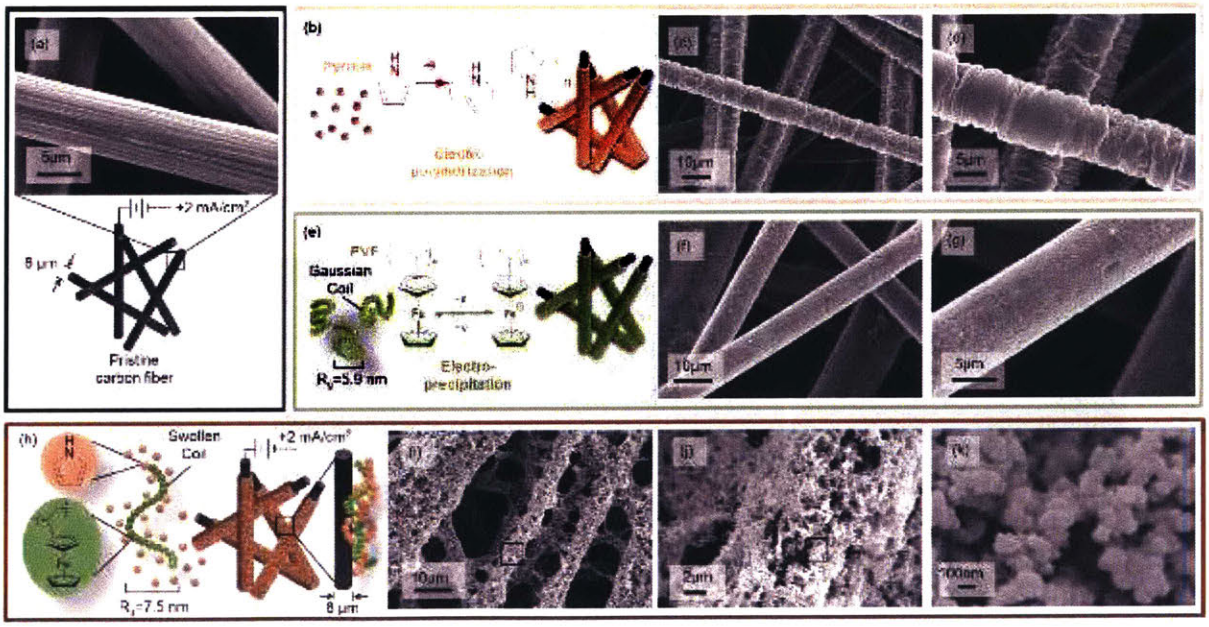

Figure 2-1. (a) Schematic and SEM image of the pristine carbon fibers, indicating their clean surfaces with striation patterns. Schematic (b) and SEM images (c, d: different magnifications) of the electro-polymerized pyrrole show the nonporous conformal coating of PPy films on each carbon fiber. Schematic (e) and SEM images (f, g) of the electro-precipitated PVF show that the formed PVF film had a rough and nonporous morphology. Schematic (h) and SEM images (i, j, k) of the co-deposited coatings of PVF and PPy on carbon fibers demonstrate the highly porous film structure resulting from this fabrication method.

Transmission electron microscopy (TEM) was used to confirm the relatively uniform distribution of the ferrocene units within the co-deposited hybrid film. **Figure 2-2a** shows the crystalline regions characteristic of pure PPy, the formation of which is attributed to the π–π interactions between adjacent PPy chains.[43] In pure PVF, the ferrocene moieties are observed as distinct black clusters with diameters ranging from 2 nm to 5 nm sitting atop a thin background layer of unclustered PVF (**Figure 2-2b**). In contrast to the morphologies of pure PPy and pure PVF, the crystalline regions and dark spheres are replaced by large grey areas in the co-deposited polymer hybrid (**Figure 2-2c**). This morphological difference suggests that the ferrocene moieties were more homogenously distributed within the hybrid.

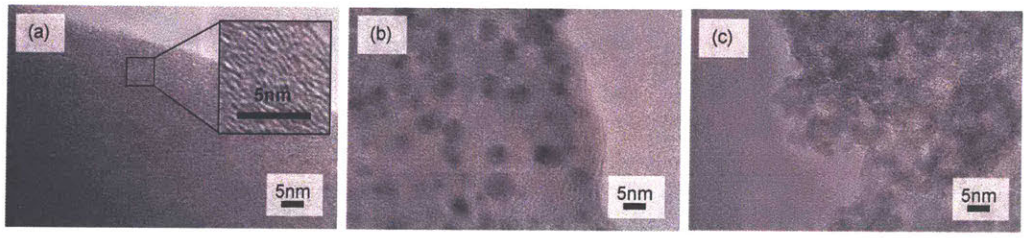

Figure 2-2. TEM images of electrochemically deposited (a) PPy, (b) PVF, and (c) co-deposited hybrid polymer film. The molar ratio of ferrocene to pyrrole units is about 5-6%, based on composition of the deposition solution and confirmation by XPS (see text).

Nitrogen adsorption was used to characterize the pore structure of the co-deposited polymer hybrid. The adsorption isotherm, or volume adsorbed versus relative pressure, P/P_0, where P_0 is the saturated vapor pressure, displayed a steep increase in slope at relative pressures above 0.8, and a hysteresis loop between the relative pressures of 1 and 0.8 on desorption (**Figure 2-3a**). This is a Type V isotherm according to the IUPAC classification, and indicates the presence of mesopores (2-50 nm)[44] within the polymer hybrid in which capillary condensation occurs at high P/P_0. The exhibited hysteresis is a result of the different pressures at which capillary condensation and capillary evaporation occur.[44] The specific surface area of the polymer hybrid obtained by the Brunauer–Emmett–Teller (BET) analysis is 166.8 $m^2 g^{-1}$, which is significantly higher than values reported for pure polypyrrole (37-61 $m^2 g^{-1}$),[45] such as polypyrrole porous clusters,[45a] tubes,[45a] nanoparticles,[45a] and thin films,[45d] or pure PVF powder (8 $m^2 g^{-1}$).[35] The pore size distribution based on the Barret–Joyner–Halenda (BJH) theory (**Figure 2-3b**) displays a broad peak in the region of 5-80 nm, with an average of 26.0 nm and a maximum at 33.0 nm. This broad distribution of pore sizes is consistent with the combination of mesopores (2-50 nm) and macropores (>50 nm) observed in the polymer hybrid under SEM. This broad distribution of pore sizes can potentially enhance ion access to the electroactive polymers and improve the power capability of the hybrid.

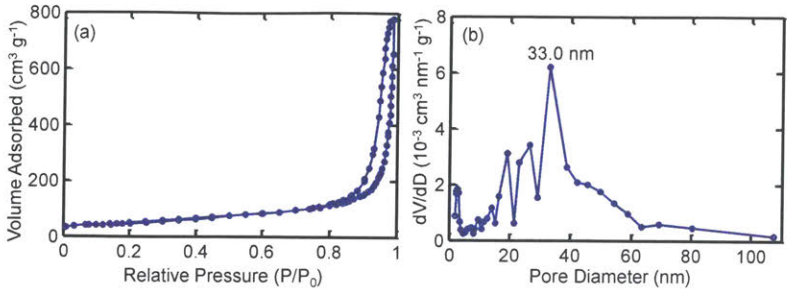

Figure 2-3. a) Nitrogen adsorption-desorption isotherms of the PVF/PPy polymer hybrid. b) The corresponding BJH pore-size distribution for the polymer hybrid.

2.2.2. Composition and Structure Characterizations

X-ray photoelectron spectroscopy (XPS) was performed to study the chemical composition of the polymer modified electrodes. Fe_{2p} and N_{1s} signals served as elemental markers for PVF and PPy, respectively. An XPS survey scan of the co-deposited polymer film indicated the presence of C_{1s}, O_{1s}, N_{1s}, Cl_{2p} and Fe_{2p} through their photoelectron peaks in the polymer films, in contrast to the pristine carbon paper where only a strong C_{1s} peak and a small O_{1s} peak were observed **(Figure 2-4a)**. The existence of the Fe_{2p} and N_{1s} peaks confirmed the deposition of both PVF and PPy on the substrate. The presence of Cl_{2p} and the increased O_{1s} signal were due to the dopant, ClO_4^-, in PPy. The high-resolution N_{1s} spectrum was deconvoluted into a main peak at 399.8 eV and a second peak at 402.2 eV (**Figure 2-4b**). These two peaks corresponded to the neutral -NH- nitrogens and the oxidized C-N^+ nitrogens, respectively, indicating that the polymerized PPy was partially oxidized.[39c, 41, 46] Fe_{2p} had two peaks from the spin-orbital splitting, $Fe_{2p,\,1/2}$ (721 eV) and $Fe_{2p,\,3/2}$ (708 eV), each of which was deconvoluted into two component peaks (**Figure 2-4c**). The two smaller component peaks of $Fe_{2p,\,1/2}$ and $Fe_{2p,\,3/2}$ at higher binding energies resulted from the partially oxidized ferroceniums.[47]

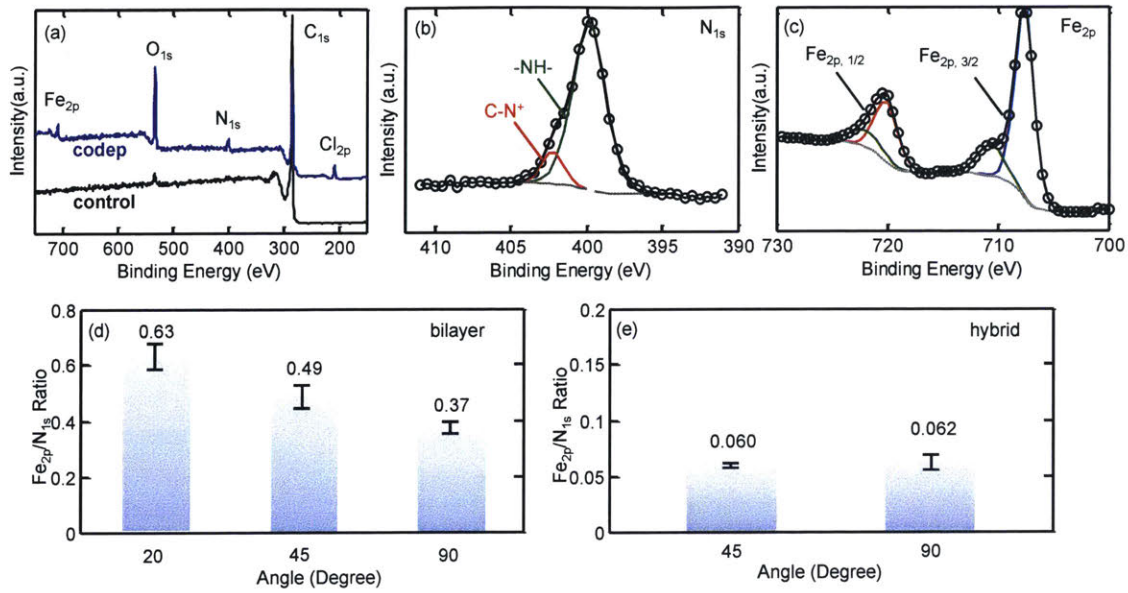

Figure 2-4. (a) Survey scans of the pristine carbon fiber paper (control) and co-deposited polymer hybrid indicated the presence of C_{1s}, O_{1s}, N_{1s}, Cl_{2p} and Fe_{2p}. High resolution scans of (b) N_{1s} and (c) Fe_{2p}. (d, e) Fe_{2p}/N_{1s} ratio obtained from angle-resolved XPS for CF-PPy/PVF bilayer and hybrid films, respectively, deposited on flat stainless steel sheets. The bilayer film showed a decreasing iron content with increasing depth, while a uniform distribution of ferrocene moieties within the co-deposited hybrid films was observed.

Angle-resolved XPS was used to probe the differences in depth profiles of chemical composition between sequentially-deposited and co-deposited polymer films. Since the local angle at the surface of a polymer-modified carbon fiber is difficult to determine and can be different from that of the sample holder relative to the XPS analyzer, we performed the angle-resolved XPS tests on polymer hybrid films deposited directly onto flat stainless steel sheets. The depth at which the composition was detected increased as the tilt angle increased. The peak intensity was used to

obtain the relative atomic concentration of each element. The Fe_{2p}/N_{1s} ratio, which measures the ratio of ferrocene to pyrrole units in the polymer hybrid, decreased with increasing tilt angles from 20 to 90 degrees, indicating that more PVF was deposited at the outer surface than in the inner layer of the polymer film for the PPy/PVF bilayer polymer film (**Figure 2-4d**). In the co-deposited polymer film, the ratio remained approximately the same throughout the analyzed depth, indicating that PVF was distributed uniformly within the polymer hybrid (**Figure 2-4e**). This observation is consistent with the conclusions drawn from TEM images. It is worth noting that, in the co-deposited polymer hybrid, the Fe_{2p} content was only ca. 6% of that of N_{1s}. This was consistent with the composition of the deposition solution, where the ratio of the molar concentration of ferrocene units to pyrrole monomer was ca. 5%.

2.2.3. Electrochemical Characterization in Three-Electrode Systems

The interesting morphologies of the PVF/PPy hybrids show promise for energy storage applications. First, we evaluated the electrochemical properties of the hybrids in three-electrode systems. The cyclic voltammetry (CV) profiles in **Figure 2-5a** indicate that the carbon fiber substrate contributed negligibly to the capacitance, while the electrochemically polymerized PPy film exhibited a quasi-rectangular CV curve within the voltage window of 0 to 0.7 V. This featureless profile resulted from the successive surface redox reactions of PPy films, indicating the perfect electrochemical capacitive behavior typical of PPy.[38b, 48] In contrast, the deposited PVF film exhibited distinct oxidation and reduction peaks at 0.35 V and 0.25 V, respectively.[34, 42] The CV curve for CF-PPy/PVF comprises both the broad quasi-rectangular profile from PPy and the pronounced anodic/cathodic peaks from PVF, indicating that PVF and PPy were both electroactive in the hybrid (**Figure 2-5b**). PPy as the inner layer was able to transport electrons effectively to the outer film of PVF, allowing two well-defined redox peaks similar to those in the pure PVF

films to develop. By contrast, the redox peaks in CF-PVF/PPy are barely discernible, presumably because the dense PPy outer layer limited ion diffusion to the ferrocene moieties in the inner layer (**Figure 2-2b**). CF-Codep displayed strong PVF redox peaks, and gave a much higher current response than did the other electrodes. The significant increase in the contributions of both polymer components to the specific capacitance indicated that the utilization efficiency of ferrocene and the ion accessibility to PPy were simultaneously improved upon forming the hybrid. The PVF/PPy hybrid also exhibited excellent rate performance. The specific capacitance of CF-Codep was much higher than that of the other electrodes, within the scan rate range of 0.001 V s^{-1} to 0.2 V s^{-1}, and remained at ~200 F g^{-1} even at 0.2 V s^{-1} (**Figure 2-5c**).

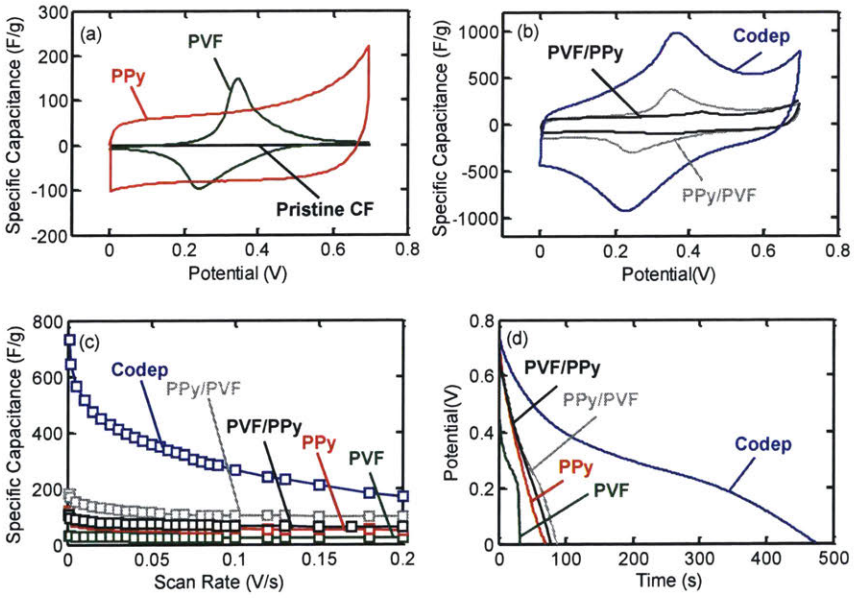

Figure 2-5. (a) The CV profiles of PPy and PVF compared to that of pristine carbon fibers. (b) The cyclic voltammetry profiles indicate the co-deposited polymer films gave a higher current response than the sequentially deposited polymer films. (c) The co-deposited polymer film shows

better rate performance at various scan rates of 0-0.2 V s^{-1}. (d) The galvanostatic discharge curves for various polymer modified electrodes at a current density of 1 A g^{-1}.

The excellent electrochemical properties of the polymer hybrids were also evident in the galvanostatic discharge profiles (**Figure 2-5d**). The discharge profile of PVF exhibited a sudden decrease in potential at short time (< 1 s), followed by an extended period (up to 30 s) where the potential decreased more slowly, as a result of the reduction of the ferrocenium to ferrocene. Upon complete reduction of all the ferrocenium units, the potential quickly plunged to zero.[34] In contrast, the curve for PPy was more linear, with no significant decrease in slope. This behavior arises because PPy has no defined redox potential within the potential window used, consistent with its featureless quasi-rectangular CV profile (**Figure 2-5a**). Both the bilayer (CF-PVF/PPy and CF-PPy/PVF) and the hybrid films deviated from a linear profile, with a decrease in the rate of change of potential at around 0.25 V. This "flattening" of the potential profile was a result of the redox reactions of the ferrocene centers. It is clear that the discharge profiles of the hybrid systems exhibited the characteristics of both PVF and PPy, but that the hybrid film displayed a much broader discharge profile than did the bilayer films, indicating a much larger charge storage capacity. A similar trend in charge storage capability was also observed in the comparison of CV profiles in Figure 5b.

Electrochemical storage capacity relies on the utilization efficiency of the redox units. In CF-PVF/PPy, PVF was deposited directly on the carbon fiber, beneath the densely grown PPy layer (**Figure 2-2a**); thus ions in the electrolyte had limited access to the PVF, which then could not be fully oxidized. This limitation manifested itself in the suppressed redox peaks in the CV profile (**Figure 2-5b**). In addition, the electron transport between PPy and the carbon fiber substrate was also compromised in this system, because the PVF backbone served mainly as an

insulating structural support and so electron transport occurred only by hopping of the electrons between the neighboring ferrocene centers. PVF permitted limited electron access to the outer-layer PPy, and thus the charge storage sites along the PPy chains were not utilized efficiently; this inefficiency ultimately resulted in the relatively low overall capacitance of 103.2 F g^{-1}. Though the ion diffusion limitation within CF-PPy/PVF was still expected, the inner polymer layer of PPy was conductive and could facilitate electron transport to the PVF. Therefore, CF-PPy/PVF exhibited the relatively higher specific capacitance of 144.1 F g^{-1}. The enhanced electrochemical performance of the co-deposited hybrid, as manifested by its specific capacitance of 514.1 F g^{-1}, was realized via the synergy between PVF and PPy. The charge delocalization along the backbone of PPy complemented the electron hopping between the redox moieties within the formed hybrid. Thus PPy chains served as "molecular wires" providing fast electron access to the isolated ferrocene moieties, which then could be efficiently oxidized and reduced. The highly porous nanostructure also increased the electrolyte-electrode interfacial contact area and ensured a high ionic conductivity by allowing easier ion diffusion within the films and facilitating the counter-ion insertion/extraction during the doping/dedoping of PPy and the redox reactions of the ferrocene moieties.

In addition, we also compared the performance of the PVF/PPy hybrid with a broad range of alternative supercapacitor electrode materials for energy storage applications, such as porous carbons and various inorganic electroactive species (**Table S1**). This comparison shows that the PVF/PPy hybrid has a higher specific capacitance than most of the recently reported carbon-based supercapacitor materials, such as corncob residue derived carbon,[49] nitrogen-containing carbon microspheres,[50] *etc.* This is due to the pseudocapacitance contribution from both PVF and PPy. Compared to the recently reported transition metal oxide/porous carbon composite materials,[51] the

PVF/PPy hybrid has a comparable or slightly higher specific capacitance. Different from metal oxide/carbon composites, the PVF/PPy hybrid is fabricated from a facile electrochemical co-deposition method, which can potentially be generalized to various other metallocene-containing polymers and conducting polymers. In addition, the hybrid polymer film can also be combined with various carbon nanomaterials, such as carbon nanotubes or graphene, to further improve its properties.

2.2.4. Two-electrode Symmetric Supercapacitor Device Performance

We also assessed the polymer hybrids in a two-electrode system that resembles the physical configuration in, and the operating conditions of, commercial packaged supercapacitors; our purpose in doing so was to provide a more meaningful measure of the material's performance for commercial applications.[52] **Figure 2-6a** compares the CV profiles of PVF, PPy, and the co-deposited PVF/PPy hybrid. The co-deposited hybrid gave a much larger current response than did the PVF and PPy films, and displayed a quasi-rectangular CV profile. The disappearance of redox peaks in the two-electrode configuration is commonly seen in electroactive polymers, for reasons that are as yet unclear.[52a, 52b] As the scan rate increased, the CV profiles for the co-deposited hybrid showed slight distortions from the quasi-rectangular shape, due to the increasing overpotential from the ion transport within the polymers (**Figure 2-6b**). The galvanostatic discharge curves (**Figure 2-6d, e**) indicated the much higher charge storage capacity of the hybrid polymer compared to those of pure PVF and pure PPy films. The calculated specific capacitance at various scan rates from 0.001-0.2 V s^{-1} and at various current densities from 0.06 to 10 A g^{-1} demonstrated the excellent rate performance of the co-deposited polymer film in the two-electrode cell (**Figure 2-6c, f**). The co-deposited PVF/PPy hybrid exhibited a specific capacitance of 345.3 F g^{-1}, which is significantly higher than that of either PVF or PPy (**Figure 2-6d**).

To gain further insight into the advantages of the co-deposited hybrid structure, electrochemical impedance spectroscopy (EIS) measurements were conducted on the two-electrode supercapacitor cells; the resulting Nyquist plots for CF-PVF, CF-PPy, and CF-Codep are shown in **Figure 2-7a**. Compared to CF-PVF or CF-PPy, CF-Codep exhibited a lower solution resistance (R_s, determined by the intercept on the Z_{re} axis) and a lower interfacial charge transfer resistance (R_{ct}, indicated by the diameter of the charge transfer semicircle or the length of the Warburg region).[53] Such decreases in R_s and R_{ct} further suggest that the ion diffusion resistance was reduced because of the formation of a porous structure and enhanced electron transport properties that result from incorporation of the conducting polymer component. The Coulombic efficiency was calculated to be 99.5% for the co-deposited polymer hybrid at a current density of 5 A g^{-1}. The power and energy densities determined from galvanostatic charge/discharge measurements in a two-electrode system are given in the Ragone plot shown in Figure 7b. This capacitor cell was characterized by a high energy density of 40.7 W h kg^{-1} at a power density of 6.79 kW kg^{-1}; the energy density decreased by only about 40% to 25 .4 W h kg^{-1} following a significant ~ 9-fold increase in the power density to 58.6 kW kg^{-1}. This enhanced power density at the expense of a relatively small decrease in energy density is attributed to the facilitated ion diffusion within the porous polymer films. The achieved maximum energy density is comparable to that of lead acid batteries (25-40 W h kg^{-1})[54] and much higher than that of activated carbon-based supercapacitors (4-5 W h kg^{-1}).[55] Compared to some of the recently reported conducting polymer-based supercapacitor devices,[53, 56] the PVF/PPy hybrid-based supercapacitor gives a higher energy density due to the additional pseudocapacitance offered by PVF.

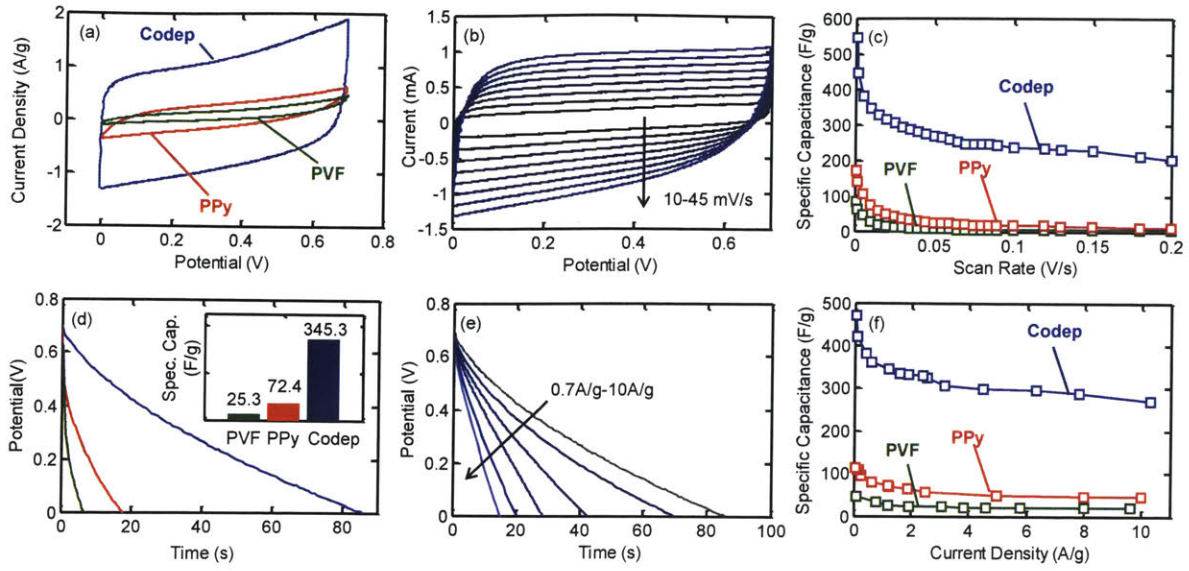

Figure 2-6. Electrochemical evaluation of the two-electrode configuration: (a) CV profiles for PPy, PVF and the co-deposited hybrid. (b) CV profiles for the co-deposited hybrid at scan rates from 10 to 45 mV s^{-1}. (c) The calculated specific capacitance at scan rates from 0.001 to 0.2 V s^{-1}. (d) The galvanostatic discharge curves recorded at 0.7 A g^{-1} and the calculated specific capacitance. (e) The galvanostatic discharge curves of the co-deposited PVF/PPy hybrid at current densities from 0.7 to 10 A g^{-1}. (f) The calculated specific capacitance of PVF, PPy, and the co-deposited hybrid at current densities from 0.06 to 10 A g^{-1}.

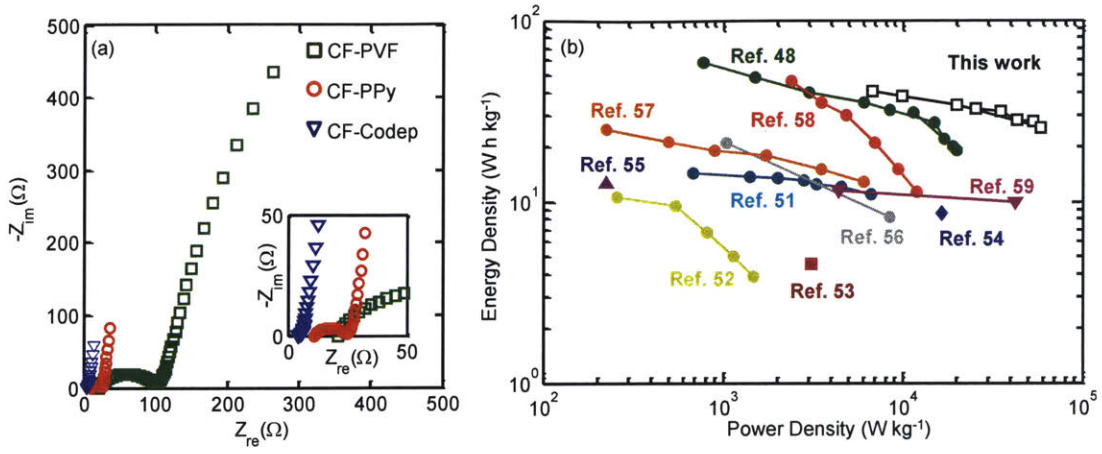

Figure 2-7. (a) Nyquist plots for CF-PVF, CF-PPy, and CF-Codep indicate lower solution and interfacial charge transfer resistances for the co-deposited polymer hybrids. (b) Ragone plot for the PVF/PPy polymer hybrid-based two-electrode symmetric supercapacitor performance relative to that of other conducing polymer-based supercapacitors reported in literature.[53, 56]

2.2.5. Cycling Stability

Conducting polymers usually have limited cycling stabilities due to repeated volumetric swelling and shrinking during charging/discharging.[30b, 57] The volume change and the resulting mechanical stress often lead to mechanical degradation and dissolution of polymer films,[58] as was also observed in the PVF/PPy polymer hybrid in this study. To address this cycling degradation issue, we utilized a hydrothermal process to deposit a thin layer of carbonaceous material on each of the hybrid clusters to mitigate the effects of the swelling and deswelling of the material during cyclic charging/discharging process.[57] In the hydrothermal process, glucose was converted under mild conditions to a nanometer-thick carbon shell coating the materials.[59] This method has been used to improve the stability of conducting polymers and metal oxides without compromising their

electrochemical performance.[59b, 60] The porous structure of the polymer hybrid was maintained during the hydrothermal coating process as observed by SEM, BET surface area, and pore size distribution (Figure 2-12a, b, d, e). XPS analysis on the PVF/PPy hybrid after the hydrothermal process indicated the presence of the carbon coating on the polymer surface (Figure 2-12g). **Figure 2-8a** compares the CV curves for the PVF/PPy hybrid observed in a 3-electrode system before and after the hydrothermal treatment. The deposition of the thin carbon shell resulted in a distorted CV profile, but with a slight increase in the capacitance due to the increased double layer effect from the carbon shells. EIS results and the calculated specific capacitance from both the CV and galvanostatic measurements (Figure 2-12f, h, i, j) confirmed that the electrochemical performance was not compromised by the hydrothermal process. The polymer hybrid retained 94.5% of its specific capacitance after 3000 cycles at 5 A g^{-1} (**Figure 2-8b**), and exhibited minor changes in its surface morphology after the cycling evaluation (Figure 2-12c).

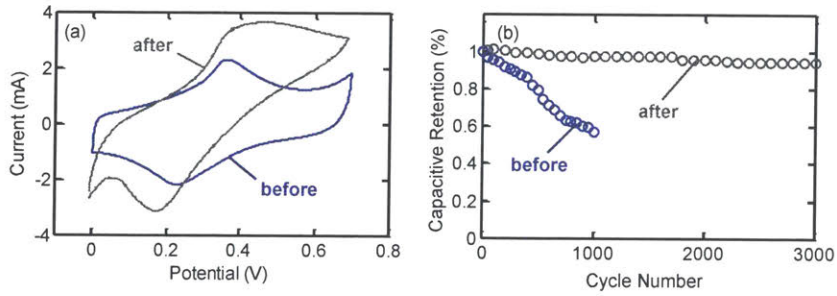

Figure 2-8. (a) The PVF/PPy hybrid electrode exhibited a more distorted CV profile after the hydrothermal process compared to that of the untreated electrode. (b) The cycling stability of the PVF/PPy hybrid modified electrode was significantly improved following the hydrothermal treatment, with retention of 94.5% of its specific capacitance at 5 A g^{-1} after 3000 cycles.

2.2.6. Molecular Interactions between Ferrocene and Pyrrole

The different surface morphology and enhanced electrochemical properties of the polymer hybrid relative to the sequentially deposited components was due to the influence of intermolecular interactions between the PVF and pyrrole molecules on the simultaneous electro-polymerization and electro-precipitation process. In the co-deposition solution, each PVF polymer chain was solvated partially by pyrrole because PVF-pyrrole interactions are more favorable than those between PVF and $CHCl_3$ due to the π-π stacking interactions. Upon electro-deposition of the swollen PVF coils, the solvating pyrrole molecules were in a position to be electro-polymerized to form polypyrrole; the PVF molecules were incorporated into and intimately associated with the PPy in the resulting film. The change in PVF polymer chain conformation in solution prior to deposition due to its interaction with pyrrole was revealed using small-angle neutron scattering (SANS) and UV-vis absorbance spectrometry. This intimate interaction between the two polymers within the formed hybrid was further elucidated via Fourier transform infrared spectroscopy (FTIR).

2.2.6.1 Small-angle neutron scattering (SANS)

Small-angle neutron scattering (SANS) was used to probe the conformation of the PVF polymer chains in solution. It is evident from the two different SANS profiles (scattering intensity $I(Q)$ vs. $Q \propto (2\theta/\lambda)\sin(2\theta)$, where θ is the scattering angle, and λ the radiation wavelength) shown in **Figure 2-9a** that PVF underwent conformational changes in the presence of pyrrole. Porod analysis confirmed this change by yielding information on the "fractal dimension" of the polymer coil.[61] In the high-Q region, the intensity was approximated as:

$$I(Q) = \frac{A}{Q^n} + B$$

For polymer coils, the Porod slope n was extracted by plotting log (I (Q)–B) vs. log (Q) (Figure 9), where B is the background. The exponent n is related to the excluded volume parameter ν by n = 1/ν; Gaussian, swollen, and collapsed coils have Porod slopes of 2, 5/3, and 3, respectively. For PVF in chloroform, we extracted an n value of 1.99, which is consistent with Θ conditions for the solution (ν = 0.5) and the Gaussian coil. However, when PVF was combined with pyrrole, n was found to be 1.67, indicating a transformation into swollen coils. This change in chain conformation was attributed to interactions between the PVF coils and pyrrole monomers, presumably through the π-π stacking. In this way, pyrrole monomers extended the PVF chains in solution, swelling the PVF coil. An increase in the measured radius of gyration (R_g) again confirmed the structural change of PVF in solution. To obtain R_g for the polymer, partial Zimm plots were prepared (Figure 9 inset).[61] Here, a Lorentzian form for the Q-dependence of the scattering intensity was assumed,

$$I(Q) = \frac{I_0}{1 + Q^2\zeta^2}$$

where ζ represents the correlation length, and is proportional to the Flory-Huggins interaction parameter. In the low-Q region, it can be used to estimate R_g

$$\zeta = \frac{R_g}{\sqrt{3}}$$

In chloroform R_g for PVF was estimated to be 5.9 nm, and increased by about 30% to around 7.5 nm when pyrrole monomers were present in solution.

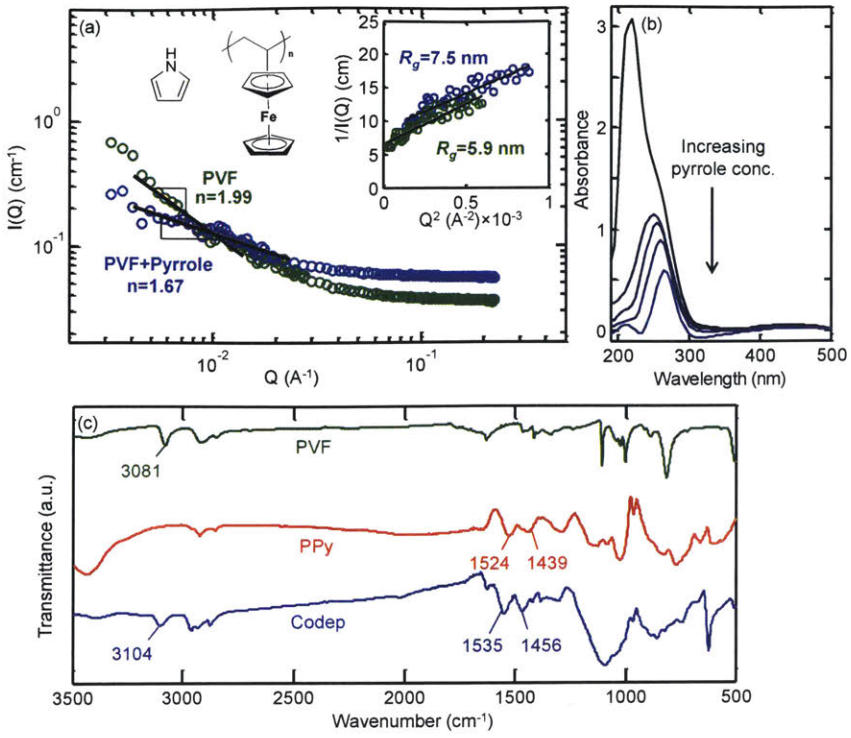

Figure 2-9. (a) SANS profiles of PVF with (blue) and without (green) pyrrole indicate the conformation change of PVF chains in solution. Inset: Partial Zimm plots of PVF and PVF in the presence of pyrrole. (b) UV-vis absorbance of 0.3 mM ferrocene in ethanol decreased significantly as the concentration of pyrrole increased from 0 to 100 mM. (c) FTIR of PVF, PPy and the formed hybrid indicated the red-shift of peaks for C=C stretching and C-N stretching in the pyrrole ring and the C-H stretching in the ferrocene moieties.

2.2.6.2 UV-Vis spectroscopy

To substantiate the likelihood of the π-π stacking interactions between PVF and PPy, we used UV-vis spectroscopy to probe the molecular interactions between pyrrole monomer and PVF, both of which possess π-aromatic cyclic moieties, in solution. The ferrocene units in each repeating unit of PVF contain two cyclopentadiene rings and have a characteristic energy absorption band around 220 nm, corresponding to the $\pi \rightarrow \pi^*$ transition.[62] Each pyrrole molecule

contains a 5-membered heterocyclic aromatic ring, exhibiting a characteristic peak around 210 nm.[63] For simplicity, the UV-vis spectrum of ferrocene was studied, rather than that of PVF, along with the spectrum of pyrrole. The ferrocene absorption peak decreased significantly as the pyrrole concentration increased from 0 mM to 100 mM (**Figure 2-9b**). The decreased UV absorption intensity, or hypochromism, of ferrocene in the presence of pyrrole is commonly observed in molecules with π-π stacking interactions, which is a result of the intermolecular overlapping of p-orbitals in their π-conjugated systems.[64] This significant suppression of the ferrocene absorption peak indicates intimate molecular interactions between pyrrole and ferrocene in solution, which could be a result of a greatly extended molecular packing between the cyclopentadiene rings in PVF and the heterocyclic aromatic ring in pyrrole.[64]

2.2.6.3 Fourier transform infrared spectroscopy (FTIR)

SANS and UV-vis spectroscopy elucidated the molecular interaction between pyrrole and PVF in solution before the electrochemical co-deposition. We used FTIR to study this interaction within the formed hybrid after the co-deposition process. Pure PVF shows characteristic peaks at 3081, 1105, 1023, 999, and 810 cm^{-1} (**Figure 2-9c**).[62] For electrochemically polymerized PPy, FTIR shows characteristic peaks at 1524, 1439, 1080, and 1012 cm^{-1}.[65] In comparison, the co-deposited polymer hybrid exhibited a broad peak from 1000 to 1300 cm^{-1}, as a result of the overlap of the peaks from the PVF and the significantly higher content of PPy in the hybrid. However, the peak corresponding to the C-H stretching of the ferrocene units[66] shifted from 3081 to 3104 cm^{-1} in the hybrid compared to the pure PVF. Similarly, the two observed peaks at 1524 cm^{-1} (C=C stretching) and 1439 cm^{-1} (C-N stretching) in PPy shifted to 1535 cm^{-1} and 1456 cm^{-1} in the hybrid, respectively. This red-shift of peaks for the C=C stretching and C-N stretching in the pyrrole ring

and the C-H stretching in ferrocene indicated that the interactions between π-electrons of the cyclopentadiene rings and the pyrrole still exist within the formed hybrid.[66]

2.2.6.4 Hybrid film structure formation

The electropolymerization of pyrrole starts with the oxidation of pyrrole monomers at the electrode surface to form cation radicals, followed by dimerization. Further oxidation of the dimers induces polymer chain growth, which occurs simultaneously with the formation of oligomers in solution.[39f] The nucleation of PPy on the electrode surfaces occurs when the length of the oligomeric chains surpasses the solubility limit. Here, the ferrocene groups of PVF, which are known to be associated closely with the pyrrole monomer in solution, may work as electron transfer mediators[67] to facilitate the formation of the pyrrole cation radicals and pyrrole oligomers in the vicinity of these PVF chains. We hypothesize that a mesoscopic phase separation occurs between the chloroform-rich phase and the pyrrole/oligopyrrole-rich phase as pyrrole monomers polymerize, with PVF partitioning preferentially into the pyrrole/oligopyrrole-rich phase, to contribute to the formation of the highly porous morphology. Although the exact mechanism of the porous film formation still remains unclear, preliminary results with other conducting polymer monomers that can have π-π stacking interactions with PVF indicate that this synthesis strategy can be generalized. We have electrochemically co-deposited PVF/polyindole hybrid and PVF/polyaniline hybrid. The surface morphologies of these hybrid films (Figure 2-13b, d) are significantly more porous than those of the electrochemically polymerized pure polyindole and pure polyaniline films (Figure 2-13a, c). Further examination of these analogous systems is the subject of on-going research.

2.3. Conclusion

We report a facile approach to synthesize a highly porous electroactive polymer hybrid with enhanced electrochemical energy storage performance. The synthesis strategy involved simultaneous electro-polymerization of pyrrole and electro-precipitation of PVF. The π-π stacking interactions between the heterocyclic pyrrole and the cyclopentadiene rings in ferrocene units cause the PVF coil to swell in solution. These pyrrole monomers are believed to remain associated with the PVF coils upon their electropolymerization. As a result, the two polymers are co-deposited on the substrate during the polymerization of PPy, such that the PPy chains interpenetrate the PVF domains and the two components are intimately associated with each other within the film thus formed. The polymer hybrid constructed in this way exhibited a highly porous morphology that is likely due to a phase separation between the pyrrole/oligopyrrole-rich and chloroform-rich phase during the polymerization process. This hybrid demonstrated excellent electrochemical properties, directly arising from the synergistic effects between PPy and PVF. A specific capacitance of 514.1 F g^{-1} was achieved for the PVF/PPy hybrid, which was significantly higher than those of PPy (27.3 F g^{-1}) and PVF (79.0 F g^{-1}). This facile electrochemical co-deposition approach can potentially be used to fabricate flexible supercapacitor devices. This interesting combination of properties from conducting polymers and non-conducting redox polymers with metallocene moieties opens up new opportunities for the design and fabrication of porous polymer hybrids with synergy for a variety of applications, such as energy storage, sensing, and catalysis.

2.4. Experimental Section

2.4.1. Electrode Fabrication

Polymer modified electrodes were prepared by applying a constant current density of 2 mA cm^{-2} to the carbon paper electrode in a three-electrode cell, where the counter electrode was a Pt wire and the reference electrode was Ag/AgCl. The PVF/PPy hybrids were fabricated by electrochemical co-deposition in 5 mL chloroform ($CHCl_3$) solution containing 0.104 M pyrrole, 1 mg mL^{-1} PVF, and 0.1 M tetrabutylammonia perchlorate (TBA-ClO_4). All depositions were performed for 5 min.

2.4.2. Electrochemical Characterization

All electrochemical polymerization and electrochemical characterizations were performed using an AutoLab PGSTAT 30 potentiostat and GPES software, version 4.9 (Eco Chemie). Cyclic voltammetry and galvanostatic discharge measurements were conducted in 0.5 M sodium perchlorate solution in both the three-electrode system and the two-electrode system. In the three-electrode cell, Pt wire and Ag/AgCl were used as the counter electrode and the reference electrode, respectively. The two-electrode cell was fabricated by sandwiching a filter paper between two polymer-deposited carbon paper electrodes. The electrode-filter paper-electrode set-up was then inserted between two glass slides for support. The electrochemical impedance spectroscopy (EIS) measurements on the two-electrode supercapacitor cells were performed in the frequency range of 100 kHz to 0.01 Hz with an electrochemical impedance analyzer (Gamery EIS300TM).

2.4.3. Polymer Characterization

Nitrogen adsorption/desorption was conducted on an automatic volumetric adsorption analyzer (Micromeritics ASAP2020). The PVF/PPy polymer hybrid films were first deposited on

stainless steel sheets and then peeled off for the N_2 physisorption measurements. XPS was performed with a PHI Versa Probe II. The X-ray used was set at 200 μm, 50W and 15kV. An XPS full scan survey was performed with a pass energy of 187.85 eV in the 0-1100 eV binding energy region. Angle-resolved XPS was performed with an argon single-ion gun for depth profiling. Changes in elemental composition within the polymer films up to 10 nm in depth were recorded nondestructively at various sample tilt angles relative to the analyzer, with values of 20°, 45 °, and 90 °. To allow depth profiling, the angle-resolved XPS was performed on polymer hybrid films that were deposited on a flat stainless steel sheet in the absence of carbon fibers. XPS survey scans were analyzed using the CasaXPS software. The spectra were calibrated with the C_{1s} peak (284.8 eV). The quantification regions are subtracted using a Shirley background.

Small-angle neutron scattering (SANS) was performed on the D22 diffractometer at Institut Laue-Langevin, Grenoble, France. The neutron wavelength used was λ = 10 Å at two different detector distances and a Q value between 0.0024 and 0.37 $Å^{-1}$ was realized. The absolute cross section I (Q) (cm^{-1}) as a function of momentum transfer Q ($Å^{-1}$) was obtained via data normalization. The measurements were performed in Hellma fused silica cuvettes with a path length of 2 mm. To provide the necessary contrast, the dilute polymer aqueous systems were measured at 5 mg mL^{-1} in *d*-chloroform (scattering length density $\rho = 3.11 \times 10^{10}$ cm^{-2}). Data analyzed were in absolute units based on the sample compositions. A flat background term was employed to account for any low level of residual incoherent scattering during the fitting process. UV-vis absorption experiments were performed with Evolution™ 201/220 UV-Visible Spectrophotometers (Thermo Scientific). Fourier transform infrared spectroscopy (FT-IR) was measured on Nicolet NEXUS. Thermogravimetric analysis of the prepared electrodes was

conducted using Q50 TGA (TA Instruments). Samples were equilibrated at room temperature, followed by ramping from room temperature to 900 °C at a heating rate of 5 °C min^{-1}.

2.5. Supporting Information

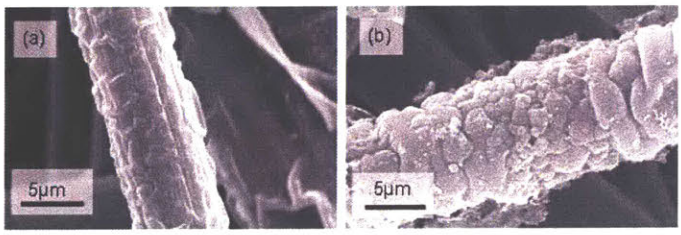

Figure 2-10. SEM images of core-shell structured polymer films that were deposited on carbon fibers: (a) CF-PVF/PPy and (b) CF-PPy/PVF.

2.5.1. Fabrication of Carbon Paper Electrode

The carbon fiber electrode was fabricated by using a piece of carbon fiber paper (1 cm × 2 cm) as the substrate which was connected to a copper wire with copper tape (**Figure 2-11a**).

2.5.2. Fabrication of Two-Electrode Symmetric Supercapacitors

In the two-electrode symmetric supercapacitor device, a piece of filter paper was used as the separator to prevent the two electrodes from contacting each other while allowing ions to diffuse through. The filter paper was sandwiched between two electrodes (polymer coated carbon fiber paper). The electrode-filter paper-electrode setup was then sandwiched between two glass slides, which were pressed against each other by tape without sealing (**Figure 2-11b**). The

electrochemical performance of the electrode was evaluated by immersing the device in 0.5 M $NaClO_4$, where the electrolyte solution had a depth of 1 cm to prevent the contact between the copper tape and the electrolyte solution.

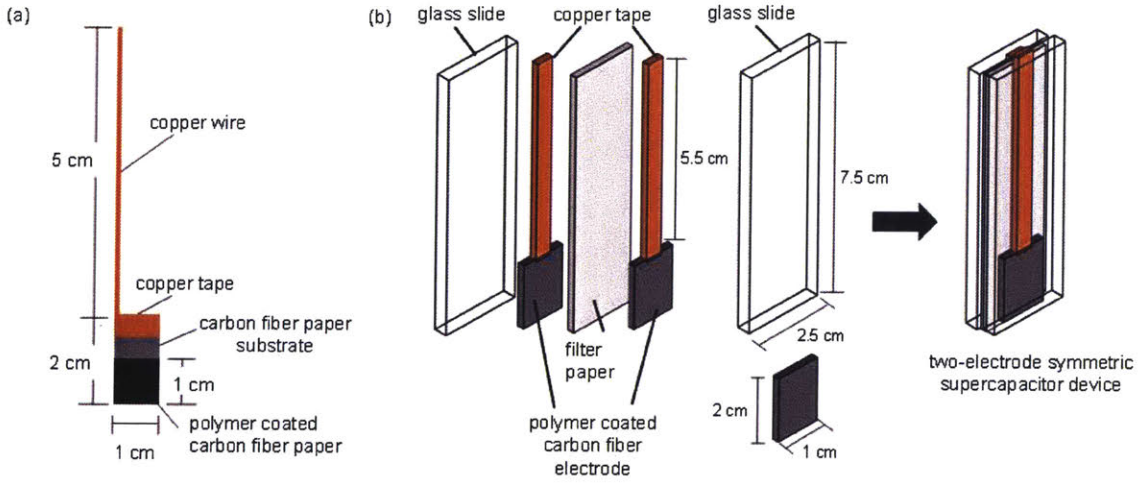

Figure 2-11. (a) Schematic of the polymer modified carbon paper electrode. (b) Schematic of the two-electrode symmetric supercapacitor device.

2.5.3. Characterization of co-deposited polymer hybrids after hydrothermal process (CF-CodepH)

The co-deposited PVF/PPy hybrid was treated with a hydrothermal process[57] to improve its cycling stability. Here, we refer to the electrode that is modified by the co-deposited polymer hybrid with the hydrothermal treatment as CF-CodepH. As observed by SEM, the porous film structure of the CF-Codep was preserved after the hydrothermal process (Figure 2-12a,b). In addition, the polymer hybrid maintained its porous film morphology after 3000 cycles (Figure 2-12c), which confirmed that the formed carbonaceous shell can provide structural support and

prevent the polymer film from exfoliating from the carbon fiber surface during the charge/discharge process. The nitrogen adsorption/desorption measurement of the treated hybrid polymer films gave a similar isotherm and pore size distribution as that of the polymer hybrid before the hydrothermal treatment (Figure 2-12d,e). The calculated BET surface area is 160.9 m^2 g^{-1}, which is also comparable to that of the hybrid polymer films without the treatment (166.8 m^2 g^{-1}). To study the surface chemistry of the PVF/PPy hybrid after the hydrothermal process, XPS was performed on CF-Codep and CF-CodepH (Figure 2-12g). After the hydrothermal treatment, the N_{1s} and Fe_{2p} peaks disappeared due to the coating of the carbon shell on the PVF/PPy polymer hybrid. The increased O_{1s} signal is likely due to the remaining glucose on the electrode surface from the solution used during the hydrothermal treatment.

In addition, the Nyquist plots for CF-Codep, CF-CodepH, and CF-CodepH after 3000 cycles are shown in Figure 2-12f. We found that, after the hydrothermal treatment, the co-deposited hybrid had a slightly decreased solution resistance, possibly because the wrapping of the polymer hybrid with a conductive carbon shell led to a better electron transport property while the porous structure was still retained, as confirmed by the SEM and BET analyses (Figure 2-12b,d). Additionally, we observed minimum changes in R_s and R_{ct} after 3000 charge/discharge cycles for CF-CodepH; SEM also suggested very minor structural changes after the cycling stability test. To further confirm that the electrochemical performance of the electrode is not compromised after the hydrothermal process, CF-CodepH was evaluated via cyclic voltammetry in a three-electrode system at various scan rates from 0 to 0.2 V s^{-1} (Figure 2-12h). The deposition of a thin carbon shell resulted in a distorted CV profile compared to that of CF-Codep (Figure 2-8a). The calculated specific capacitance was 572 F g^{-1} at 0.01 V s^{-1}, which was slightly higher than that of CF-Codep (514.1 F g^{-1}) due to the double layer effect of the carbon shells. At higher scan rates, the specific

capacitance decreased, but still retained a relatively high value of 212 F g^{-1} at 0.2 V s^{-1}. To give a more accurate evaluation of the CF-CodepH electrode, the CVs and galvanostatic measurements were also conducted in a two-electrode system (Figure 2-12i, j). The CF-CodepH electrode exhibited a specific capacitance of 353 F g^{-1} at a current density of 0.625 A g^{-1}, which is comparable to that of CF-Codep (345.3 F g^{-1}at 0.7 A g^{-1}).

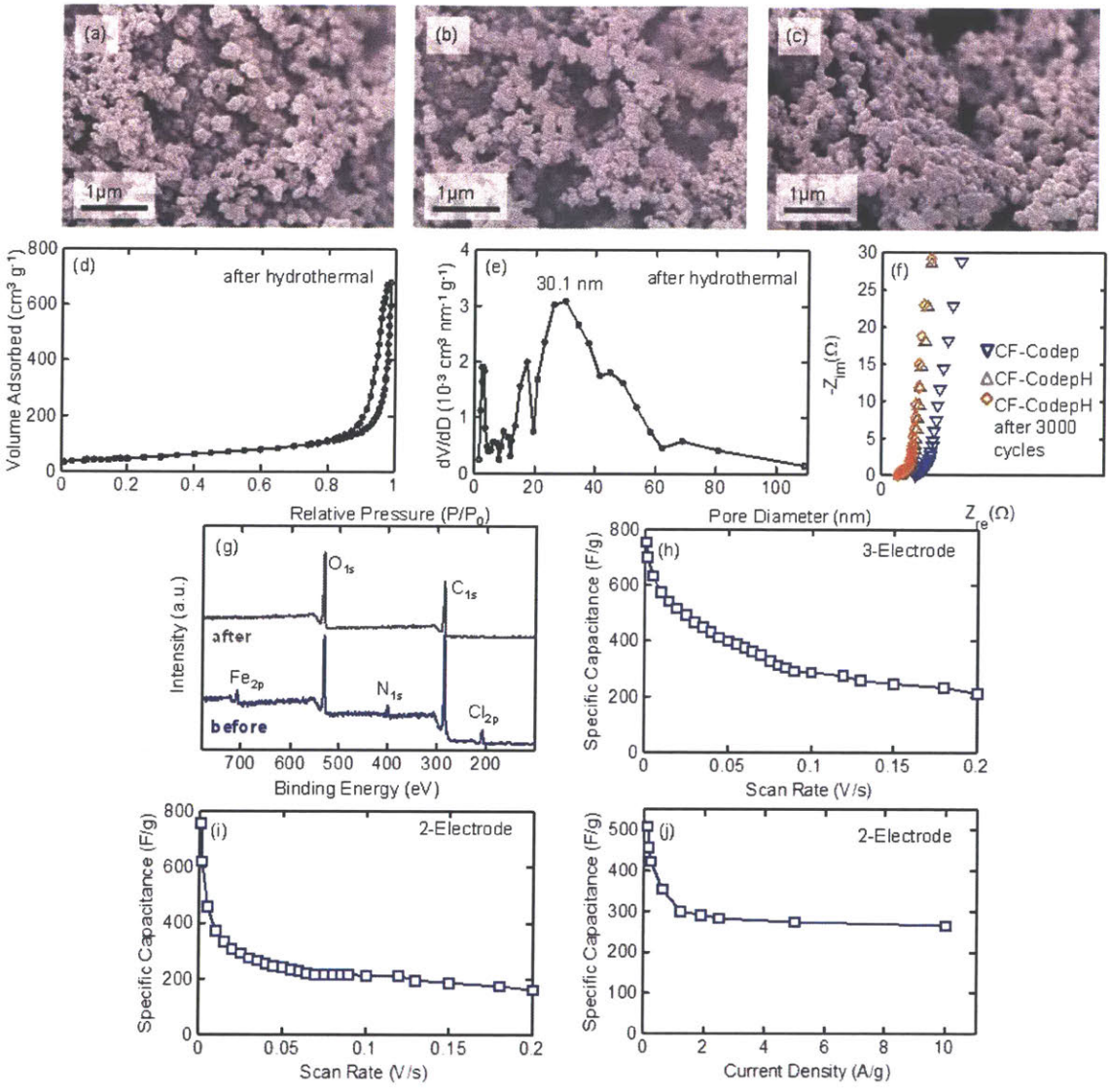

Figure 2-12. SEM images of co-deposited polymer films (a) before the hydrothermal process, (b) after the hydrothermal process, and (c) after 3000 cycles indicate that the surface morphology of the polymer hybrid is preserved after the hydrothermal treatment and after the cycling stability measurement. (d) N_2 physisorption isotherms and (e) the pore size distribution of the co-deposited polymer after hydrothermal process show characteristics similar to that of the polymers without the hydrothermal treatment. (g) XPS survey scan of CF-Codep in comparison to that of CF-CodepH. (f) EIS measurment for the CF-Codep, CF-CodepH, and CF-Codep after 3000 cycles. The specific capacitance measured at various scan rates from 0-0.2 V s^{-1} in (h) a three-electrode system and (i) a two-electrode system, and (j) at various current densities in a two-electrode systems.

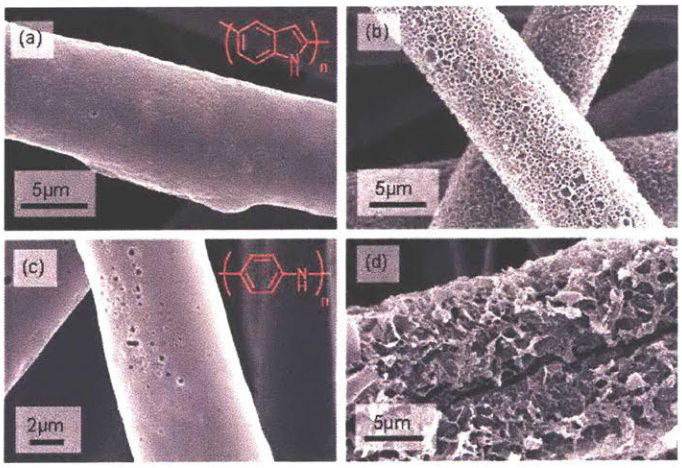

Figure 2-13. SEM images of electrochemically (a) polymerized polyindole, (b) co-deposited PVF and polyindole hybrid, (c) polymerized polyaniline, and (d) co-deposited PVF and polyaniline hybrid on carbon fibers.

Table 2-1. Specific capacitance and cycling performance of various supercapacitor electrode materials reported in recent years in comparison with the PVF/PPy hybrid in this work.

Composite	Specific capacitance/F g^{-1}	Electrolyte	Voltage window/V (Ag/AgCl)	Current load/scan rate	Retention ratio	Year
PVF/PPy hybrid	514.1 (3-Electrode)	0.5 M $NaClO_4$	0 to 0.7	10 mV s^{-1}	94.5% after 3000 cycles	2015
	345.3 (2-Electrode)	0.5 M $NaClO_4$	0 to 0.7	0.7 A g^{-1}		
Ag-doped PEDOT:PSS/CNT[68]	85.3 (2-Electrode)	0.1 g mL^{-1} poly(vinyl alcohol)/water	0 to 0.8	0.15 mA cm^{-2}	NA	2018
lignosulfonate /CNF-PEDOT[69]	230 (3-Electrode)	[0.1 M $HClO_4$ in water]/acetonitrile (9/1)	0 to 0.7	0.5 A g^{-1}	45% after 700 cycles	2018
MnO_2NFs@PPy NWs core/shell[70]	276 (3-Electrode)	1 M Na_2SO_4	0 to 0.9	2 A g^{-1}	93.4% after 1500 cycles	2017
poly tris[4-(2-thienyl)phenyl]amine[71]	278 (3-Electrode)	1 M $TEAFB_4$ in acetonitrile	0 to 1.5	2.5 mA cm^{-2}	NA	2017
ZnO@MnO_2 core-shell pillar arrays on Ni foam[72]	423.5 (3-Electrode)	1 M Na_2SO_4	-0.2 to 0.8	0.5 A g^{-1}	92% after 3000 cycles	2015
$MgCo_2O_4$[73]	321 (3-Electrode)	3 M LiOH	0 to 0.5	0.5 A g^{-1}	~100% after 2000 cycles	2015

MnO_2 Nanoflakes/hierarchical porous carbon[51a]	417.2 (3-Electrode)	1 M Na_2SO_4	-0.1 to 0.9	20 mV s^{-1}	100% after 10000 cycles	2015
Zinc oxide/activated carbon nanofiber[51c]	178.2 (2-Electrode)	6 M KOH	0 to 1.0	1-20 mA/cm^2	75% after 1000 cycles	2015
Co_3O_4/carbon[51b]	456 (3-Electrode)	2 M KOH	-0.1 to 0.55	2 mV s^{-1}	93.4% after 2000 cycles	2015
Corncob residue derived carbon[49]	314 (3-Electrode)	6 M KOH	-1.0 to 0[a)]	5 mV s^{-1}	~100% after 10000 cycles	2015
Nitrogen-containing carbon microspheres[50]	228 (3-Electrode)	6 M KOH	-1 to 0[a)]	1 A g^{-1}	86% after 5000 cycles	2015
Porous and nitrogen-rich carbons [74]	492 (3-Electrode)	1 M H_2SO_4	-0.9 to -0.1[a)]	0.1 A g^{-1}	97-98% after 1000 cycles	2015
Silicon carbide microsphere/ birnessite-type MnO_x[75]	251.3 (3-Electrode)	1 M Na_2SO_4	-0.1 to 0.9	10 mV s^{-1}	94.43% after 1000 cycles	2014
α-MnO_2 nanowires [76]	118 (3-Electrode)	0.5 M Na_2SO_4	-0.2 to 0.8	2 mV s^{-1}	95.3% after 1000 cycles	2014
Cobalt oxides nanoparticles[77]	362.8 (3-Electrode)	6 M KOH	0 to 0.35	0.2 A g^{-1}	73.5% after 1000 cycles	2014
MnO_2 microspheres with Fe_3O_4 nanoparticles[78]	448 (3-Electrode)	1 M Na_2SO_4	0 to 1.0	5 mV s^{-1}	76% after 5000 cycles	2014
ZnO nanorod@NiO/MoO_2[79]	983 (3-Electrode)	2 M KOH	0 to 0.5	4.16 A g^{-1}	91.7% after 4000 cycles	2014
SnO_2/ rGO droplet aerogel[80]	310 (2-Electrode)	2 M KOH	0 to 1.0	5 mV s^{-1}	90% after 1000 cycles	2014
V_2O_5-rGO[81]	178.5 (3-Electrode)	1 M $LiChO_4$/PC	-0.8 to 0.8	0.05 A g^{-1}	~100% after 8000 cycles	2014
$CuSbSe_xS_{2-x}$ mesocrystals[82]	48 (3-Electrode)	3 M LiOH	0.1-0.55	0.4 A g^{-1}	100% after 1000 charges	2014

[a)] Reference electrode: Hg/HgO

Acknowledgements

This research was supported by a grant from the MIT Energy Initiative Seed Fund program. X.M. was supported by a Skoltech Fellowship.

Chapter 3. Multiphase Diffusion-Controlled Electrochemical Synthesis of One Dimensional Conducting Polymer Nanostructures

Doping/de-doping processes underlie the properties of tunable conductivity and high charge storage capacity in conducting polymers. However, they are often hampered by inefficient counter-ion diffusion, due to low surface areas and undesirable morphologies. Nanostructuring of π-conjugated systems is an elegant strategy to improve the utility of conducting polymers in applications such as energy storage, catalysis and separations. Here, we present a conceptually new synthesis strategy for constructing conducting polymer nanostructures, based on multiphase diffusion-controlled electrochemical polymerization. A CO_2–bound polyamine was used to induce phase separation at the electrode surface. Interactions between pyrroles and carbamate groups hinder the diffusivity of pyrrole significantly, thereby forcing the polymerization process into a transport-limited regime that leads to growth of 1D polymer nanostructures. This method results in a porous coating consisting of polypyrrole fibers with a significantly higher specific surface area (three-fold) and enhanced energy storage capabilities (four-fold) compared to nonporous polypyrrole. This porous coating also demonstrated promise as an adsorption medium for toxic gas molecules that are urgent targets for environmental remediation. This approach offers insight into the rational design and fabrication of conducting polymer nanostructures, which may be applicable to a wealth of material systems. The nanostructured conducting polymer systems can be flexibly integrated onto porous conductive substrates, and may serve as key components for technology platforms with applications ranging from energy storage to environmental remediation.

3.1. Introduction

The doping level of conducting polymers, in which the π-conjugated backbones can delocalize charge carriers, can be modulated to tune the conductivity of these materials. The simultaneous insertion of counter-ions into the polymer during doping is essential to maintain charge neutrality and, consequently, has a profound impact on the doping process. Meanwhile, nanostructures that are intermediate to the molecular and macroscopic levels can give rise to attractive properties, such as large polymeric interfacial areas and high porosities, while maintaining excellent ion access during doping/de-doping processes. As a result, the union of nanostructured morphology and π-conjugated systems has proven to be a powerful strategy to enhance the merit of conducting polymers as candidate materials in applications that include energy storage,[83] catalysis[84] and separations.[85]

To date, template and template-free methods have been developed to synthesize conducting polymer nanostructures. In template methods, hard templates, such as anodized alumina,[14, 86] opals[15] and polycarbonate[14b, 16], serve as sacrificial materials to control the shape, size and orientation of nanostructures.[87] Although the template fabrication is simple, the post-synthesis template removal process can be cost-prohibitive or detrimental to the environment,[87a] and the harsh treatment conditions can damage the nanostructures and introduce defects and impurities.[88] Soft template methods employ the non-covalent interactions of surfactants, such as π–π stacking, van der Waals forces, hydrogen bonding, and electrostatic interactions, to guide the self-assembly of monomers that, upon polymerization, preserve the nanostructures.[13, 19, 89] In soft template methods, it is challenging to exert precise control over the desired shape and size of the nanostructures, however. Template-free methods, such as those obtained via gas bubbling[90] and alternating current-bipolar electrolysis,[91] are easy to implement and cost-efficient. The structures

thus generated are often at micrometer scales, and therefore provide limited performance improvement, compared to their nanostructured counterparts, in applications impacted by polymer interfacial areas. Mechanical stretching and the electrospinning method, though versatile, are limited to polymers with specific physical properties, such as their viscoelasticity.

Polypyrrole (PPy) has a π-conjugated backbone comprising five-membered aromatic rings whose conductivity is governed by the doping level of the polymer. PPy can be easily synthesized via electrochemical polymerization upon application of a positive potential to a conductive substrate that is immersed in an electrolyte solution containing pyrrole. As the polypyrrole chain grows, it quickly exceeds its solubility and precipitates onto the conductive substrate. PPy that is synthesized by this conventional method exhibits a compact and cauliflower-like film morphology. This non-porous structure provides limited interfacial area for interaction with target entities and inhibits fast ion transport within the polymer bulk, resulting in low utilization of polypyrrole. Despite the advantages of ease of synthesis, superior thermal stability and low cost, PPy was reported to have poor mechanical and physical properties.[92] It is also not soluble in most solvents and does not melt upon heating.[93] These properties preclude possible nanostructuring methods by mechanical stretching, electrospinning and solution processing, making it crucial to nanostructure PPy during the synthesis process itself.

Phase separation has been exploited as a technique to generate micropores in membrane fabrications for filtration purposes. [94] Instabilities at growth interfaces have been used to control the morphology of metallic materials to form 1D, spherical and dendritic structures.[95] The coupling effect of mass transport and interfacial kinetics in crystallization were found to impact the interfacial growth instabilities,[96] and therefore exert control over the morphology of

electrodeposited metal particles .[95b] To date, only a few studies have applied these techniques in synthesizing conducting polymer nanostructures.[97]

In this work, we report a strategy for generating nanostructures of conducting polymers that is fundamentally different from previous methods. In this strategy, a CO_2–bound polyamine was used to induce phase separation and to limit diffusion of monomer during polymerization, giving rise to a growth instability and the formation of a porous coating composed of polypyrrole nanofibers. Here, we take advantage of the interactions between aromatic monomers and carbamate groups to induce transport limitations on pyrrole monomer during electro-polymerization. The resulting reduction in monomer diffusivity subjects the polymer growth process to a diffusion-controlled condition, which consequently facilitates the 1D growth of polypyrrole nanofibers. The polyamine used, polyethylenimine (PEI), is inexpensive and readily available.[98] The water-soluble nature of PEI allows the synthesis to be carried out in an aqueous environment without the use of hazardous reagents or need for complex purification processes. As PEI is also safe and biocompatible, this approach is superior to methods involving metal oxides[87a] or metallocenes[83] for biological applications. This electrochemical method allows the coating to be deposited on various conductive substrates, including porous substrates. We have further demonstrated that the resulting porous morphology endows the PPy coating with excellent electrochemical properties and improves adsorption performance for aldehydes, which are contaminants of environmental interest. This strategy of combining phase separation and subsequent diffusion-controlled reaction opens up new opportunities for the engineering of conducting polymer nanostructures: by taking advantage of a diffusion-limited instability at the growth front, we achieve a level of morphological design and fabrication in a material system that may have applications well beyond conducting polymers.

3.2. Results and Discussion

3.2.1. Surface Morphology

Electro-polymerized polypyrrole was deposited onto a conductive carbon paper (CP) substrate composed of non-woven carbon microfibers with a diameter of 8 μm (**Figure 1d**), using a process illustrated in **Figure 3-1a**. Under an applied potential of 0.8 V, the polypyrrole chains precipitate onto the carbon microfibers as they grow. In the presence of CO_2-bound PEI in a 0.1 M solution of pyrrole, a conformal coating of porous polyyrrole (pPPy) was formed on each carbon microfiber (**Figure 3-1b**). High resolution SEM revealed that the pPPy sheath consisted of fibrous structures with diameters of ~100 nm (**Figure 3-1c**). This morphology is drastically different from the thick and non-porous dense film obtained when polypyrrole was polymerized form a 0.1 M solution of pyrrole in the conventional manner (**Figure 3-1e**). The Brunauer-Emmett-Teller (BET) surface area of pPPy was determined to be 173.5±3.6 $m^2 g^{-1}$ (see Supporting Information, Section 1, for details), significantly higher than that of the conventionally polymerized polypyrrole (37 - 61 $m^2 g^{-1}$).[45] The synthesis of PPy in the presence of PEI without CO_2 also resulted in a non-porous PPy morphology (**Figure 3-1f**), demonstrating the essential role that CO_2 plays in this nanostructuring strategy. The carbon paper substrate, along with the pPPy coating, results in a hierarchical structure of macro- and mesopores.

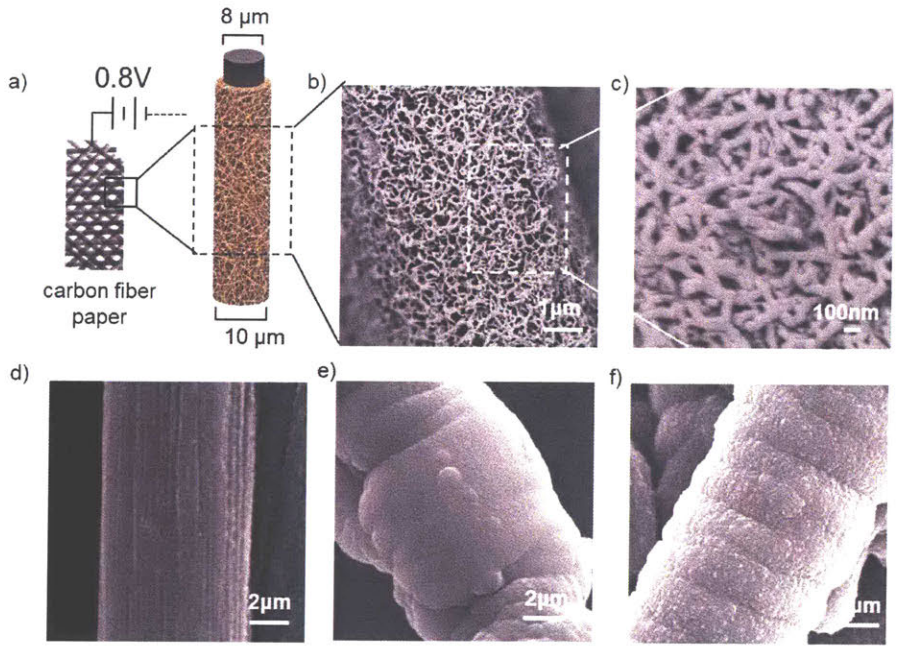

Figure 3-1. (a) Schematic shows how electro-polymerized pPPy is deposited on carbon microfiber substrate. (b) SEM shows that pPPy is a porous coating. (c) High resolution SEM indicates pPPy coating consists of nanofibers with diameters of 100 nm. (d) SEM image shows that pristine fiber in carbon paper has a diameter of 8 µm. (e) SEM image shows that polypyrrole synthesized by direct electro-polymerization has a non-porous morphology. (f) SEM image shows that polypyrrole synthesized in the presence of PEI without CO_2 exhibits non-porous morphology.

3.2.2. Electrochemical Characterization

Cyclic voltammetry (CV) is an effective tool for probing the redox properties of polymers. CV profiles for pPPy and PPy deposited on carbon fiber substrates both had quasi-rectangular shapes, characteristic of electro-polymerized polypyrrole (**Figure 3-2a**). pPPy exhibited a nearly four-fold increase in current response compared to that of PPy, which we attribute to the increase in its polymer/electrolyte interfacial area. For comparison, CV of a blank carbon paper substrate

gave negligible current response, suggesting that charging of the electrochemical double layer on the carbon substrate had a minimal contribution to the charge storage capacity of the composite. pPPy exhibited a specific capacitance of 370.4 F g^{-1}, compared to 71.4 F g^{-1} for PPy (**Figure 3-2b**). In a thick PPy film, the electrolyte has limited access to polypyrrole chains over the time frame of the electrochemical measurement. By contrast, the gaps between fibers in pPPy provide abundant pathways and facilitate the easy penetration of counter-ions into the film, facilitating the redox reactions within the polypyrrole. The capacitance of PPy quickly dropped to 50% of the maximum capacitance as the scan rate increased from 0.01 V s^{-1} to 0.02 V s^{-1}, and eventually fell to less than 20% of its maximum capacitance (**Figure 3-2c**). pPPy, however, experienced a much slower decay in capacitance, and more than 40% of its maximum capacitance was retained at a high scan rate of 0.1 V s^{-1}. This improved rate performance with pPPy is attributed to the reduced ion diffusion limitation within its porous polymer film, as confirmed by electrochemical impedance spectroscopy (see below).

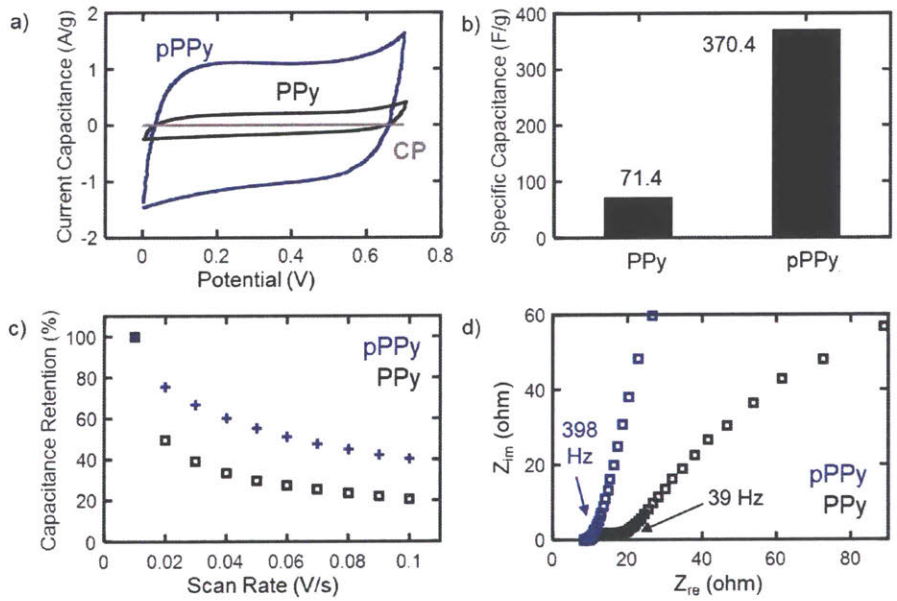

Figure 3-2. (a) pPPy has enhanced CV responses compared to that of PPy. The CV of CP exhibits negligible current responses. (b) The specific capacitances of pPPy and PPy are calculated from the CV scans. See Supporting Information, Section 3 for details. (c) pPPy has higher capacitance retentions than PPy at scan rates of 0.01 to 0.1 V s^{-1}. (d) Nyquist plot for EIS measurements confirms the fast ion transport within pPPy.

The electrochemical properties of pPPy were further probed by electrochemical impedance spectroscopy (EIS). The intercept of the EIS spectrum with the Z_{re} axis gives the solution resistance associated with the pPPy electrode, R_s. pPPy exhibits a smaller R_s as measured by EIS, than does PPy (**Figure 3-2d**). The knee frequency, where the Nyguist plot transitions from the high-frequency to the low-frequency component, corresponds to the maximum frequency at which the electrode can maintain capacitive behavior. The knee frequency for pPPy (398 Hz) was observed to be an order of magnitude higher than that of the PPy (39 Hz), confirming the improvement in electrolyte access to, and the shortened diffusion distance within, the porous polymer film.[99]

3.2.3. Aldehyde Adsorption

As it has a porous morphology with a high specific surface area, pPPy is a promising candidate for adsorbing contaminants of environmental interest from both air and water resources. Aldehydes, a class of organic compounds characterized by the formyl moiety, can be found in building materials,[100] tobacco smoke,[101] and natural surface waters.[102] The incomplete combustion of biomass and fossil fuels,[103] along with the photochemical oxidation of hydrocarbons in the atmosphere,[104] also contributes to the presence of aldehydes in polluted air. The toxicity and carcinogenicity due to exposure to high doses of aldehydes have been well established.[105]

Conducting polymers containing protonated nitrogen atoms in their backbones can adsorb aldehydes and donate protons to the adsorbed molecules. This property has been used to develop chemiresistive sensors based on conducting polymers that detect aldehydes by measuring the induced change in conductance.[106] Here, pPPy and PPy deposited on carbon paper substrates (pPPy/CP and PPy/CP) were used to adsorb two model aldehydes, acetaldehyde and butyraldehyde, from an aqueous phase. It was found that the equilibrium solution concentration of aldehydes decreased the most when pPPy/CP was used as the adsorbent (**Figure 3-3a, b**). The adsorption capacity, calculated based on the measured UV-Vis spectrum, demonstrated that pPPy/CP enhanced the adsorption amount by nearly two-fold (**Figure 3-3c**). Here, the compact film morphology of PPy offers a limited number of sites for adsorption of aldehydes. In contrast, the nanostructures within the pPPy film provide a large polymer/solution interface for aldehydes to interact with the protonated nitrogen atoms of the polypyrrole backbone. The increase in adsorption amount by pPPy/CP (two-fold) was not proportional to its increase in the specific surface area (four-fold); this discrepancy is likely due to the inaccessibility of some small pores within the film. Nevertheless, pPPy demonstrated a significant improvement in the utilization of receptor sites compared to non-porous PPy.

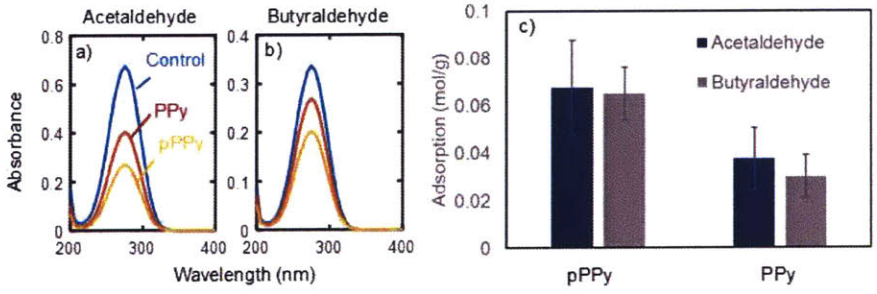

Figure 3-3. UV-Vis absorbance measurements of acetaldehyde (a) and butyraldehyde (b) in solutions that have been soaked with no sample, PPy or pPPy. The changes in peak intensity

indicate the decrease of aldehyde concentrations. The corresponding aldehyde adsorption capacities of pPPy/CP and PPy are plotted in (c).

3.2.4. Study of the Electrochemical Deposition Mechanism

In the conventional synthesis process, the deposition of electro-polymerized polypyrrole can be described as a nucleation and growth process. During nucleation, monomers first adsorb onto the electrode, followed by oligomerization; alternatively, oligomers can also form first in solution and then precipitate at the electrode surface.[107] In the absence of strong concentration gradients, the precipitates grow isotropically, spreading across the electrode surface to form a thin layer of polypyrole.[107b, 108] The polymer growth front then advances more or less uniformly, leading to a nonporous morphology consistent with that observed by SEM (**Figure 3-1e**).

In the new synthesis strategy described here, the deposition mechanism is fundamentally altered by the presence of PEI/CO_2. We hypothesize that the formation of polypyrrole 1D nanostructure is due to a phase separation between the pyrrole-rich and PEI/CO_2-rich phases at the electrode surface, followed by a diffusion-controlled polymerization process. A two-phase region was verified experimentally by constructing a ternary phase diagram of PEI/CO_2, water, and pyrrole (see Supporting Information, Section 4). The oligomerization of pyrrole can result in the upward shift of the phase boundary between the one- and two-phase regions, because oligo-pyrrole is less soluble in water than pyrrole monomer is. Consequently, phase separation occurs, resulting in domains of the pyrrole/oligopyrrole-rich phase at the electrode. Furthermore, the molecular interaction between pyrrole and PEI/CO_2 significantly hinders the diffusion of pyrrole within the PEI/CO_2-rich phase, giving rise to a strong pyrrole concentration gradient as electro-

polymerization proceeds. Under these conditions, the pyrrole-rich domains at the electrode surface form small protrusions that see higher concentrations of pyrrole monomer in the surrounding PEI/CO_2-rich phase compared to the electrode surface, due to the strong concentration gradient required to drive diffusion of pyrrole monomer to the reactive sites (**Figure 3-4**). These protrusions therefore grow anisotropically, resulting in formation of 1D polymer nanostructures. In what follows, we offer evidence in support of this hypothesis.

To investigate the hypothesized deposition mechanism, we first quantified the interaction between pyrrole and PEI/CO_2 experimentally. Secondly, a reaction-diffusion model was developed to confirm that the polymer growth process falls within a diffusion-controlled regime. Lastly, the effect of PEI/CO_2 concentration on surface morphology was studied to validate the proposed mechanism.

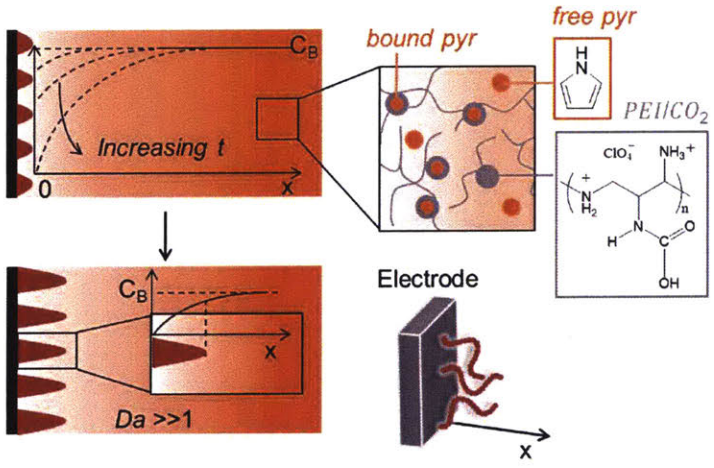

Figure 3-4. Schematic shows that the interaction between pyrrole and PEI/CO_2 leads to the reduction in the apparent diffusivity of pyrrole, which drives the polymerization process into a diffusion-controlled regime. Under this condition, protrusions at the polymer growth front experience a higher concentration than the base, due to the concentration gradient. The faster

polymerization at the tip of the protrusion results in extension of the protrusion, forming 1D polymer nanostructures.

1) Interaction of pyrrole with PEI/CO_2

The interaction between pyrrole and the carbamate groups in PEI/CO_2 was quantified by FTIR, to demonstrate the formation of carbamate groups in PEI/CO_2, and UV-Vis titration, to probe the interactions of the carbamates with pyrrole. In the FTIR spectra of PEI, the broad band at 3430 cm^{-1} and the narrow band at 800 cm^{-1} correspond to the N-H stretching and the N-H (oop) bending of the amine groups, respectively (**Figure 3-5a**).[109] The peak at 1100 cm^{-1} is due to the alkyl C-N stretching. Upon CO_2 sparging, some amine groups of PEI were converted to carbomate.[98] The suppression of N-H bending (1630 cm^{-1}) and the enhancement of COO^- asymmetric stretching (1570 cm^{-1}) confirms the formation of carbamate groups.[109]

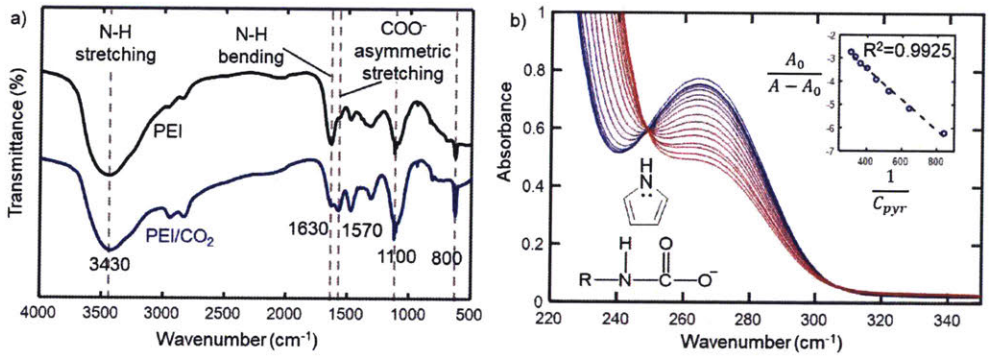

Figure 3-5. (a) FTIR of PEI and PEI/CO_2 confirms the binding of PEI with CO_2. (b) UV-Vis absorbance spectra of PEI/CO_2 exhibit hypochromism in the presence of pyrrole. Inset: linear fitting of UV-vis absorbance of PEI/CO_2 using the Benesi-Hildebrand equation.

UV-Vis titration is one of the most common approaches for quantifying non-covalent interactions.[110] It has been widely used in determining the complexation constant in supramolecular chemistry, such as those associated with the π-π stacking interactions between

ferrocene and macrocycles,[111] the binding of metal ions to ligands,[112] and the hydrophobic interactions involved in DNA intercalations.[113] As the resulting resonance structure of the carbamate group likely interacts with the aromatic ring of pyrrole in solution, and the carbamato anions exhibit a UV-Vis absorption peak,[114] we used the titration approach to quantify the interaction between pyrrole and carbamate groups, assuming that such interactions also quench the UV-Vis absorption peak. In the titration approach, the UV-Vis absorbance of PEI/CO_2 was monitored while the concentration of pyrrole in solution was increased slowly. Hypochromism was observed at 268 nm as a result of the pyrrole-PEI/CO_2 interactions (**Figure 3-5b**). The appearance of only one isosbestic point at 248 nm suggests that the formation of the complex between pyrrole and the carboxylate groups in PEI/CO_2 is random.[112a, 115] The decrease in absorbance of PEI/CO_2 was further analyzed quantitatively by fitting the absorbance intensity with the Benesi-Hildebrand equation, assuming a 1:1 binding ratio between a pyrrole monomer and a carbamate group:

$$\frac{A_0}{A-A_0} = \frac{\varepsilon_{pyr}}{\varepsilon_{pyr-PEI/CO_2}-\varepsilon_{pyr}} + \frac{\varepsilon_{pyr}}{\varepsilon_{pyr-PEI/CO_2}-\varepsilon_{pyr}}\left(\frac{1}{KC_{pyr}}\right), \quad (3.1)$$

where

$$K = \frac{C_{pyr-PEI/CO_2}}{C_{pyr}\,C_{PEI/CO_2}}. \quad (3.2)$$

The UV-Vis absorbance of PEI/CO_2 at 268 nm, with and without pyrrole, is denoted by A and A_0, respectively. ε_{pyr} and $\varepsilon_{PEI/CO2}$ are the molar absorptivities of pyrrole and PEI/CO_2 in water. C_{pyr} is the concentration of pyrrole in solution. The binding constant, K, between pyrrole and PEI/CO_2 can therefore be determined by the ratio of the intercept and the slope of the linear fitting of the left-hand side of the equation to $1/C_{pyr}$ (**Figure 3-5b inset**). Here, K was found to be 127.5

M^{-1} with a linear correlation coefficient of 0.9925; this result supports the assumed 1:1 binding ratio. The association constant for complexes involving aromatic π-stacking interactions have been found to be typically in the range 20 - 600 M^{-1}.[116] The change in Gibb's free energy associated with this interaction, $\Delta G = -RTlnK$, was calculated to be -11.8 kJ mol^{-1}. The negativity of ΔG indicates that association between pyrrole and PEI/CO_2 in the deposition solution is spontaneous. Association between pyrrole and PEI/CO_2 hinders the transport of pyrrole toward the electrode surface, since pyrrole must unbind in order to diffuse through the concentrated solution of PEI/CO_2.

2) Reaction-diffusion model

To investigate the deposition mechanism quantitatively, we interpreted the nanostructure growth process using a reaction-diffusion model. The electrode surface was assumed to be immersed in a semi-infinite medium, and the electro-polymerization modeled as a heterogeneous surface reaction. The concentration of pyrrole, C, at a distance, x, away from the electrode surface can be described by the following differential equation, with the indicated boundary conditions:

$$\frac{\partial C}{\partial t} = D\frac{\partial^2 C}{\partial x^2}; \quad C(x,0) = C_B,\ C(\infty,\mathrm{t}) = C_B,\ -D\frac{\partial C}{\partial x} = R_h(C) = kC_s. \qquad (3.3)$$

D is the diffusivity of pyrrole in the deposition solution. $R_h\ (C)$ is the rate of pyrrole consumption due to polymerization at the growth front, which is considered to be a first order heterogeneous reaction with a kinetic rate constant, k. C_B is the bulk concentration of pyrrole. C_s is the pyrrole concentration at the electrode surface. For a first order surface reaction, the differential equation can be solved analytically; the solution is: [117]

$$\theta = erf(\eta) + \exp(2\eta\tau + \tau^2)erfc(\eta + \tau), \qquad (3.4)$$

where $\square\square C/C_B$ is the dimensionless concentration, $\eta = x/2\sqrt{Dt}$ the dimensionless length, and $\tau = k\sqrt{t/D}$ the dimensionless time. The dimensionless concentration profile in **Figure 3-6a** shows that as τ increases, the surface concentration decreases gradually and eventually reaches a value near zero, corresponding to transition to the diffusion-controlled regime.

A quantitative study of the growth of the 1D nanostructure as a reaction-diffusion problem requires the determination of two key parameters: the diffusivity of pyrrole as a function of PEI/CO_2 concentration, and the kinetic rate constant for polymerization. The diffusion coefficient of pyrrole in water, D_w, was estimated with the Wilke-Chang correlation,[118] which gives satisfactory predictions for organic compounds in water:

$$D_w = 7.4\times10^{-8}\frac{(xM)^{0.5}T}{\mu V^{0.6}}, \quad (3.5)$$

where T is the absolute temperature, μ is the viscosity of the solvent, M is the molecular weight of pyrrole and V is its molar volume. The association parameter, x, is 2.6 for water. By this approach, we estimate D_w to be 1.35×10^{-9} m^2 s^{-1} for pyrrole in water. To account for the interactions between pyrrole and PEI/CO_2 in aqueous solutions, we estimated the apparent diffusivity of pyrrole, D_{app}, using a rule of mixtures and assuming that only the unbound (i.e. unassociated) pyrroles are free to diffuse in the PEI/CO_2 solution:

$$D_{app} = \frac{C_{pyr-PEI/CO_2} D_{bpyr} + C_{pyr} D_{ubpyr}}{C_{pyr-PEI/CO_2} + C_{pyr}}. \quad (3.6)$$

Here, D_{bpyr} is the diffusivity of pyrrole bound to carbamate, which is effectively zero. D_{ubpyr} is the diffusivity of free pyrrole in the solvent, which is effectively D_w. The concentrations, $C_{pyr-PEI/CO_2}$

and C_{pyr}, were calculated from the measured equilibrium constant, K. D_{app} was determined to be 2.32×10^{-12} m^2 s^{-1} by this approach. The kinetic rate constant, k, for the electro-polymerization of polypyrrole was determined experimentally by considering the process to be a first order heterogeneous reaction (see details in Supporting Information, Section 5). k was determined to be 5.0×10^{-6} m s^{-1}.

The time it takes for the system to transition to such a diffusion-controlled regime was determined by setting τ to a value ($\tau = 16$) large enough to give a negligible surface concentration ($\theta = 0.035$). It was found that $t = 24$ s when $D = D_{app}$, the diffusivity of pyrrole in PEI/CO_2 solution, which is significantly shorter than the duration of the experiment. On the contrary, $t = 1.4\times10^4$ s when using $D = D_w$, the case when PEI/CO_2 is not present. This analysis confirms that the system quickly transitions into a diffusion-controlled process during the polymer growth stage in the presence of PEI/CO_2 solution, while it never does so in the absence of PEI/CO_2. This conclusion is also supported by the values of the Damköhler number, Da, of the system (see details in Supporting Information, Section 6).

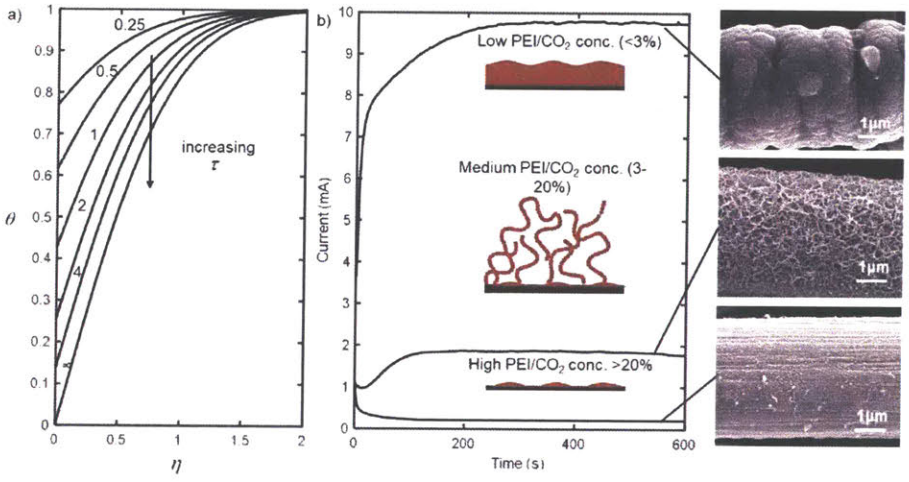

Figure 3-6. (a) Dimensionless concentration profile of pyrrole during polymer growth stage indicates the surface concentration decreases to a near-zero value as τ increases. (b) Current responses and SEM images of pPPy deposition at low, medium, and high PEI/CO_2 concentrations are consistent with the proposed mechanism.

4) Effect of PEI/CO_2 Concentration

It is proposed that the presence of PEI/CO_2 inhibits the diffusion of pyrrole to the electrode surface and facilitates the 1D growth of pPPy. To validate the hypothesized mechanism, the PEI/CO_2 concentration was varied and its effect on the deposition current and surface morphology was studied (**Figure 3-6b**).

The electrochemical polymerization of pyrrole starts by forming oxidized radicals and then coupling the radicals into oligopyrroles. The solubility of oligopyrrole decreases as the degree of polymerization increases, eventually resulting in oligomer that exceeds its solubility limit and deposits on the conductive substrate. At zero or low concentration of PEI/CO_2, the diffusivity of pyrrole is high, and allows rapid diffusion of pyrrole to the polymer surface. Under these reaction-controlled conditions, the polymer growth front advances rapidly, and eventually plateaus at a high value of deposition current, indicating that a stationary growth regime of polypyrrole with high deposition rate is reached.[89a] The observation of a uniform and nonporous surface morphology of polypyrrole fabricated under this condition supports this deposition mechanism qualitatively. When the concentration of PEI/CO_2 falls within a medium range (3-20 wt.%), the deposition current increases more slowly and plateaus at a lower value compared to that without PEI/CO_2, due to the lower diffusion rate of pyrrole in the presence of PEI/CO_2. The observed porous

morphology comprising 1-D nanostructures under these conditions is consistent with diffusion-limited growth. With a high concentration of PEI/CO_2 (above 20 wt.%), the deposition current decreases almost to zero. Under these conditions, the high concentration of PEI/CO_2 inhibits the diffusion of pyrrole towards the electrode surface to such an extent that it prevents polymer chain growth almost completely. This is in agreement with SEM observations, where the striation patterns of pristine carbon fibers are clearly visible, and a minimal quantity of polymer is deposited on the carbon fiber surface.

The diffusivities and corresponding Da values were calculated at various concentrations of PEI/CO_2 by the method discussed above (**Figure 3-7a, b**). A strong dependence of both parameters on PEI/CO_2 concentration was observed. A rapid decrease in diffusivity and increase in Da were found as the PEI/CO_2 concentration increased from 0 to 3%, consistent with the drastic change in polymer morphology observed in this concentration range.

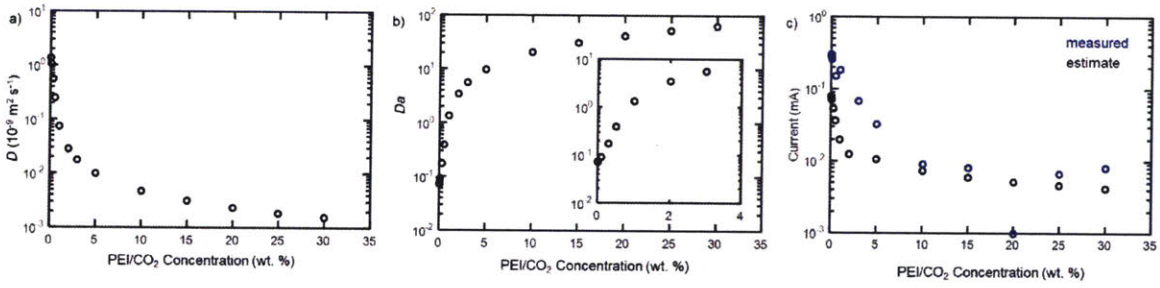

Figure 3-7. (a) Estimated diffusivity of pyrrole and (b) Da at various concentrations of PEI/CO_2 show strong dependence on the concentrations of PEI/CO_2. (c) Estimated (black) and measured (blue) plateau values of the deposition current at different PEI/CO_2 concentration.

The plateau value of the deposition current at different concentrations of PEI/CO_2 can be estimated from the analytic solution of the concentration profile (eq. 3.4). The concentration of pyrrole at the electrode surface was determined by:

$$C_s = C_B\theta(\eta = 0) = C_B \exp(\tau^2) erfc(\tau), \qquad (3.7)$$

The current was estimated from the surface reaction rate using the equation:

$$I = FAkC_s. \qquad (3.8)$$

As τ approaches a large value (i.e. long time), the current can be approximated by (see details in Supporting Information, Section 7):[117, 119]

$$I = FAC_B\sqrt{\frac{D}{\pi t}}. \qquad (3.9)$$

To compare the estimated values with experimental data quantitatively, polymerizations at different PEI/CO_2 concentrations were performed on a glassy carbon electrode with a defined surface area. Consistent with the measured values, the rapid decrease in the predicted plateau deposition current occurs over the same concentration range (0 - 3 %) where the diffusivity and Da vary the most (**Figure 3-7c**). This rapid change in current is due to the transition of the system from a reaction-controlled to a diffusion-controlled regime. The underestimation by the model at low PEI/CO_2 concentrations can be explained by an increase in the effective surface area for deposition as the rapidly growing polypyrrole film extends beyond the defined electrode surface.

3.3. Conclusion

We present an electrochemical approach for constructing a nanostructured conducting polymer coating consisting of polypyrrole nanofibers on a carbon microfiber substrate. In this approach, a safe and low-cost CO_2–bound polyamine was used to induce phase separation at the electrode surface and impose a diffusion limitation on the movement of pyrrole monomers through

the solution, which eventually resulted in the diffusion-limited formation of polypyrrole 1D nanostructures. The porous pPPy has a high specific surface area of 173.5±3.6 m^2 g^{-1} and significantly improved electrochemical properties. A specific capacitance of 370.4 F g^{-1} was achieved, which is a five-fold increase over that for conventionally polymerized PPy. pPPy can be used to adsorb pollutants of environmental interest, with an adsorption capacity of 0.065 mg g^{-1} for aldehydes. The synthesis rates were evaluated in terms of the properties of pyrrole and PEI/CO_2, and the effects of PEI/CO_2 concentration on morphology and current assessed. A reaction-diffusion model was developed to demonstrate that the reduction of monomer diffusivity drove the system into a transport-controlled regime. This concept of exploiting intermolecular interactions to induce phase separation, followed by a transport-controlled reaction process to direct 1D nanostructure growth, can provide meaningful insights into the rational morphological design for a wealth of material systems. The polymerization or co-polymerization of various conducting polymers may be achieved by judicious selection of the interacting functional groups. Other materials systems containing gas-binding functionalities may also be used to assist synthesis of nanostructures, permitting a high degree of modularity of this synthesis concept, and therefore encourage further investigations in this domain. The successful union of porous morphology and electro-responsiveness of pPPy may allow this material to serve as a promising platform for applications in catalysis, separation, energy storage, sensing, or drug delivery. Gas molecules and polymers with additional functionalities can be incorporated in principle, to add suitable functionalities to the system, such as antigen groups for biomedical or biosensing applications, or fluorescence moieties for imaging at nanoscale and studying of polymer morphological changes in situ. Our detailed mechanistic studies reveal the impact of molecular interactions on nanoscale structure formation, which has broad implications for not only nanomaterials synthesis, but also

diverse areas of inquiry ranging from surface sciences to fundamental studies on multi-molecular transport.

3.4. Experimental Section

3.4.1. Materials

Pyrrole, sodium perchlorate, polyethylenimine solution (50 wt.%), acetaldehyde, and butyaldehyde were purchased from Millipore Sigma Corp. They were used without further purification.

3.4.2. Polymer Synthesis

Conventionally synthesized PPy was prepared by electro-polymerization of pyrrole in a solution containing only 0.1 M pyrrole and 0.1 M $NaClO_4$. pPPy was fabricated by the electro-polymerization of pyrrole in the presence of CO_2-bound PEI in an aqueous solution. A deposition solution containing a specified concentration of PEI and 0.1 M $NaClO_4$ in water was sparged with CO_2 for 10 minutes until the pH reached 6.8. Pyrrole monomers were then added so that the deposition solution contained 0.1 M pyrrole. As a comparison, PPy was also prepared in the presence of PEI without CO_2. In this method, HCl was used to titrate the solution pH to 6.8. All electrochemical depositions were performed in a three-electrode system, where Ag/AgCl was the reference electrode, a platinum wire was the counter electrode, and a carbon fiber electrode was the working electrode. A potential of 0.8V was applied to the working electrode while it was immersed in the prepared deposition solution. The polypyrrole formed was directly deposited onto the conductive carbon fiber substrate. Samples were then rinsed thoroughly with deionized water to remove adsorbed PEI and air-dried at room temperature. All electrochemical polymerization experiments were performed with a VersaSTAT 3 potentiostat (Princeton Applied Research).

3.4.3. Polymer Characterizations

The polymer surface morphology was observed by scanning electron microscopy (JEOL 6010LA and JEOL 6700F). The nitrogen physisorption measurements were performed on an automatic volumetric adsorption analyzer (Micromeritics ASAP2020). Fourier transform infrared spectroscopy (FT-IR) was conducted on a Nicolet NEXUS. UV-Vis adsorption spectra were recorded using a Cary 60 UV-Visible spectrophotometer by Agilent Technologies. All the electrochemical characterizations were performed in the same three-electrode systems and with the same equipment as described in the foregoing section.

3.4.4. Aldehyde Adsorption Measurement

The aldehyde adsorption experiments were conducted by immersing polymer/carbon fiber composites in an aqueous solution containing acetaldehyde or butyraldehyde. The concentration of aldehyde was determined via its absorbance peak at around 280 nm with ultraviolet spectrophotometry.[120] The amount of aldehyde adsorbed was determined by the change in the amount of aldehyde remaining in the aqueous solution compared to the control sample. The control sample was prepared following the same procedure with no polymer/carbon fiber composites immersed in it. In this method, it was assumed that no additional aldehyde was lost other than that adsorbed onto the composite.

3.5. Supporting Information

3.5.1. Surface Area Measurement

The surface morphology of pPPy was further characterized by nitrogen physisorption measurement. The Brunauer-Emmett-Teller (BET) surface area was measured to be 173.5±3.6 m^2 g^{-1}, significantly higher than that of the conventionally polymerized polypyrrole (37 - 61 m^2 g^{-1}).[45]

The measured adsorption isotherm exhibits a sharp increase at a relative pressure of around 0.9, with a hysteresis loop over the range of relative pressure from 0.9 to 1 due to capillary condensation in the mesopores (**Figure 3-8a**). The isotherm resembles a Type V isotherm according to IUPAC classification. Based on the Barret–Joyner–Halenda (BJH) theory it was determined that pPPy has a wide pore size distribution that consists mostly of mesopores ranging from 20 to 60 nm in diameter, corresponding to the inter-fiber distance (**Figure 3-8b**).

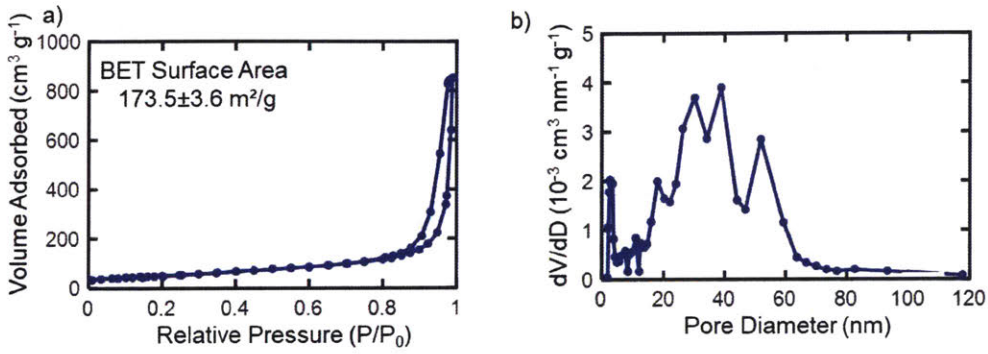

Figure 3-8. The BET surface area (a) and pores size distribution (b) of pPPy/CP was measured via nitrogen adsorption-desorption. P_0 is the saturation pressure of nitrogen at the measurement temperature (~763 mmHg).

3.5.2. Surface Elemental Analysis

The sample surface was analyzed by X-ray photoelectron spectroscopy (XPS) (Surface Science Instruments SSX-100). The measurement was conducted under an operating pressure of ~$2x10^{-9}$ torr and with a flood gun for charge neutralization of the polymer samples. The X-rays were monochromatic Al Kα (1486.6 eV), with a beam size of 1 mm diameter.

XPS survey scans of pPPy, PEI and conventionally polymerized PPy were performed to obtain the atomic percent ratio of N_{1s} to C_{1s} (N/C ratio). PPy and pPPy were deposited on CP as described in main text; PEI was deposited on CP by drop-casting from solution, followed by air-drying. Distinct C_{1s} and N_{1s} peaks were observed in the survey scans of pPPy and conventionally synthesized PPy (**Figure 3-9a, b**). The presence of O_{1s} and Cl_{2p} was due to the doping of ClO_4^- ions during polymerization. The N/C ratio was around 0.5 for PEI and 0.25 for directly polymerized PPy. The analysis of pPPy gives a N/C ratio of 0.24, suggesting only PPy was deposited within the depth of the film over which XPS can detect species (**Figure 3-9c**).

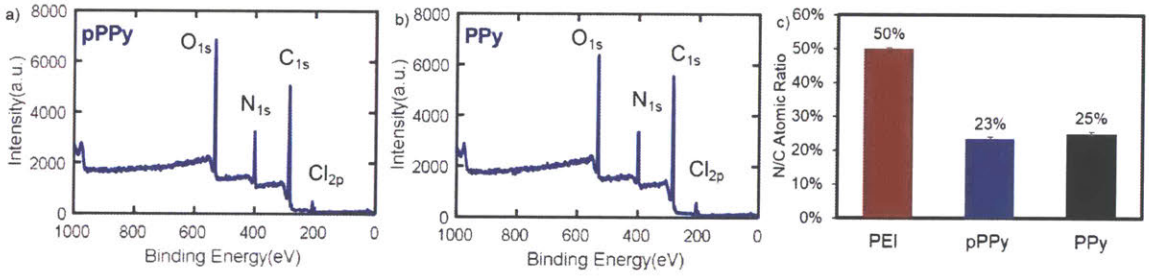

Figure 3-9. XPS survey scans of a) pPPy and b) directly polymerized PPy were performed. c) The calculated N/C atomic ratio indicates that only PPy was deposited at the film surface.

3.5.3. Calculation of Specific Capacitance

Capacitances of both pPPy and PPy electrodes at various scan rates were calculated according to equation S1:[121]

$$\text{Capacitance} = \frac{\int_{V_1}^{V_2} [I_a(V) - I_c(V)]dV}{2(V_2 - V_1)vm}. \qquad \text{(S1)}$$

Here, V_1 and V_2 are the minimum and maximum voltages of the cyclic voltammetry scans. I_a and I_b are the measured anodic and cathode currents. v is the scan rate. The amount of polypyrrole deposited, m, was determined by the total amount of charge consumed during polymerization, assuming that no other reactions occurred at the electrode surface.[99a] Electric double layer charging and water splitting contributed negligibly to charge consumption, as confirmed by measuring the current when applying a potential to the blank electrode in a pyrrole-free electrolyte solution.

3.5.4. Ternary Phase Diagram of PEI/CO_2, Water, and Pyrrole

The existence of a two-phase region in the ternary system of PEI/CO_2, pyrrole, and water was verified experimentally by constructing a phase diagram, shown in **Figure 3-10**, based on cloud point measurements obtained by titration. There are two regions in the phase diagram: a single-phase region at high PEI/CO_2 concentrations, characterized by a homogeneous solution of PEI/CO_2 and pyrrole in water; and a two-phase envelope at low PEI/CO_2 concentrations, composed of a PEI/CO_2-rich aqueous phase in equilibrium with a pyrrole-rich phase. Prior to application of the electric potential, the composition of the deposition solution (point A) is located in the one-phase region. We hypothesize that the oligomerization of pyrrole results in the upward shift of the phase boundary between the one- and two-phase regions, because oligo-pyrrole is less soluble in water than pyrrole monomer is. Consequently, phase separation occurs, resulting in domains of the pyrrole/oligopyrrole-rich phase at the electrode.

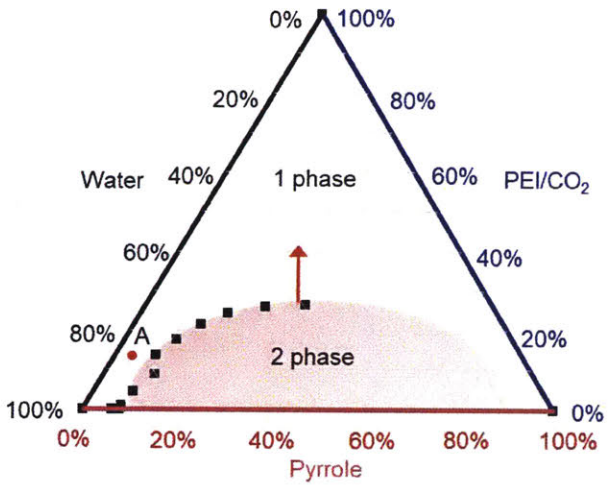

Figure 3-10. Ternary phase diagram of water, pyrrole and PEI/CO_2 shows a two-phase region

3.5.5. Determining the Kinetic Rate Constant

The polymerization of polypyrrole is considered to be a first order reaction:

$$R_h = kC_{pyr}. \qquad \text{(S2)}$$

Electro-polymerization was performed over a range of pyrrole concentrations on a rotating disk electrode at 5000 rpm to eliminate diffusion limitations. The steady state current value can be related to the reaction rate by assuming that the double layer charging is negligible:[122]

$$R_h = I/FA. \qquad \text{(S3)}$$

Here, F is the Faraday constant. A is the surface area of the electrode (0.071 cm^2). From the linear fitting shown in **Figure 3-11**.

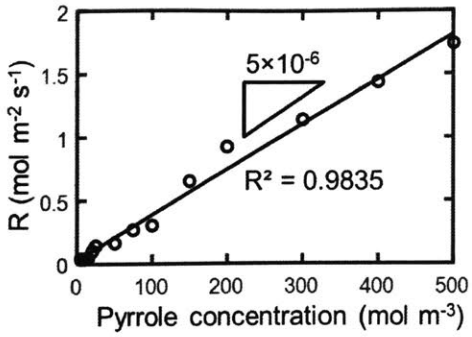

Figure 3-11. Linear fitting of the reaction rate with pyrrole concentration to obtain the first order rate constant for the polymer growth process.

3.5.6. Calculation of Damköhler Number.

The Damköhler number, Da, is defined as the ratio of the characteristic diffusion time to the characteristic reaction time for the process; it is defined as follows:

$$\mathrm{Da} = \frac{kL}{D}. \qquad \text{(S4)}$$

The diffusion layer thickness, L, is defined as the distance from the electrode surface at which the concentration increases to its near-bulk value (when $\eta = 2$, i.e. $x = 4\sqrt{Dt}$, θ approaches 1).[123] Therefore,

$$L = 4\sqrt{Dt}. \qquad \text{(S5)}$$

Da was calculated for the duration of the polymerization process (**Figure 3-12**). Da is much smaller than unity in the system without PEI/CO_2, indicating a reaction-controlled regime. When PEI/CO_2 is present, Da increases to a much larger value than unity for the entire duration of the polymerization process, confirming the polymer growth is a transport-controlled process.

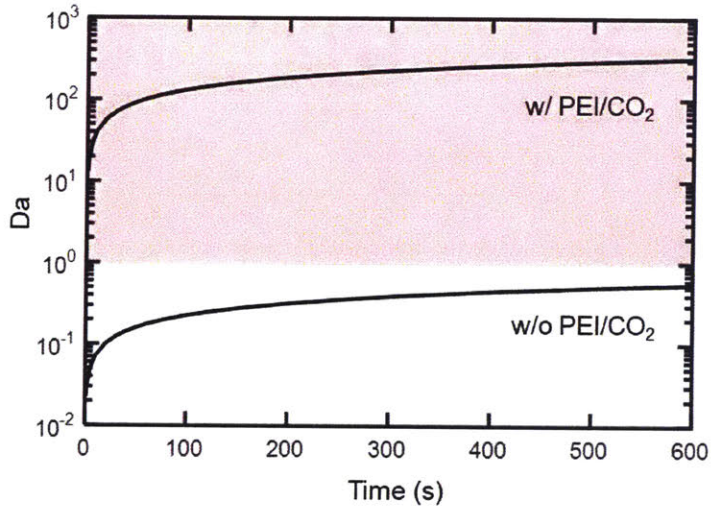

Figure 3-12. Calculated Da in systems with and without PEI/CO2 for the duration of the polymerization process.

3.5.7. Estimating the Current Response at Large τ

Starting with eq. 7 in main text, we take the limit as τ approaches a large value (i.e. long time), using the asymptotic formula

$$\exp(z^2)erfc(z) \approx \frac{1}{\sqrt{\pi}}\left(\frac{1}{z} - \frac{1}{2z^3} + \frac{1\cdot 3}{2^2 z^5} - \ldots\right). \quad \text{(S6)}$$

The concentration at electrode surface is therefore simplified to:

$$C_s = C_B \frac{1}{\tau}\sqrt{\frac{1}{\pi}}. \quad \text{(S7)}$$

Plugging in for τ, we obtain:

$$R_h = kC_s = C_B\sqrt{\frac{D}{\pi t}}. \quad \text{(S8)}$$

Substitution of the above equation into eq. 8 of the main text leads to eq. S9 below:[117, 119]

$$I = FAC_B\sqrt{\frac{D}{\pi t}}. \quad \text{(S9)}$$

Acknowledgement

This research was supported by Philip Morris International (Neuchâtel, Switzerland). We would like to thank the Institute for Soldier Nanotechnology at MIT for the use of facilities. This work also made use of the Cornell Center for Materials Research Shared Facilities which are supported through the NSF MRSEC program (DMR-1719875).

Chapter 4. Application of Nanostructured Conducting Polymer Composite in Adsorbing Polynucleotides

With the advancement of sequencing technologies, DNA has been playing an increasingly crucial role in biological research and clinical diagnosis. The current purification methods based on solid phase extraction has disadvantages of high cost and low consistency. The tunable conductivity and charge carrier level in conducting polymers provide opportunities to achieve electrochemically controlled separation of charged molecules. Polynucleotides comprising negatively charged phosphate-sugar backbones, which can electrostatically interact with the positively charged carriers in polypyrrole backbones. In this work, we achieved electrochemically controlled adsorption of polynucleotides by modulating the doping levels in the π-conjugated system. The adsorption performance demonstrated a dependence on the oxidation states of polypyrrole chains, as a result of the correlation between the oxidation state and the charge level in conjugated polymers. This finding can serve as an alternative principle in developing DNA purification systems and has fundamental implications for advancing next generation non-viral gene delivery technologies.

4.1. Introduction

The wide use of polymerase chain reaction and sequencing enabled DNA in providing insights into biological analysis research. DNA not only aids clinical diagnosis and biological studies, but also plays a role in colloidal particle assembly, molecular electronics, and material preparation.[124] However, the use of DNA is challenged by the presence of proteins, small organic

molecules, polysaccharides, and phospholipids in cellular matrix or environmental samples.[125] Therefore, the extraction and purification of nucleic acids play a crucial role in the success of downstream sequencing and molecular assays.

Existing purification methods of DNA involve liquid extraction with phenol-chloroform. The use of organic solvent can lead to the degradation of nucleic acid and a time-consuming and labor-intensive centrifugation process. Many commercially available DNA purification kits relying on solid phase extractions, though can obtain high purity DNAs, have high cost and low consistency.[125] The need for portability and a nonhazardous chemical process call for the development of a new separation system for polynucleotides.

Conducting polymers with tunable conductivity and charge carrier property are a promising platform for exploiting electrochemically controlled electrostatic interactions with charged molecules to achieve desirable separations. In particular, polypyrrole with π-conjugated backbones are stimulus-responsive. It can be electrochemically switched between an oxidized and a reduced state, which accompanies the inserting and de-inserting of counter ions within the polymer bulk. DNA consisting of nucleotides has a negatively charged backbone from the alternatively arranged deoxyribose and phosphate groups. Electrostatic interactions and ion-exchanges can drive the adsorption and desorption process as polypyrrole is switched between different redox states.[4c, 126] The electro-responsive and ion-exchange properties, along with the biocompatibility[127] of PPy make it a promising platform for biomolecule separation, especially in point-of-care applications.

Here, a porous polypyrrole-modified electrode (pPPy) was developed to electrostatically adsorb polynucleotides. The porous-polymer modified electrode consists of nanostructured polypyrrole coatings on carbon microfibers. The unique morphology provides a large accessible surface area for polynucleotides to interact with polypyrrole chains. The selective and reversible

adsorption of DNAs was carried out by inducing changes in the redox states of the nanostructured polypyrrole. The adsorption of DNA was confirmed by surface elemental analysis and cyclic voltammetry (CV). UV-Vis and CV titrations were used to study the interaction between DNA and PPy, through which the electrostatic interactions were found to be the main driving force. The successful modulation of the porous conducting polymer as a platform in separating charged genetic materials opens a new door to the development of an alternative inexpensive non-viral delivery method in next generation gene therapies.

4.2. Results and Discussion

4.2.1. Surface Morphology and Electrochemical Properties of pPPy

The adsorption of DNA by polypyrrole relies on their intermolecular interactions which highly depend on the accessibility of DNA towards polypyrrole chains. Therefore, the surface morphology of polypyrrole-modified electrodes plays a crucial role in the adsorption performance. We evaluated the morphological properties using scanning electronic microscopy (SEM). The pPPy electrode exhibits as a porous polymer coating deposited on carbon microfibers (**Figure 4-1a**). The polymer coating comprises fibrous structures with diameters of approximately 100 nm. Polypyrrole that was fabricated by conventional methods exhibit as a thick coating (**Figure 4-1b**), therefore has a much lower specific surface area.[83]

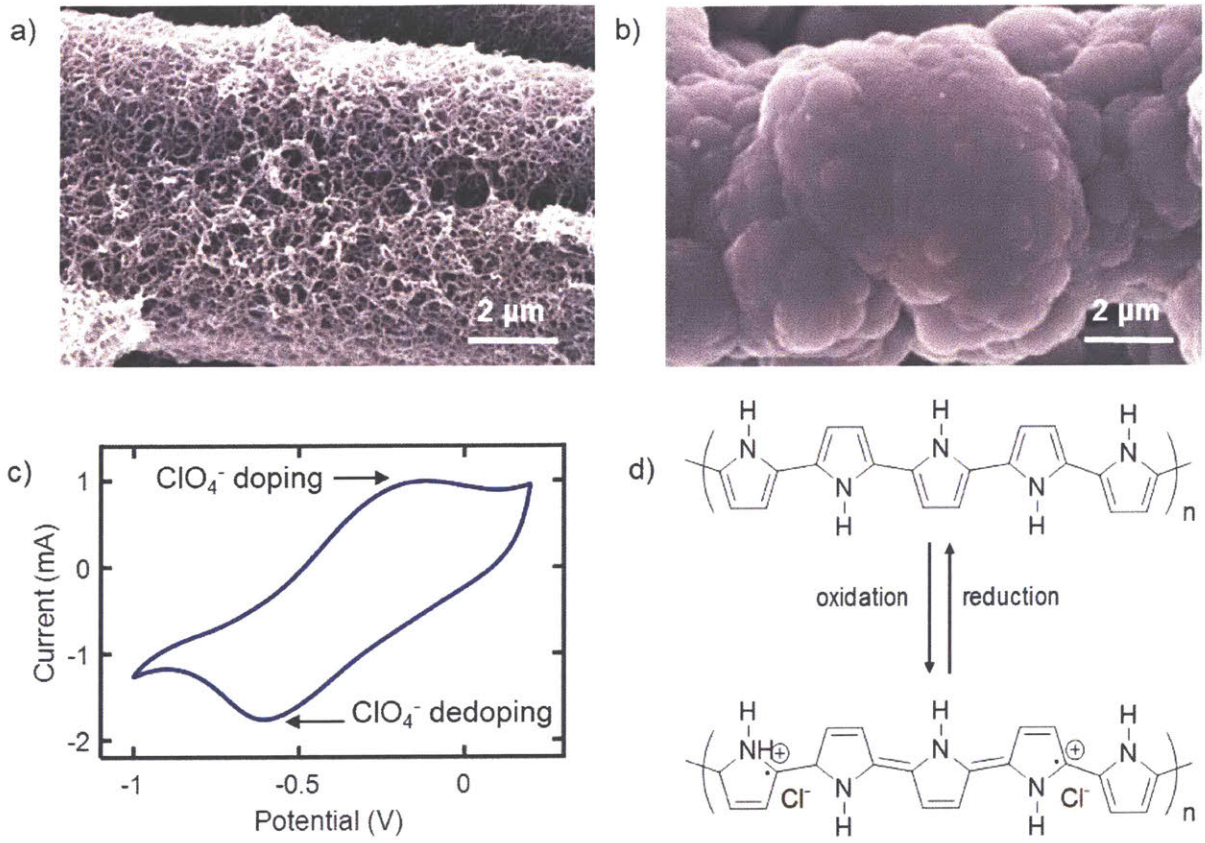

Figure 4-1. SEM images show PPy (a) has a thick non-porous morphology, while pPPy (b) is a porous coating consisting of nanofibroud structures. (c) Cyclic voltammogram of pPPy in 0.1 M $NaClO_4$ exhibits the redox peaks corresponding to the doping and dedoping process. (d) Schematics shows the change in molecular structures of polypyrrole upon oxidation and reduction.

The electrochemical tunable nature of polypyrrole stems from the redox responsiveness of its conjugated backbones, which can be evaluated via cyclic voltammetry. The doping/dedoping of cations within PPy film resulted in broad peaks in both the anodic and cathodic scans in the cyclic voltammogram (**Figure 4-1c, d**).[128] The forward scan exhibits a single anodic peak, corresponding to the oxidation of PPy and the insertion of negatively charged ClO_4^-. The presence of the single peak in the reverse scan indicates the oxidation of PPy is reversible. The degree of oxidation can be estimated by:[128c]

$$\frac{Q_{CV}}{Q_{syn}} = \frac{\rho}{2+\rho}. \quad (4.1)$$

Q_{CV} is the total charge passed to PPy during the anodic scan up to 0.2 V, Q_{Syn} is the amount of charge consumed during the polymerization. Both Q_{Syn} and Q_{CV} were determined by integrating the corresponding current response over time. By assuming a 100% polymerization efficiency, the degree of oxidation, ρ, was determined to be 0.3, therefore each positive charge was shared by three pyrrole units in the oxidized pPPy.

The adsorption performance of PPy can be impacted significantly by the effective electrochemical surface areas (ESA). We evaluated ESA by measuring the cyclic voltammogram of PPy deposited on a glassy carbon electrode (GCE) in the presence of a redox indicator, $K_3Fe(CN)_6$ / $K_4Fe(CN)_6$. The peak potential separation, ΔE_p (= $E_{pc} - E_{pa}$), increases as the scan rate increases due to the slow electrode kinetics, suggesting a quasi-reversible process at the electrode surface (**Figure 4-2a, d**). The peak current of PPy, i_p, has a linear dependence with the square root of the scan rate (**Figure 4-2b, c, e, f**), indicating a diffusion controlled process based on the Randles-Sevcik equation:[129]

$$i_p = (2.687\times10^5)n^{3/2}v^{1/2}D^{1/2}AC. \quad (4.2)$$

Here A is the electrode surface area (cm^2). C is the bulk concentration of $Fe(CN)_6^{3-}$ (10 mM). D is the diffusion coefficient of $Fe(CN)_6^{3-}/Fe(CN)_6^{4-}$ (5.7×10^{-6} cm^2 s^{-1}).[130] v is the scan rate used. n is the number of electrons transferred (n=1). The ESA of the GCE electrode was determined to be 0.09 cm^2, comparable to its geometric surface area of 0.071 cm^2. The determined ESA of pPPy-modified GCE was 0.20 cm^2, which is a 2.3-fold increase compared to that of pristine GCE, confirming the advantage of the nanofibrous morphology of pPPy.

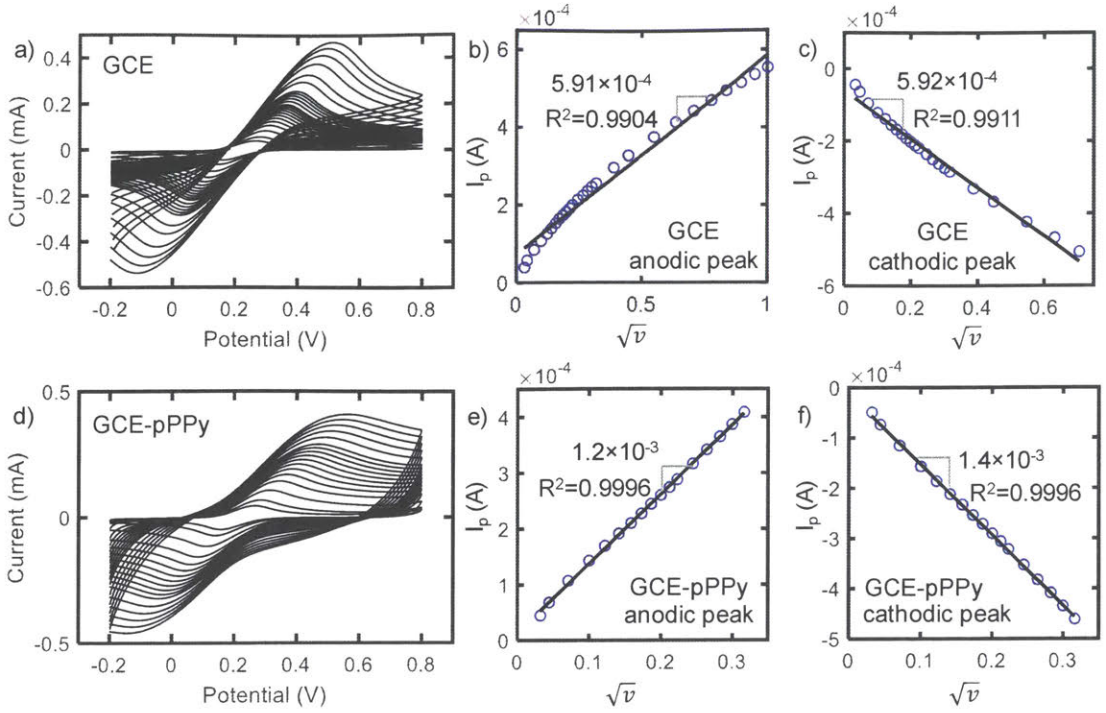

Figure 4-2. CV current responses of $Fe(CN)_6^{3-}/Fe(CN)_6^{4-}$ at the electrode surface of (a) GCE and (b) pPPy-modified GCE at various scan rates. The anodic peak currents (b, e) and cathodic peak currents (c, f) were linear fitted to obtain the ESAs.

4.2.2. Study of DNA and pPPy Interactions

Two major modes of interactions between DNA and PPy are possible based on their molecular structures: hydrophobic and electrostatic interactions.[131] The repeating units of polypyrrole is aromatic and planar, which can potentially fit in between the stacked DNA base pairs via hydrophobic interaction or intercalation. Alternatively, the positive charges along the oxidized PPy backbone can electrostatically interact with the negatively charged sugar-phosphate backbone.[132] To further decipher the adsorption mechanism, UV-vis and CV titrations were performed.

Study intermolecular interactions by UV/Vis titrations

Spectroscopic studies can sensitively unveil the molecular mode of interactions. Since pyrrole has no absorption above 250 nm, the observed variance of peak intensity at 260 nm is attributed to the formation of the complex between pyrrole and DNA. As the concentration of pyrrole increases, the absorbance between 200-250 nm intensifies and the peak at 260 nm diminishes significantly (by ~25%) with little shift in peak position (**Figure 4-3a**). This change in absorbance intensity gave rise to an isosbestic point at around 250 nm. The isosbestic point shifted gradually to the right as more pyrrole was added, showing spectroscopically that the complexation proceeded in a stepwise fashion, instead of randomly.[112a, 115]

The formation constant of the complexes was determined from the Benesi-Hildebrand equation:

$$\frac{A_0}{A-A_0} = \frac{\varepsilon_{pyr}}{\varepsilon_{pyr-DNA}-\varepsilon_{pyr}} + \frac{\varepsilon_{pyr}}{\varepsilon_{pyr-DNA}-\varepsilon_{pyr}} \times \frac{1}{KC_{pyr}}, \quad (4.3)$$

with the assumption of 1:1 binding stoichiometry/host-to-guest complex formation ratio and the condition that guest concentration is in excess of that host.[133] Here, A_0 and A are the absorbance of free DNA and DNA in the presence of pyrrole, respectively. ε_{pyr} and ε_{DNA} are the adsorption coefficients of pyrrole and DNA in water. C_{pyr} is the concentration of pyrrole. $K_{DNA\text{-}Pyr}$ is the binding constant between DNA and pyrrole. By plotting $A_0/(A-A_0)$ vs. $1/C_{Pyr}$, $K_{DNA\text{-}Pyr}$ can be obtained by taking the ratio of the intercept and the slope. $K_{DNA\text{-}Pyr}$ was determined to be 6.6 M^{-1}. The linear fit has a correlation coefficient of 0.9932, supporting the assumed 1:1 complex ratio between a nucleotide base pair and a pyrrole unit (**Figure 4-3b**). The change in Gibb's free energy,

$\Delta G = -RT \ln K$, was calculated to be -4.6 kJ/mol. The negative value of ΔG further confirmed the binding between DNA and pyrrole was spontaneous.

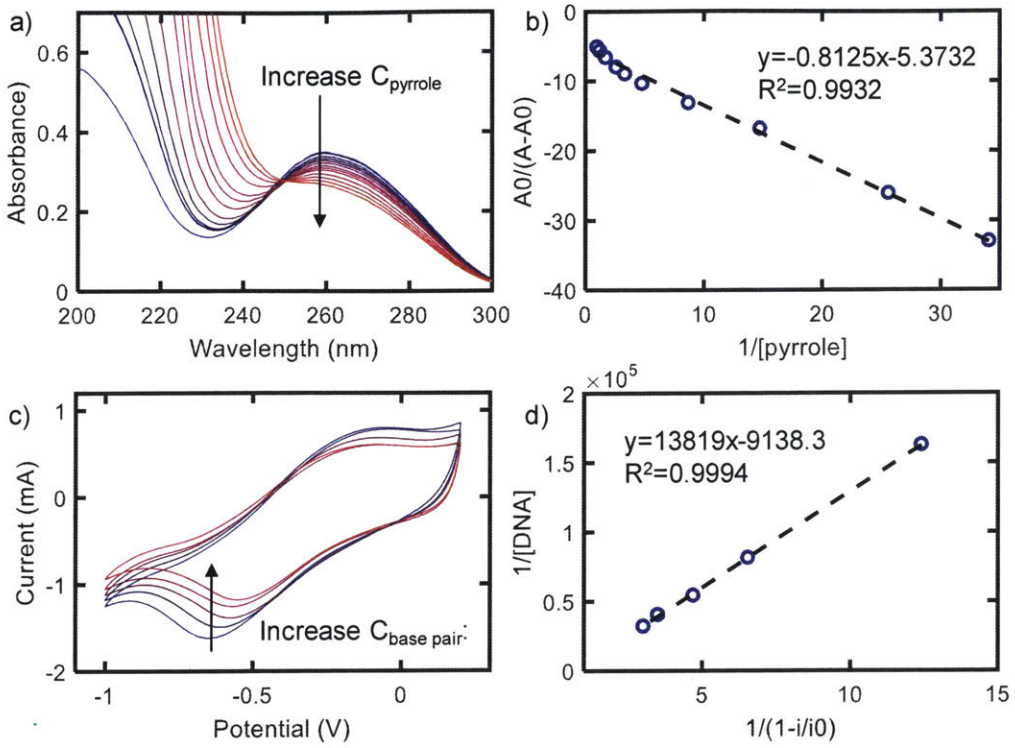

Figure 4-3. (a) The UV-Vis absorbance of DNA changes with the increasing concentrations of pyrroles. (b) The fitting of UV-Vis absorbance data with Benesi-Hildebrand equation. (c) Cyclic voltammogram of pPPy with the increasing concentrations of DNAs. (d) The fitting of CV cathodic peak currents based on equation 4.5.

Study intermolecular interactions by cyclic voltammetry

Voltammetric studies of DNA-PPy complex was performed with calf thymus DNA. In the presence of DNAs, a gradual decrease in the peak current was observed, likely due to the coverage of an insulating layer of DNAs at the electrode surface.[134] DNA also has a lower diffusion coefficient compared to ClO_4^- ions, as DNA served as the counter ion to insert into the polymer upon oxidation. The binding constant between DNA and PPy, $K_{DNA\text{-}PPy}$, can be calculated via

$$\frac{1}{C_{DNA}} = \frac{K_{DNA-PPy}(1-A)}{1-(\frac{i}{i_0})} - K_{DNA-PPy}, \quad (4.4)$$

where i and i_0 are the peak currents of PPy in the presence and absence of DNA, respectively.[135] A is a proportionality constant. Here, a 1:1 complex ratio between a DNA base pair and a PPy repeating unit was assumed. The condition that the concentration of DNA was in excess of PPy was met. The linear regression for fitting $1/C_{DNA}$ with $1/(1-i/i_0)$ gave a linear correlation coefficient of 0.9994. The corresponding $K_{DNA\text{-}PPy}$ was determined to be 9138 M^{-1}. The free energy of binding, $\Delta G_{DNA-PPy} = -RT \ln K_{DNA-PPy}$, was then calculated to be -22.2 kJ mol^{-1}, the large negative value of which suggests the binding process is spontaneous and the formed DNA-polypyrrole complex is stable. $K_{DNA\text{-}PPy}$ is much larger than $K_{DNA\text{-}Pyr}$, likely because 1) oxidized PPy possesses positive charges to electrostatically interact with the negatively charged phosphate groups in nucleotides; 2) PPy has an extended resonance structure and can delocalize the positive charges along its aromatic backbone. The mobility of the positive charged defects allows flexible and continuous multi-point contacts with the linear calf thymus polynucleotides.[136] As manifested by the small value of $\Delta G_{DNA\text{-}Pyr}$, the hydrophobic interaction between DNA and pyrrole is relatively weak and contributes marginally toward the adsorption of DNA by PPy when oxidized. The

intercalation of a large molecule, PPy, into DNA was less likely. Therefore, the DNA-PPy complex formation is mainly driven by Columbic electrostatic interactions. This mode of interaction is likely beneficial for avoiding the DNA structural disruption that is commonly caused by the intercalation occurring between the base pairs of DNA double helix.[131, 137]

4.2.3. Electrochemically Controlled Adsorption of DNA by pPPy

Adsorption study was performed on CF, PPy, and pPPy with different oxidation states (**Figure 4-4**). Negligible amount of DNA was removed from the solution by CF as the hydrophobic interactions between the CFs and the aromatic bases of DNA is minimal. Non-porous PPy prepared by the conventional method adsorbed limited amount of DNA because its compact polymer morphology provided limited polymer/solution interface for DNA to interact with its positive charge carriers. The unique structure of the porous pPPy electrode allows more exposure of the positive charges in its backbones, therefore has much improved adsorption capability towards DNA. The pre-oxidation procedure eliminated the possibility of damaging DNAs that is caused by directly applying a positive potential to electrodes contacting DNAs.

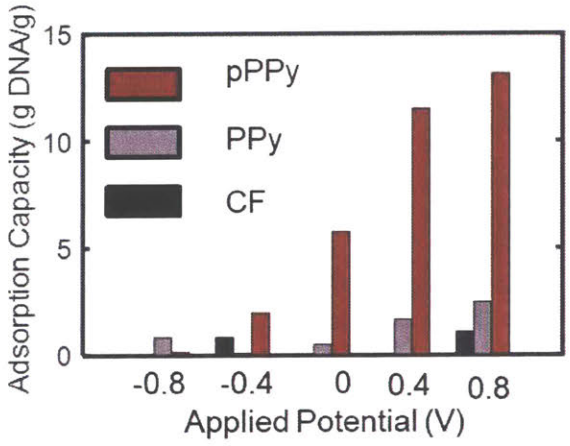

Figure 4-4. Adsorption capacity of pPPy (red), PPy (grey), and CF (black) towards DNAs at various potentials.

The adsorption capability of pPPy also exhibited a clear dependence on its oxidation states. Here, an increasing amount of DNA adsorption coincided with the increasing oxidation potential that was applied to the electrode prior to adsorption, demonstrating the tunable nature of the adsorption process by an external electro-stimulus. This modularity stemmed from the control of the generation of charge carriers in polypyrrole by the oxidation potential. To further analyze the adsorption dependence on oxidation states, the level of positive charged defects was estimated by the charge transferred upon polarization of the electrodes at a specific potential until the current reaches zero, assuming the contribution from the electric double-layer charging of the substrate is negligible. The utilization efficiency of the polypyrrole electrode was determined as the percentage of the amount of charged defects at an oxidation potential to the total amount of charges required during synthesis (**Figure 4-5**). pPPy exhibited an improved utilization efficiency compared to non-porous PPy due to the improved morphology.

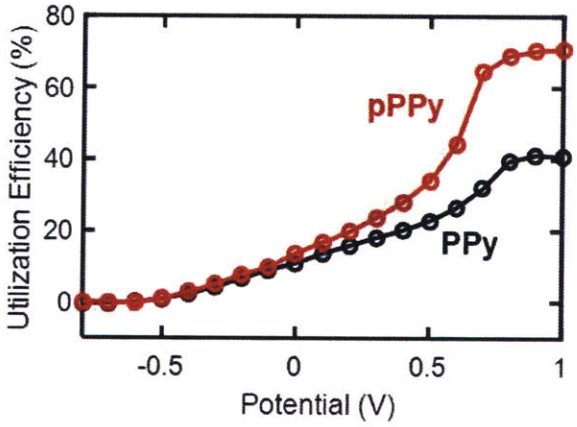

Figure 4-5. Utilization efficiency of pPPy and PPy electrodes as determined by taking the ratio of the amount of charged defects at an oxidation potential to the total amount of charges required during the synthesis.

Surface elemental analysis provides a direct confirmation of DNA adsorption on polymer surface. Tris buffer was used during the adsorption experiments to avoid the introduction of phosphate groups from buffer solutions such as phosphate buffers. After DNA adsorption, the XPS spectra of PPy at different oxidation potentials all display distinct C_{1s}, N_{1s} and O_{1s} peaks (**Figure 4-6a**). A concomitant increase of P_{2p} (134 eV) and Cl_{2p} (200 eV) peaks was observed as the oxidation state increased. The appearance and gradual increase of P_{2p} peak are assigned to the phosphate groups from DNA. The Cl_{2p} is from the Tris buffer and the dopant used during polymerization. The atomic percent of P_{2p} and O_{1s} were determined to coincide with the increase in polypyrrole oxidation states (**Figure 4-6b, c**). This is mostly attributed to the increasing adsorption of DNAs as polypyrrole carries more positive charge defects at a higher oxidation state. The estimated amount of charges vs. potential curve exhibits a sigmoidal shape, characteristic of the Nernst relations. Both the adsorption capacity of pPPy and the atomic percent of P_{2p} showed a similar potential dependence as predicated by the Nernstian relation. This change in surface elemental composition further demonstrates the strong dependence of DNA adsorption on the oxidation state of polypyrrole chains.

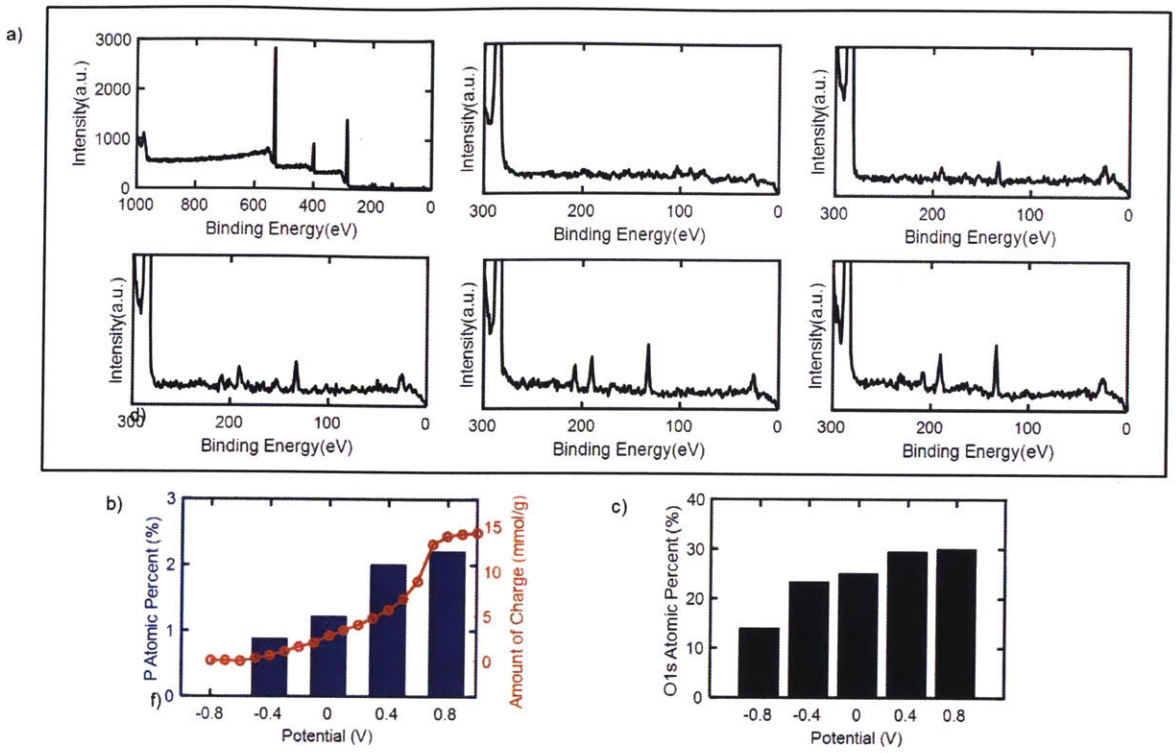

Figure 4-6. (a) XPS scans of pPPy electrodes at different oxidation potentials after adsorbing DNAs indicate the concomitant increase of P_{2p} and Cl_{2p} peaks. (b) The atomic percent of P_{2p} at pPPy electrode surface as determined by XPS analysis and the calculated amount of charge in pPPy at various potentials. (c) The atomic percent of O_{1s} at pPPy electrode surface as determined by XPS analysis at various potentials.

To evaluate the reversibility of the adsorption process, a pPPy electrode that was previously adsorbed with DNA was reduced to its neutral state by applying different reduction potentials to remove the surface charge. A constant potential of -0.8V and -0.4V was applied to the electrode for a period of time until the current reached zero to reduce the polypyrrole to its neutral state. The desorption experiments were carried out by immersing the DNA-loaded electrodes in 5 mLof 0.1 M Tris-HCl solution. The desorption efficiency was calculated by taking the ratio of the amount

of DNA remaining on the electrode after reduction to that was initially adsorbed in the oxidized state. In its reduced state, the assembled DNAs were liberated from the polymer matrix and the surface of the polymer film. When no potential was applied to the electrode, a 22% of desorption efficiency was observed due to the diffusion of DNA from the electrode surface to solution (**Figure 4-7**). When completely reduced to its neutral state by applying a -0.8V potential, the electrode has a 62% desorption efficiency, which is 20% higher than that of the partially reduced electrode (-0.4V). The tunable control of DNA release into a physiological pH and solution environment has great implications for its development in smart gene delivery

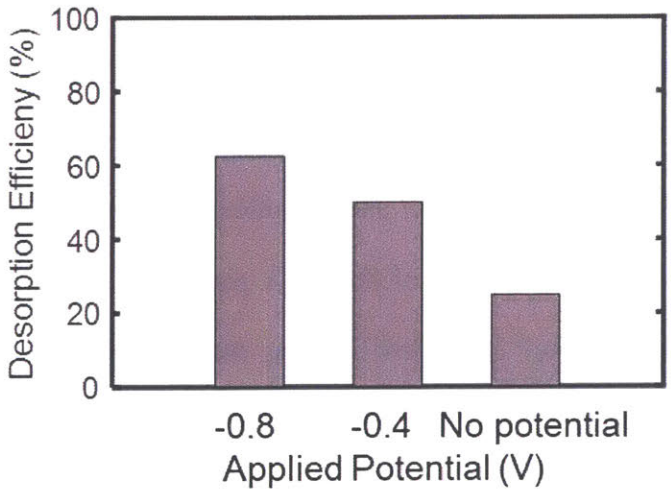

Figure 4-7. The desorption efficiency of pPPy when various reduction potentials were applied to the electrode.

The adsorption of DNA at the polymer surface can be further confirmed by cyclic voltammetry "blocking" experiments. Here, the blocking effect was assessed by the degree to which an adsorbed layer of molecules inhibits the redox reaction of a redox probe at the electrode surface.[138] $K_4[Fe(CN)_6]$ was used again as the redox probe since it does not interact with DNA or

PPy, and has been frequently used for studying the barrier properties of monolayer coated electrodes.[139] The cyclic voltammogram of pPPy after DNA adsorption was recorded and compared with that of clean and pPPy coated GCE (**Figure 4-8**). Clean GCE exhibits well-defined oxidation and reduction peaks of $Fe(CN)_6^{3-}/Fe(CN)_6^{4-}$. pPPy coated GCE exhibits broad quasi-rectangular current profile in addition to two distinct redox peaks. The broad CV response across the entire voltage window is attributed to the redox reactions of polypyrrole. The redox peaks have a magnitude ~3 times of that for the clean GCE, as a result of the increased ESA. After DNA adsorption, both the redox peaks and the current response corresponding to PPy redox reaction were significantly suppressed. Since the adsorption of DNA at the electrode surface did not result in blockage of the pores or ion diffusion path as evidenced by SEM (**Figure 4-9**), this suppression is likely a result of the coverage of non-conducting DNA at the PPy surface.[129] The binding of DNAs insulated the electrode surface and significantly perturbed the interfacial electron transfer.[140] The electronegative nature of the DNA phosphate backbone also has electrostatic repelling effect with $[Fe(CN)_6]^{3-}$, therefore blocking the redox reaction of $Fe(CN)_6^{3-/4-}$ with the electrode.[138, 141] This observed blocking effect provided additional evidence for the adsorption of DNA by pPPy.

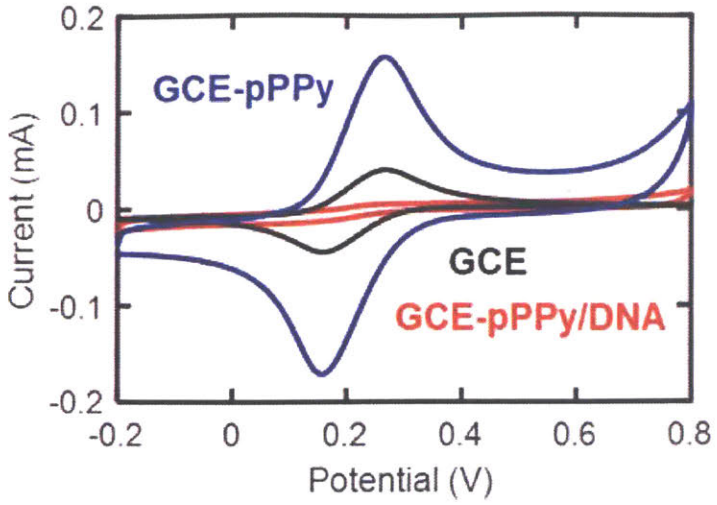

Figure 4-8. Cyclic voltammograms of GCE, GCE-pPPy and GCE-pPPy/DNA demonstrate the "blocking effect" of DNA adsorptions.

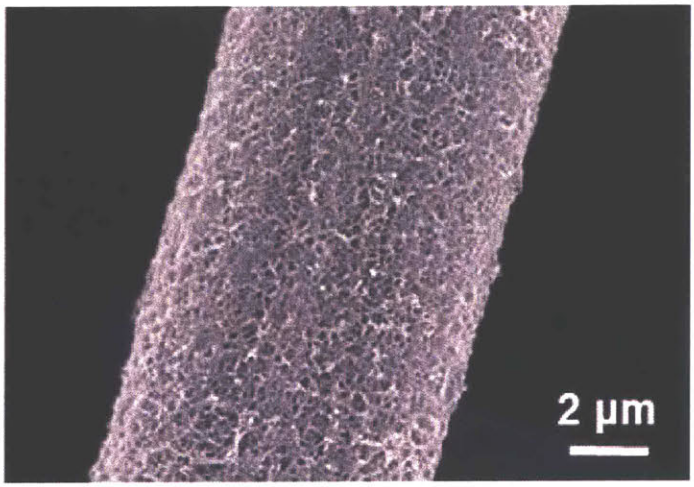

Figure 4-9. SEM image of pPPy after adsorbing DNAs shows no morphological changes compared to newly-prepared electrodes.

4.3. Conclusions

We present an electrochemically tunable method to adsorb and release polynucleotides using a nanostructured conducting polymer and carbon fiber composite. The nanostructured composite comprising a carbon microfiber substrate and a porous polypyrrole fibrous film synthesized via a novel electrochemical method. The system demonstrated an adsorption dependence on the polymer oxidation state. By electrochemically modulating the oxidation state of the polymer, the amount of positive charge carriers in the composite can be manipulated. We therefore achieved the control of the electrostatic interactions between the composite and the negatively charged polynucleotides. The porous polypyrrole composite demonstrated improved adsorption compared to its nonporous counterpart as a result of the large surface area and improved film morphology. The electrochemically controlled adsorption of DNAs can serve as an alternative principle in developing DNA purification systems and provide meaningful insights for advancing next generation non-viral gene delivery technologies.

4.4. Experimental Section

4.4.1. Materials

Calf thymus DNA was purchased from Millipore Sigma Corp. and used as received. 1 mg mL^{-1} of stock solution was prepared with 0.05M Tris-HCl buffer (Millipore Sigma, pH 8) and stored at 4 °C.

4.4.2. Procedures

Electrochemical polymerization and characterization

Toray carbon paper consisting of carbon microfibers were used as a substrate. Porous polypyrrole was deposited on the 1 cm by 2 cm substrate by an electrochemical method that was developed previously in our research group. All electrochemical polymerization and characterization experiments were carried out in a three-electrode system, with a platinum wire as the counter electrode and a Ag/AgCl reference electrode. 10 mM Tris-HCl (pH 7.4) was used as the buffer solution for characterization with DNAs.

Material characterizations

The surface morphologies of polymer electrodes were evaluated using scanning electron microscope (JEOL 6010LA and JEOL 6700F). Adsorption spectra were recorded using Cary 60 UV-Visible spectrophotometer by Agilent Technologies. The concentration of DNA was measured by UV/Vis spectroscopy with molar extinction coefficients of 13200 bp $cm^{-1}M^{-1}$ (base pair).[132, 142] Standard calibration curves for DNA absorbance at 260 nm were also obtained for consistency check. The UV-vis absorption of DNA in 50 mM NaCl/5 mM Tris, pH 7.1 gave a A260/A280 ratio of 1.7-1.8, which indicates the DNA sample was sufficiently free of protein[132, 143]. The ability of PPy to bind with DNA was investigated using a UV-visible absorption titration method. It was carried out by monitoring changes in the UV absorption at 260 nm as more pyrrole was added into the solution. Protein concentration was determined by mixing samples solutions with Bradford reagent (Millipore Sigma Corp) and measured via UV absorbance at 595 nm. X-ray photoelectron spectroscopy (XPS) analysis was conducted using Surface Science Instruments SSX-100 under an operation pressure of ~$2x10^{-9}$ Torr. A flood gun was used for charge neutralization of the polymer samples. The monochromatic Al Kα x rays (1486.6 eV) used had a beam size of 1 mm diameter. The XPS spectra were analyzed with CasaXPS. The surface

composition was determined by the integrated peak areas of C1s, N1s, O1s, Cl2p, and P2p with the respective sensitivity factors.

Adsorption experiments

Prior to adsorption experiments, prepared PPy electrodes were subjected to a constant potential for a period time until the current reaches zero. In this way, PPy was switched to a specific oxidation state. The constant potential used were –0.8 V, -0.4 V, 0 V, 0.4V, and 0.8V. Pristine carbon fiber substrate (CF) and carbon fibers coated with non-porous polypyrrole (PPy) were used as controls. The adsorption of DNA was carried out in a glass vial containing 0.1 mg mL^{-1} DNA in Tris-HCl buffer. The concentration of DNA was determined by measuring its UV-Vis absorbance at 260 nm. The amount of DNA adsorbed was calculated based on:

$$Q_t = \frac{(C_0 - C_t)V}{M}, \quad (4.5)$$

where C_0 is the solution initial concentration, C_t is the solution concentration measured at equilibrium, V is the solution volume, and M is the mass of the polypyrrole.

Acknowledgement

This research was supported by Philip Morris International (Neuchâtel, Switzerland). We would like to thank the Institute for Soldier Nanotechnology at MIT for the use of facilities. This work also made use of the Cornell Center for Materials Research Shared Facilities which are supported through the NSF MRSEC program (DMR-1719875).

Chapter 5. Conclusions and Future Work

5.1. Conclusions

The principal focus of this thesis was to investigate and develop new synthesis strategies for nanostructured electroactive polymeric composites with desired properties and morphologies for energy storage and separation applications. The thesis discusses the synthesis, properties, and applications of nanostructured electroactive polymeric composites and provides useful insights that can extends far beyond the discussed polymer hybrids and potentially be generalized for future advancement of energy storage devices and separation technologies.

To achieve this, we developed two novel synthesis strategies by exploring two different non-covalent inter-molecular interactions to influence the electrochemical polymerization process. In the first approach, the π-π stacking interactions between aromatic monomers and the aromatic components of metallocene moieties were utilized to synthesize a porous conducting polymer hybrid. In particular, the pyrrole monomers possessing a five-membered aromatic ring can interact with the cyclopentadiene ring in polyvinylferrocene. This interaction resulted in a phase separation during pyrrole polymerization as oligopyrrole preferentially partitioned into the pyrrole-rich phase and eventually led to the formation of nanospheres comprising PVF and PPy. The electro-responsiveness and the high surface area associated with the electroactive polymer nanostructures imply great potentials in energy storage and separation applications. The PVF/PPy hybrid was extensively studied for its application as a supercapacitor electrode material. We demonstrated the porous morphology shortened the transport pathway for electrolyte ions and improved the ionic conductivity. The synergistic effect between PVF and PPy allowed PPy to serve as a molecular wire to enhance the electronic conductivity. The fast one-electron redox reaction occurring at the

ferrocene moieties of PVF contributed additional charge storage capacity. As a result, the porous hybrid achieved significantly enhanced energy storage rate performance and specific capacitance.

In the second approach, the interactions between aromatic monomers and carbamate groups of a CO_2 –bound polyamines played a role in inducing phase separations and imposing diffusion limitations during the polymerization and deposition process. The transport-limited condition directed the growth of polypyrrole 1D nanostructures, resulting in a porous PPy fibrous film. The porous PPy film-modified carbon microfiber electrode was found to exhibit enhanced CV current responses and improved adsorption capacity towards aldehydes, compared to its non-porous counterpart. We later applied the porous polypyrrole electrode in achieving electrochemically controlled adsorption of polynucleotides. The affinity of PPy towards DNAs was found to be mainly driven by electrostatic interactions between positively charged PPy backbones and negatively charged phosphate groups. As a result, the adsorption of DNA exhibited a dependence on the oxidation state of the polymer, which allowed us to achieve an electrochemical control over the adsorption process.

The conductive substrate also plays an integral role in the synthesis and analysis of electroactive polymer composites. In this thesis, we introduced nanostructures in the construction of conductive substrates to enhance their performance. Carbon nanofibers were fabricated via electrospinning, followed by stabilization and carbonization. A simple and quick dip-coating method was developed to easily incorporate electrospun CNFs into a CMF scaffold to form a CNF/CMF composite with improved conductivity and structural integrity as a deposition substrate.

5.2. Recommendations for Future Work

The research presented in the thesis is expected to stimulate interests in exploiting molecular interactions to engineer polymeric nanostructured materials and encourage further investigations into applying such materials in a wide range of applications. Several future research directions are worth exploring.

- In the method for fabricating polypyrrole 1D structures, a multiphase-diffusion-controlled electrochemical deposition mechanism was proposed. Despite the various experimental evidences supporting the mechanism, observing the nanostructure formation process via an in situ technique can reveal more direct insights on the polymerization mechanism. Data generated using in situ TEM, SEM, or AFM technique may give a more complete picture of the deposition process.
- There are still many challenges remaining in applying the porous PPy system to extract and purify DNAs. Functionalization of the system with tailored molecular design that poses specific interactions with intra-cellular contaminants, such as lipids and surfactants, *etc.*, is needed before this system can be served as a viable option in point-of-care devices.
- In the thesis, carbon nanofibers were introduced to engineer the conductive substrate. Alternative nanostructured carbonaceous materials, such as carbon nanotubes and activated carbons, can also serve as a conductive framework and provide support for mechanical strains during doping/de-doping processes. Direct incorporation of nanoscale carbon materials into polymeric composites during polymerization can be explored to further enhance the morphological and electrochemical properties.
- The applicability of the synthesis approaches in a broad range of conducting polymers and redox polymers is of great interest for applications such as sensing and catalysis. In

particular, nanostructured polymeric hybrids containing a variety of metallocene systems, such as zirconocene, ruthenocene, titanocene, *etc.*, can be beneficial for catalysis applications.

- The electro-responsive property and porous morphology of the discussed materials also bode promise for sensing applications. The interactions between conducting polymer and specific target molecules can increase or reduce the charge mobility along the conjugated backbone. Consequently, a change in conductivity can be measured. In particular, polypyrrole has been extensive studied to immobilize biological molecules in designing bioanalytical sensors for detecting glucose, DNA, proteins, *etc.* The porous polypyrrole system can be explored to serve as an excellent platform for incorporating bio-relevant entities in sensing applications.

Chapter 6. Appendix: Development of Nanostructured Conductive Carbonaceous Substrates via Electrospinning

6.1. Introduction

The application of electroactive polymers often relies on a robust conductive substrate. In electrochemical polymerizations, an inert and conductive material serves as a working electrode, which also plays the role of an initiator and a polymer deposition substrate. Carbonaceous materials have the advantages of high strength to weight ratio, high modulus, chemical resistance, excellent electrical conductivity and durability. Among the various studied carbon materials, carbon fibers have a continuous fibrous structure and can be easily and inexpensively fabricated. In various applications, carbon fibers can not only serve as a conductive framework by facilitating electronic charge transport, but also provide reinforcements by enhancing strain tolerance and structural integrity. The excellent conductivity and chemical stability in most solution conditions render carbon fibers as an ideal supporting substrate for electroactive polymers.

Commercially available carbon microfiber papers were commonly used due to its low cost, good mechanical strength and excellent conductivity. Those carbon microfibers have diameters of 10 μm. When coated with nanoscale polymeric materials, carbon microfibers-containing composite creates a hierarchical architecture. However, due to their large diameters, commercial carbon fibers have small surface areas. Nanostructured materials offer short diffusion pathways to ionic species and high polymer/electrolyte interfacial areas, both of which are crucial properties for electrochemical applications. At a nanoscale, carbon nanofibers attracted special attentions due to their high surface area and tunable electronic structures and surface chemistry. We therefore

turned to carbon nanofibers to further advance the conductive substrates for electroactive polymer composites.

Carbon nanofiber mats can be easily and cost-efficiently fabricated via electrospinning followed by thermal treatments. Electrospinning relies on using a high potential to generate electrostatic repulsions within a polymer blend. A charged polymer jet ejects from the Taylor cone, when the repulsion overcomes the surface tension of the polymer blend, and eventually turns into a polymer fiber as solvent evaporates in the process. Polyacrylonitrile (PAN) is often used as it has a high carbon yield and can convert to carbon fibers with excellent mechanical properties.[144] Thermal treatments, including a stabilization and a carbonization process, subsequently converts polymer fibers into carbonaceous fibers.[29b, 145]

Mao et al. electrospun PAN fibers directly onto a carbon microfiber substrate followed by a thermal treatment to obtain a carbon nanofibers/microfiber composite. In this method, the thickness of the nanofiber mat was controlled by the electrospinning deposition time. As a result, to control the amount of CNFs used, it required modifications to be made at the electrospinning step. Although this method allowed large amount of nanofibers to be densely packed and adhered onto the microfiber substrate, the substrate-supported two-layer architecture lacked a more integrated structural support for the top-layer nanofiber mat to sustain harsh conditions, and therefore calls for a more robust substrate system for applications involving contacting with a flow-through gas or liquid phase.

Here, we developed a simple post-carbonization dip-coating process to fabricate CNF/CMF composites with a well-integrated fibrous structure. This composite demonstrated a comparable mat conductivity to the pristine microfiber substrate and an improved structural

integrity compared to the direct-spun method. The successful construction of the composite rendered it as a robust and versatile substrate for nanostructured electroactive polymers.

6.2. Results and Discussion

Electrospinning technique was used to fabricate PAN polymer electrospun nanofiber mats. The PAN nanofiber mat is non-woven and consists of smooth and continuous nanofibers with diameters of 300-500 nm (**Figure 6-1a**). Upon stabilization in air and subsequent carbonization in nitrogen, PAN fibers were converted into carbon nanofibers. The continuous fibrous structure was maintained after the thermal treatments (**Figure 6-1b**). Under high magnification, the CNFs exhibited a relatively rough surface (**Figure 6-1c**).

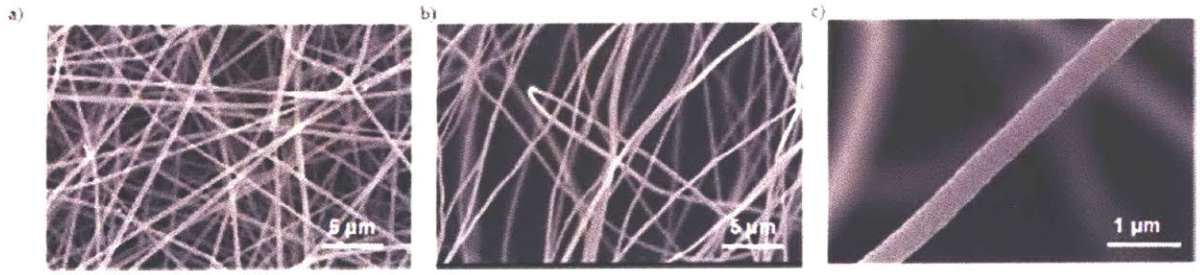

Figure 6-1. (a) SEM images indicate that electrospun PAN nanofiber mat consists of smooth and continuous fibers with diameters of 300-500 nm. (b) Carbonized electrospun fibers maintain their continuous fibrous structure. (c) The electropun CFNs show surface roughness under high magnifications.

As a comparison, direct-spun, dip-coated and drop-casted composites were fabricated with commercial carbon microfiber papers. The surface morphologies of the carbon fiber composites were observed using SEM. SEM images show CNFs in the direct-spun composites exhibit as a separated layer supporting on the CMF substrate (**Figure 6-2a, b**). The CNF layer has cracks and exhibits as small patches. This morphology was likely due to the shrinkage of electrospun fibers

during carbonization, resulting in the incomplete and non-uniform coating of CNFs on the CMF substrate.[146] In the composites prepared by dip-coating and drop-casting, CNFs fill the interstices of the CMF scaffold (**Figure 6-2c, d, e**). As a result, the composite consists of fully integrated CNFs and CMFs without any separate layers. Under high magnifications, ECNFs exhibit a shortened length, likely due to the grinding process in sample preparations (**Figure 6-2f**).

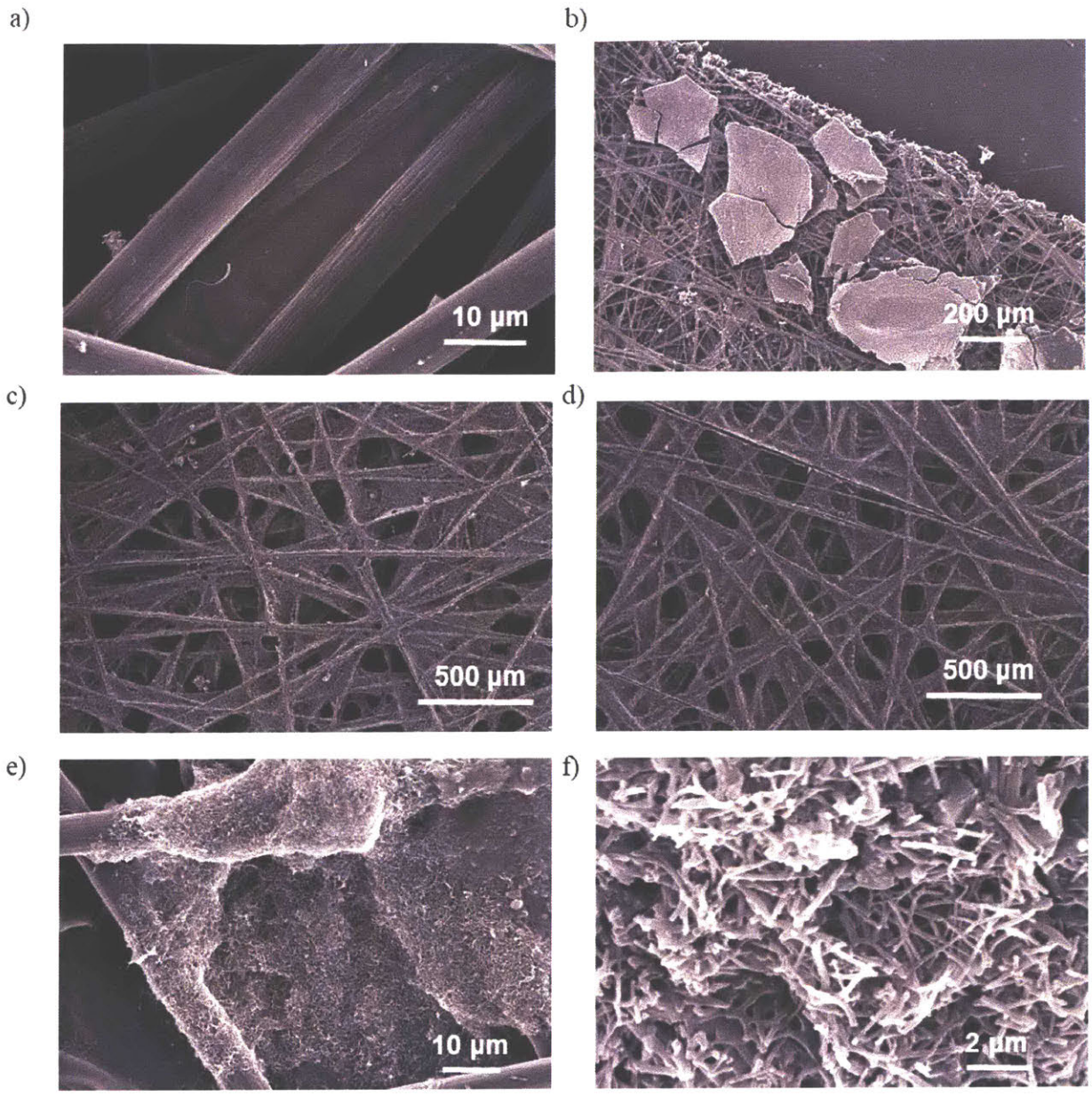

Figure 6-2. (a) SEM images of CMF substrate show the microfibers have diameters of ~ 8 µm. (b) The direct-spun composite exhibits as a cracked CNF mat supported by a microfiber substrate. SEM images show that both (c) dip-coated composite and (d) drop-casted composite have a well-integrated structure where the CMFs are embedded within CNFs. SEM images of dip-coated

composite at higher magnification show that (e) ECNFs are located in the interstices of CMFs, and (f) the ECNFs have a short length likely due to the grinding process during sample preparations.

Fourier Transform Infrared Spectroscopy (FTIR) spectra of ECNFs and two types of commercial CMFs were compared (**Figure 6-3a**). All three fibers exhibit a wide band around 3500 cm^{-1}, corresponding to the hydroxyl groups likely caused by the physically adsorbed water.[147] The weak peaks around 3000 cm^{-1} are due to the C-H bond stretching in the CH_2 groups at carbon edge sites.[147b, 147c] The stretching and bending vibration of C=C in graphene backbones result in bands at 1600 and 1200.[147c] The similarity in FTIR spectra of the carbon fibers confirmed that no new functional groups were introduced into the nanocomposite.

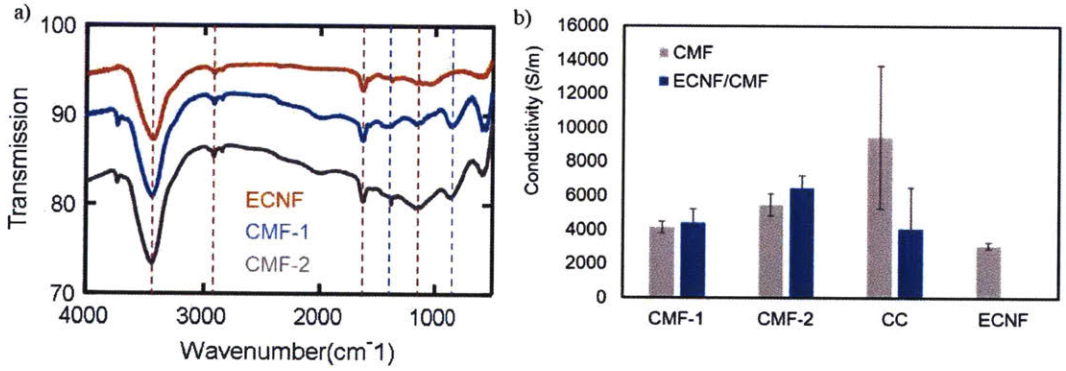

Figure 6-3. (a) The similar FTIR spectra of ECNFs and CMFs indicate that the functional groups present at the carbon fiber surfaces are the same. (b) The conductivity values determined by a 4-point probe method show the effect of ECNFs on the conductivity of the composites.

To serve as a polymer deposition substrate, the excellent conductivity of the CNF/CMF composite is crucial. A 4-probe method was used to evaluate the conductivities of free-standing electrospun CNFs, along with the CNF/CMF composites that were fabricated with two different

types of commercial carbon microfiber paper and one type of carbon cloth. Free-standing ECNFs were found to have a comparable conductivity to that of commercial carbon papers (**Figure 6-3b**). It was found that the coating of ECNFs improved the conductivity of both carbon paper substrates slightly, likely due to the increased contact points between carbon fibers when carbon nanofibers were introduced. The measurement of the carbon cloth shows significant inconsistency among different measurements. Because the carbon cloth is a woven fabric, the sliding motion between the fibers gives this fabric a flexible nature. Consequently, the compressing and sliding between fibers likely resulted in the large variation among different measurements.

As the pPPy/CMF composite was previous demonstrated to exhibit excellent adsorption performance towards aldehydes, the use of CNF/CMF as a substrate in functionalized polymeric composites is of great interest in the development of material systems for adsorbing target pollutants in gas and liquid phase separations. For the composite to be applied in an integrated separation system where a flow-through configuration is often used, the pressure drop across the substrate is an important performance parameter. The pressure drop across a fibrous mat has been shown to increase with the decrease of fiber diameters.[148] This phenomenon is due to the high surface area-to-volume ratio of nanofibers and can pose serious limitations in applying nanoscale materials in such applications.[27b] As nanofibers were introduced into the composites, the pressure drop across the CNF/CMF composites is of interests in evaluating their performance. We measured the pressure drops cross various substrates and composites at a face velocity of 45 cm s^{-1} in air at room temperature (**Table 6-1**). It was found that the introduction of electrospun CNFs only resulted in a small increase in the pressure drop for one carbon microfiber paper substrate. In the case of carbon cloth and CMF-2, the pressure drop remained the same upon coating of CNFs. This is likely because only a small amount of ECNFs were coated onto the CMF substrate using the

dip-coating method. The CMFs were embedded within a thin web of CNFs instead of underneath a thick dense mat of nanofibers, imposing negligible effect on the flow of air through the composite.

Table 6-1. The pressure drop values across various substrates and composites were measured at a face velocity of 45 cm s^{-1} at room temperature.

Substrate	ΔP (kPa)	Substrate	ΔP (kPa)
CMF-1	0.65±0.02	CNF/CMF-1	0.74±0.02
CMF-2	0.08+±0.02	CNF/CMF-2	0.09±0.02
CC	0.02±0.01	CNF/CC	0.01±0.01

As the carbon fiber composite can be used as the conductive substrate for electrochemical polymerization, the electrochemical active surface area (ESA) is an important characteristic of the CNF/CMF substrate. ESA can be determined by measuring the CV response of $Fe(CN)_6^{3-}$ /$Fe(CN)_6^{4-}$ at a range of scan rates.[145a] Based on the Randles-Sevcik equation:

$$i_p = (2.687\times10^5)n^{3/2}v^{1/2}D^{1/2}AC, \quad (6.1)$$

the ESA can be determined from the slope obtained by fitting the peak current to the square root of scan rate. Here, C is the bulk concentration of $Fe(CN)_6^{3-}$ (10 mM). D is the diffusion coefficient of $Fe(CN)_6^{3-}$/$Fe(CN)_6^{4-}$ (5.7×10^{-6} cm^2/s).[130] v is the scan rate of the cyclic voltammetry. n is the number of electrons transferred (n=1). A is the ESA of the substrate (cm^2). **Figure 6-4** shows an example of the CV measurements and linear fitting for the carbon fibers. The specific ESA of CMF was determined to be 0.11 m^2 g^{-1}, which is lower than its theoretical specific surface area determined by its geometry and the true density of carbon (0.25 m^2 g^{-1}).[149] This is likely caused by

the inaccessibility of the carbon fibers further inside the carbon fiber paper by the redox probe. This discrepancy is more obvious for CNFs, where the determined specific ESA, 1.4 $m^2 g^{-1}$, is much smaller than that of the theoretical specific ESA, 5 $m^2 g^{-1}$. This was likely caused by the densely packed nature of the freestanding CNF mat. When comparing the composite prepared with different concentrations of CNFs and different dipping time, it was found that dipping time has negligible effect on the ESA of the composite, whereas a higher concentration of CNF in the suspension results in a higher ESA for the composite (**Table 6-2**). The effective mass of CNFs loaded onto the CNF/CMF composite was estimated by assuming the specific ESAs of CNF and CMF remain the same before and after forming a composite. It was found that the effective mass loading of CNFs is very small (~ 1 mg), supporting the hypothesis that the low pressure drop measured is due to the small amount of CNFs coated onto the electrode.

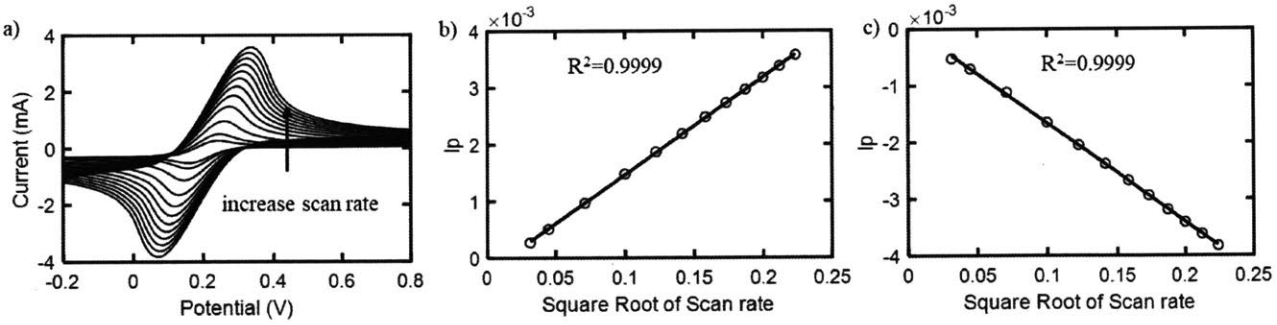

Figure 6-4. (a) CV measurements of CMF substrate with $Fe(CN)_6^{3-}/Fe(CN)_6^{4-}$ as a redox probe. The linear fitting of the peak current for (b) anodic current and (c) catholic current based on Randles-Sevcik equation.

Table 6-2. The ESA of CNF/CMF composited determined by electrochemical methods.

	CMF	CNF	Dip time (s) at 10 mg/mL			CNF conc. (mg mL^{-1}) at 5 s dip time		
			5	10	30	1	5	10
ESA (cm^2)	5.40±0.04	70±1.1	16±0.44	17±0.26	16±0.25	10±0.2	15±0.3	16±0.25
Specific ESA ($m^2 g^{-1}$)	0.11	1.4	0.32	0.34	0.32	0.2	0.3	0.32
Effective CNF Mass (mg)	NA	NA	0.98	1.09	0.98	0.38	0.87	0.98

6.3. Conclusion

In this section of the thesis, carbon nanofibers were fabricated via electrospinning followed by a thermal treatment process. A dip-coating method was developed to incorporate submicron ECNFs into a CMF substrate. With the support of CMFs, the developed ECNF/CMF composite exhibits excellent structural integrity. This well integrated structure ensured good electrical conductivity throughout the entire composite. Despite the smaller diameters of ECNFs, the unique structure of embedding CMFs within a thin web of CNFs avoided posing a high pressure drop cross the composite, rendering the composite as a suitable candidate for flow-through separation systems.

6.4. Experimental Section

6.4.1. Materials

Polyacrylonitrile (PAN) (MW=150 000) and chloroform were purchased from Millipore Sigma and used as received. The carbon microfiber substrates and the carbon cloths were obtained from Electrochem Inc.

6.4.2. Fabrication of Electrospun Carbon Fibers

Electrospun polymer fibers were first fabricated using a PAN solution. 10 wt% PAN precursor solution was prepared by placing the PAN and DMF mixture in a water bath at 80 °C with vigorous stirring. A parallel-plate electrospinning setup with a 30 cm plate-to-place distance was used. During electrospinning, an applied potential of 30 kV and a flow rate of 0.02 mL min^{-1} was chosen. The electrospun fibers were collected on a grounded metal plate. The electrospun PAN fibers were then converted to carbon fibers via a two-step process involving stabilization and carbonization as described by Mao *et al.*[145a] The thermal treatment processes were performed in a tube furnace (MTI, GSL-1800S60).

The electrospun carbon nanofibers were incorporated into a carbon microfiber substrate via three different fabrication methods. In the first method developed by Mao *et al.*,[145b] PAN nanofibers were directly electrspun onto the carbon microfiber substrate. The PAN nanofiber/CMF composite was then sandwiched between molybdenum plates to maintain the contact between the nanofibers and the microfiber substrate during the thermal treatment. The formed CNF/CMF composite was denoted as the direct-spun composite. In the second method, electrospun PAN fibers were first converted to CNFs via the thermal treatment. The CNFs were then ground into a powder form. A CNFs/chloroform suspension of 10 mg mL^{-1} was prepared by sonication. A

specific aliquot of suspension was drop-casted on to the CMF substrate, followed by air drying. Samples prepared via this method were denoted as drop-casted composites. A third method involved dip-coating the CMF substrate in the same CNF/chloroform suspension. The carbon microfiber paper was slowly submerged into the suspension and remained in the suspension for 5 seconds. The dip-coated CMF substrate was then air dried in a fume hood, resulting the composite denoted as the dip-coated composite.

6.4.3. Material Characterizations

The morphologies of the CNF/CMF composites were observed by SEM (JEOL 6010LA). A four-point probe method was used to measure the conductivity of the carbon fiber samples. The conductivity of each sample was measured in different directions for multiple times. Sheet resistance of the carbon fiber composites were evaluated using Signatone S-302-4 with a Keithley SCS-4200 current source. The pressure drop values across the CNF/CMF composites were measured by flowing air at 45 cm s^{-1} through a circular-shaped composite at room temperature. All electrochemical characterization experiments were performed in a three-electrode electrochemical cell with a VersaSTAT 3 potentiostat (Princeton Applied Research).

Bibliography

1. (a) Kim, J.; Lee, J.; You, J.; Park, M.-S.; Hossain, M. S. A.; Yamauchi, Y.; Kim, J. H., Conductive polymers for next-generation energy storage systems: recent progress and new functions. *Materials Horizons* **2016,** *3* (6), 517-535; (b) Muench, S.; Wild, A.; Friebe, C.; Häupler, B.; Janoschka, T.; Schubert, U. S., Polymer-Based Organic Batteries. *Chemical Reviews* **2016,** *116* (16), 9438-9484; (c) Gracia, R.; Mecerreyes, D., Polymers with redox properties: materials for batteries, biosensors and more. *Polymer Chemistry* **2013,** *4* (7), 2206-2214.

2. (a) Janata, J.; Josowicz, M., Conducting polymers in electronic chemical sensors. *Nature Materials* **2003,** *2*, 19; (b) Pernaut, J.-M.; Reynolds, J. R., Use of Conducting Electroactive Polymers for Drug Delivery and Sensing of Bioactive Molecules. A Redox Chemistry Approach. *The Journal of Physical Chemistry B* **2000,** *104* (17), 4080-4090; (c) Xia, L.; Wei, Z.; Wan, M., Conducting polymer nanostructures and their application in biosensors. *Journal of Colloid and Interface Science* **2010,** *341* (1), 1-11.

3. Chandra, V.; Kim, K. S., Highly selective adsorption of Hg2+ by a polypyrrole-reduced graphene oxide composite. *Chemical Communications* **2011,** *47* (13), 3942-3944.

4. (a) Nagaoka, T.; Fujimoto, M.; Nakao, H.; Kakuno, K.; Yano, J.; Ogura, K., Electrochemical separation of ionic compounds using a conductive stationary phase coated with polyaniline or polypyrrole film, and ion exchange properties of conductive polymers. *Journal of Electroanalytical Chemistry* **1994,** *364* (1), 179-188; (b) Weidlich, C.; Mangold, K. M.; Jüttner, K., Continuous ion exchange process based on polypyrrole as an electrochemically switchable ion exchanger. *Electrochim Acta* **2005,** *50* (25), 5247-5254; (c) Wu, J.; Mullett, W. M.; Pawliszyn, J., Electrochemically Controlled Solid-Phase Microextraction Based on Conductive Polypyrrole Films. *Analytical Chemistry* **2002,** *74* (18), 4855-4859.

5. Akhoury, A.; Bromberg, L.; Hatton, T. A., Redox-Responsive Gels with Tunable Hydrophobicity for Controlled Solubilization and Release of Organics. *ACS Applied Materials & Interfaces* **2011,** *3* (4), 1167-1174.

6. Su, X.; Hatton, T. A., Electrosorption at functional interfaces: from molecular-level interactions to electrochemical cell design. *Physical Chemistry Chemical Physics* **2017,** *19* (35), 23570-23584.

7. Su, X.; Hübner, J.; Kauke, M. J.; Dalbosco, L.; Thomas, J.; Gonzalez, C. C.; Zhu, E.; Franzreb, M.; Jamison, T. F.; Hatton, T. A., Redox Interfaces for Electrochemically Controlled Protein–Surface Interactions: Bioseparations and Heterogeneous Enzyme Catalysis. *Chem Mater* **2017,** *29* (13), 5702-5712.

8. Shi, Y.; Peng, L.; Ding, Y.; Zhao, Y.; Yu, G., Nanostructured conductive polymers for advanced energy storage. *Chem Soc Rev* **2015,** *44* (19), 6684-6696.

9. Li, C.; Bai, H.; Shi, G., Conducting polymer nanomaterials: electrosynthesis and applications. *Chem Soc Rev* **2009,** *38* (8), 2397-2409.

10. Otero, T. F.; Sansieña, J. M., Soft and Wet Conducting Polymers for Artificial Muscles. *Adv Mater* **1998,** *10* (6), 491-494.

11. (a) Otero, T. F., Soft, wet, and reactive polymers. Sensing artificial muscles and conformational energy. *Journal of Materials Chemistry* **2009,** *19* (6), 681-689; (b) Smela, E., Conjugated Polymer Actuators for Biomedical Applications. *Adv Mater* **2003,** *15* (6), 481-494.

12. Sadki, S.; Schottland, P.; Brodie, N.; Sabouraud, G., The mechanisms of pyrrole electropolymerization. *Chem Soc Rev* **2000,** *29* (5), 283-293.

13. Jang, J.; Yoon, H., Formation Mechanism of Conducting Polypyrrole Nanotubes in Reverse Micelle Systems. *Langmuir* **2005,** *21* (24), 11484-11489.

14. (a) Wu, C.-G.; Bein, T., Conducting Polyaniline Filaments in a Mesoporous Channel Host. *Science* **1994,** *264* (5166), 1757-1759; (b) Wang, C.; Wang, Z.; Li, M.; Li, H., Well-aligned polyaniline nano-fibril array membrane and its field emission property. *Chemical Physics Letters* **2001,** *341* (5), 431-434.

15. Misoska, V.; Price, W.; Ralph, S.; Wallace, G., Electrochemical synthesis of pyrrole through a polystyrene opal matrix. *Synthetic Met* **2001,** *121* (1), 1501-1502.

16. Martin, C. R., Membrane-Based Synthesis of Nanomaterials. *Chem Mater* **1996,** *8* (8), 1739-1746.

17. Chen, J.; Chao, D.; Lu, X.; Zhang, W.; Manohar, S. K., General Synthesis of Two-Dimensional Patterned Conducting Polymer-Nanobowl Sheet via Chemical Polymerization. *Macromol Rapid Comm* **2006,** *27* (10), 771-775.

18. Zhang, X.; Zhang, J.; Song, W.; Liu, Z., Controllable Synthesis of Conducting Polypyrrole Nanostructures. *The Journal of Physical Chemistry B* **2006,** *110* (3), 1158-1165.

19. Huang, K.; Wan, M., Self-Assembled Polyaniline Nanostructures with Photoisomerization Function. *Chem Mater* **2002,** *14* (8), 3486-3492.

20. (a) Yan, Y.; Yu, Z.; Huang, Y. W.; Yuan, W. X.; Wei, Z. X., Helical Polyaniline Nanofibers Induced by Chiral Dopants by a Polymerization Process. *Adv Mater* **2007,** *19* (20), 3353-3357; (b) Li, W.; Wang, H.-L., Oligomer-Assisted Synthesis of Chiral Polyaniline Nanofibers. *Journal of the American Chemical Society* **2004,** *126* (8), 2278-2279.

21. Huang, J.; Virji, S.; Weiller, B. H.; Kaner, R. B., Polyaniline Nanofibers: Facile Synthesis and Chemical Sensors. *Journal of the American Chemical Society* **2003,** *125* (2), 314-315.

22. (a) Zhang, X.; Goux, W. J.; Manohar, S. K., Synthesis of Polyaniline Nanofibers by "Nanofiber Seeding". *Journal of the American Chemical Society* **2004,** *126* (14), 4502-4503; (b) Zhang, X.; Manohar, S. K., Bulk Synthesis of Polypyrrole Nanofibers by a Seeding Approach. *Journal of the American Chemical Society* **2004,** *126* (40), 12714-12715; (c) Zhang, X.; Manohar, S. K., Narrow Pore-Diameter Polypyrrole Nanotubes. *Journal of the American Chemical Society* **2005,** *127* (41), 14156-14157; (d) Pan, L. J.; Pu, L.; Shi, Y.; Song, S. Y.; Xu, Z.; Zhang, R.; Zheng, Y. D., Synthesis of Polyaniline Nanotubes with a Reactive Template of Manganese Oxide. *Adv Mater* **2007,** *19* (3), 461-464.

23. He, H. X.; Li, C. Z.; Tao, N. J., Conductance of polymer nanowires fabricated by a combined electrodeposition and mechanical break junction method. *Applied Physics Letters* **2001,** *78* (6), 811-813.

24. Zhang, Y.; Rutledge, G. C., Electrical Conductivity of Electrospun Polyaniline and Polyaniline-Blend Fibers and Mats. *Macromolecules* **2012,** *45* (10), 4238-4246.

25. Rutledge, G. C.; Fridrikh, S. V., Formation of fibers by electrospinning. *Advanced Drug Delivery Reviews* **2007,** *59* (14), 1384-1391.

26. (a) Bhardwaj, N.; Kundu, S. C., Electrospinning: A fascinating fiber fabrication technique. *Biotechnology Advances* **2010,** *28* (3), 325-347; (b) Lu, Y.; Huang, J.; Yu, G.; Cardenas, R.; Wei, S.; Wujcik, E. K.; Guo, Z., Coaxial electrospun fibers: applications in drug delivery and tissue engineering. *Wiley Interdisciplinary Reviews: Nanomedicine and Nanobiotechnology* **2016,** *8* (5), 654-677.

27. (a) Scholten, E.; Bromberg, L.; Rutledge, G. C.; Hatton, T. A., Electrospun Polyurethane Fibers for Absorption of Volatile Organic Compounds from Air. *ACS Applied Materials & Interfaces* **2011,** *3* (10), 3902-3909; (b) Chattopadhyay, S.; Hatton, T. A.; Rutledge, G. C., Aerosol filtration using electrospun cellulose acetate fibers. *Journal of Materials Science* **2016,** *51* (1), 204-217.

28. Sridhar, R.; Lakshminarayanan, R.; Madhaiyan, K.; Amutha Barathi, V.; Lim, K. H. C.; Ramakrishna, S., Electrosprayed nanoparticles and electrospun nanofibers based on natural materials: applications in tissue regeneration, drug delivery and pharmaceuticals. *Chem Soc Rev* **2015,** *44* (3), 790-814.

29. (a) Mao, X.; Yang, X.; Wu, J.; Tian, W.; Rutledge, G. C.; Hatton, T. A., Microwave-Assisted Oxidation of Electrospun Turbostratic Carbon Nanofibers for Tailoring Energy Storage Capabilities. *Chem Mater* **2015,** *27* (13), 4574-4585; (b) Yang, Y.; Centrone, A.; Chen, L.; Simeon, F.; Alan Hatton, T.; Rutledge, G. C., Highly porous electrospun polyvinylidene fluoride (PVDF)-based carbon fiber. *Carbon* **2011,** *49* (11), 3395-3403; (c) Mao, X.; Tian, W.; Hatton, T. A.; Rutledge, G. C., Advances in electrospun carbon fiber-based electrochemical sensing platforms for bioanalytical applications. *Analytical and Bioanalytical Chemistry* **2016,** *408* (5), 1307-1326.

30. (a) Arico, A. S.; Bruce, P.; Scrosati, B.; Tarascon, J. M.; Van Schalkwijk, W., Nanostructured materials for advanced energy conversion and storage devices. *Nat Mater* **2005,** *4* (5), 366-377; (b) Simon, P.; Gogotsi, Y., Materials for electrochemical capacitors. *Nat Mater* **2008,** *7* (11), 845-854.

31. (a) *Modern Aspects of Electrochemistry No. 44*. Springer New York: 2009; Vol. 44; (b) Inzelt, G., *Conducting Polymers*. 2 ed.; Springer Berlin Heidelberg: 2012; p 310; (c) *Advances in Chemical Physics: Polymeric Systems*. John Wiley & Sons, Inc: 1996; Vol. 94.

32. (a) Savéant, J. M., Electron hopping between fixed sites: Equivalent diffusion and migration laws. *Journal of Electroanalytical Chemistry and Interfacial Electrochemistry* **1986,** *201* (1), 211-213; (b) Laviron, E., A multilayer model for the study of space distributed redox modified electrodes: Part I. Description and discussion of the model. *Journal of Electroanalytical Chemistry and Interfacial Electrochemistry* **1980,** *112* (1), 1-9; (c) Vorotyntsev, M. A.; Vasilyeva, S. V., Metallocene-containing conjugated polymers. *Advances in Colloid and Interface Science* **2008,** *139* (1–2), 97-149; (d) Dalton, E. F.; Surridge, N. A.; Jernigan, J. C.; Wilbourn, K. O.; Facci, J. S.; Murray, R. W., Charge transport in electroactive polymers consisting of fixed molecular redox sites. *Chemical Physics* **1990,** *141* (1), 143-157.

33. *Applications of Electroactive Polymers*. Chapman & Hall: 1993; p 354.

34. Iwakura, C.; Kawai, T.; Nojima, M.; Yoneyama, H., A New Electrode-Active Material for Polymer Batteries: Polyvinylferrocene. *Journal of The Electrochemical Society* **1987,** *134* (4), 791-795.

35. Mao, X.; Simeon, F.; Achilleos, D. S.; Rutledge, G. C.; Hatton, T. A., Metallocene/carbon hybrids prepared by a solution process for supercapacitor applications. *Journal of Materials Chemistry A* **2013,** *1* (42), 13120-13127.

36. Janata, J.; Josowicz, M., Conducting polymers in electronic chemical sensors. *Nat Mater* **2003,** *2* (1), 19-24.

37. (a) William H. Smyrl, M. L., Electrical and electrochemical properties of electronically conducting polymers. In *Applications of Electroactive Polymers*, Scrosati, B., Ed. Springer Netherlands: 1993; pp pp 29-74; (b) Snook, G. A.; Kao, P.; Best, A. S., Conducting-polymer-based supercapacitor devices and electrodes. *J Power Sources* **2011,** *196* (1), 1-12.

38. (a) Bubnova, O.; Khan, Z. U.; Wang, H.; Braun, S.; Evans, D. R.; Fabretto, M.; Hojati-Talemi, P.; Dagnelund, D.; Arlin, J.-B.; Geerts, Y. H.; Desbief, S.; Breiby, D. W.; Andreasen, J. W.; Lazzaroni, R.; Chen, W. M.; Zozoulenko, I.; Fahlman, M.; Murphy, P. J.; Berggren, M.; Crispin, X., Semi-metallic polymers. *Nat Mater* **2014,** *13* (2), 190-194; (b) Zhou, M.; Qian, J.; Ai, X.; Yang, H., Redox-Active Fe(CN)64−-Doped Conducting Polymers with Greatly Enhanced Capacity as Cathode Materials for Li-Ion Batteries. *Adv. Mater.* **2011,** *23* (42), 4913-4917.

39. (a) Northcutt, R. G.; Sundaresan, V. B., Phospholipid vesicles as soft templates for electropolymerization of nanostructured polypyrrole membranes with long range order. *Journal of Materials Chemistry A* **2014,** *2* (30), 11784-11791; (b) Kim, M. S.; Moon, J. H.; Yoo, P. J.; Park, J. H., Hollow Polypyrrole Films: Applications for Energy Storage Devices. *Journal of The Electrochemical Society* **2012,** *159* (7), A1052-A1056; (c) Kowalski, D.; Schmuki, P., Polypyrrole self-organized nanopore arrays formed by controlled electropolymerization in TiO2 nanotube template. *Chem. Commun.* **2010,** *46* (45), 8585-8587; (d) Bartlett, P. N.; Birkin, P. R.; Ghanem, M. A.; Toh, C. S., Electrochemical syntheses of highly ordered macroporous conducting polymers grown around self-assembled colloidal templates. *J Mater Chem* **2001,** *11* (3), 849-853; (e) Kim, J.-Y.; Kim, K. H.; Kim, K. B., Fabrication and electrochemical properties of carbon nanotube/polypyrrole composite film electrodes with controlled pore size. *J Power Sources* **2008,** *176* (1), 396-402; (f) Lee, J. I.; Cho, S. H.; Park, S. M.; Kim, J. K.; Kim, J. K.; Yu, J. W.; Kim, Y. C.; Russell, T. P., Highly aligned ultrahigh density arrays of conducting polymer nanorods using block copolymer templates. *Nano Lett* **2008,** *8* (8), 2315-2320.

40. (a) Yan, Y.; Zhang, J. Y.; Qiao, Y. L.; Ganewatta, M.; Tang, C. B., Ruthenocene-Containing Homopolymers and Block Copolymers via ATRP and RAFT Polymerization. *Macromolecules* **2013,** *46* (22), 8816-8823; (b) Hardy, C. G.; Zhang, J. Y.; Yan, Y.; Ren, L. X.; Tang, C. B., Metallopolymers with transition metals in the side-chain by living and controlled polymerization techniques. *Prog Polym Sci* **2014,** *39* (10), 1742-1796; (c) G. Pickup, P., Conjugated metallopolymers. Redox polymers with interacting metal based redox sites. *J Mater Chem* **1999,** *9* (8), 1641-1653.

41. Dong, B.; Zhong, D. Y.; Chi, L. F.; Fuchs, H., Patterning of Conducting Polymers Based on a Random Copolymer Strategy: Toward the Facile Fabrication of Nanosensors Exclusively Based on Polymers. *Adv. Mater.* **2005,** *17* (22), 2736-2741.

42. Mao, X.; Tian, W.; Wu, J.; Rutledge, G. C.; Hatton, T. A., Electrochemically Responsive Heterogeneous Catalysis for Controlling Reaction Kinetics. *Journal of the American Chemical Society* **2015**.

43. Kaiser, A. B., Systematic Conductivity Behavior in Conducting Polymers: Effects of Heterogeneous Disorder. *Adv. Mater.* **2001,** *13* (12-13), 927-941.

44. Kruk, M.; Jaroniec, M., Gas adsorption characterization of ordered organic-inorganic nanocomposite materials. *Chem Mater* **2001,** *13* (10), 3169-3183.

45. (a) Dubal, D. P.; Lee, S. H.; Kim, J. G.; Kim, W. B.; Lokhande, C. D., Porous polypyrrole clusters prepared by electropolymerization for a high performance supercapacitor. *J. Mater. Chem.* **2012,** *22* (7), 3044-3052; (b) Cui, Y. M.; Wen, Z. Y.; Liang, X.; Lu, Y.; Jin, J.; Wu, M. F.; Wu, X. W., A tubular polypyrrole based air electrode with improved O-2 diffusivity for Li-O-2 batteries. *Energy Environ. Sci.* **2012,** *5* (7), 7893-7897; (c) Chang, L. Y.; Li, C. T.; Li, Y. Y.; Lee, C. P.; Yeh, M. H.; Ho, K. C.; Lin, J. J., Morphological Influence of Polypyrrole Nanoparticles on the Performance of Dye-Sensitized Solar Cells. *Electrochim. Acta* **2015,** *155*, 263-271; (d) Shinde, S. S.; Gund, G. S.; Dubal, D. P.; Jambure, S. B.; Lokhande, C. D., Morphological modulation of polypyrrole thin films through oxidizing agents and their concurrent effect on supercapacitor performance. *Electrochim. Acta* **2014,** *119*, 1-10.

46. Neoh, K. G.; Kang, E. T.; Tan, K. L., Limitations of the X-ray Photoelectron Spectroscopy Technique in the Study of Electroactive Polymers. *The Journal of Physical Chemistry B* **1997,** *101* (5), 726-731.

47. (a) Woodbridge, C. M.; Pugmire, D. L.; Johnson, R. C.; Boag, N. M.; Langell, M. A., HREELS and XPS Studies of Ferrocene on Ag(100)†. *The Journal of Physical Chemistry B* **2000,** *104* (14), 3085-3093; (b) Gassman, P. G.; Macomber, D. W.; Hershberger, J. W., Evaluation by ESCA of the electronic effect of methyl substitution on the cyclopentadienyl ligand. A study of titanocenes, zirconocenes, hafnocenes, and ferrocenes. *Organometallics* **1983,** *2* (10), 1470-1472; (c) Barber, M.; Connor, J. A.; Derrick, L. M. R.; Hall, M. B.; Hillier, I. H., High energy photoelectron spectroscopy of transition metal complexes. Part 2.-Metallocenes. *Journal of the Chemical Society, Faraday Transactions 2: Molecular and Chemical Physics* **1973,** *69* (0), 559-562.

48. Yang, C.; Liu, P.; Wang, T., Well-Defined Core–Shell Carbon Black/Polypyrrole Nanocomposites for Electrochemical Energy Storage. *ACS Applied Materials & Interfaces* **2011,** *3* (4), 1109-1114.

49. Qu, W.-H.; Xu, Y.-Y.; Lu, A.-H.; Zhang, X.-Q.; Li, W.-C., Converting biowaste corncob residue into high value added porous carbon for supercapacitor electrodes. *Bioresource Technology* **2015,** *189* (0), 285-291.

50. Zhu, D. Z.; Wang, Y. W.; Gan, L. H.; Liu, M. X.; Cheng, K.; Zhao, Y. H.; Deng, X. X.; Sun, D. M., Nitrogen-containing carbon microspheres for supercapacitor electrodes. *Electrochim Acta* **2015,** *158*, 166-174.

51. (a) Li, H. L.; Jiang, L. X.; Cheng, Q. L.; He, Y.; Pavlinek, V.; Saha, P.; Li, C. Z., MnO2 nanoflakes/hierarchical porous carbon nanocomposites for high-performance supercapacitor electrodes. *Electrochim Acta* **2015,** *164*, 252-259; (b) Balasubramanian, S.; Kamatchi Kamaraj, P., Fabrication of Natural Polymer Assisted Mesoporous Co3O4/Carbon Composites for

Supercapacitors. *Electrochim Acta* **2015,** *168* (0), 50-58; (c) Kim, C. H.; Kim, B. H., Zinc oxide/activated carbon nanofiber composites for high-performance supercapacitor electrodes. *J Power Sources* **2015,** *274*, 512-520.

52. (a) Khomenko, V.; Frackowiak, E.; Béguin, F., Determination of the specific capacitance of conducting polymer/nanotubes composite electrodes using different cell configurations. *Electrochim Acta* **2005,** *50* (12), 2499-2506; (b) Stoller, M. D.; Ruoff, R. S., Best practice methods for determining an electrode material's performance for ultracapacitors. *Energ Environ Sci* **2010,** *3* (9), 1294-1301; (c) Stoller, M. D.; Park, S.; Zhu, Y.; An, J.; Ruoff, R. S., Graphene-Based Ultracapacitors. *Nano Lett* **2008,** *8* (10), 3498-3502.

53. Jiang, W. C.; Yu, D. S.; Zhang, Q.; Goh, K. L.; Wei, L.; Yong, Y. L.; Jiang, R. R.; Wei, J.; Chen, Y., Ternary Hybrids of Amorphous Nickel Hydroxide-Carbon Nanotube-Conducting Polymer for Supercapacitors with High Energy Density, Excellent Rate Capability, and Long Cycle Life. *Adv Funct Mater* **2015,** *25* (7), 1063-1073.

54. Dunn, B.; Kamath, H.; Tarascon, J. M., Electrical Energy Storage for the Grid: A Battery of Choices. *Science* **2011,** *334* (6058), 928-935.

55. Zhao, J.; Xu, S.; Tschulik, K.; Compton, R. G.; Wei, M.; O'Hare, D.; Evans, D. G.; Duan, X., Molecular-Scale Hybridization of Clay Monolayers and Conducting Polymer for Thin-Film Supercapacitors. *Adv Funct Mater* **2015**, 1616-3028.

56. (a) Peng, Y. J.; Wu, T. H.; Hsu, C. T.; Li, S. M.; Chen, M. G.; Hu, C. C., Electrochemical characteristics of the reduced graphene oxide/carbon nanotube/polypyrrole composites for aqueous asymmetric supercapacitors. *J Power Sources* **2014,** *272*, 970-978; (b) Chee, W. K.; Lim, H. N.; Harrison, I.; Chong, K. F.; Zainal, Z.; Ng, C. H.; Huang, N. M., Performance of Flexible and Binderless Polypyrrole/Graphene Oxide/Zinc Oxide Supercapacitor Electrode in a Symmetrical Two-Electrode Configuration. *Electrochim Acta* **2015,** *157*, 88-94; (c) Zhu, Y. L.; Shi, K. Y.; Zhitomirsky, I., Polypyrrole coated carbon nanotubes for supercapacitor devices with enhanced electrochemical performance. *J Power Sources* **2014,** *268*, 233-239; (d) Li, P. X.; Yang, Y. B.; Shi, E. Z.; Shen, Q. C.; Shang, Y. Y.; Wu, S. T.; Wei, J. Q.; Wang, K. L.; Zhu, H. W.; Yuan, Q.; Cao, A. Y.; Wu, D. H., Core-Double-Shell, Carbon Nanotube@Polypyrrole@MnO2 Sponge as Freestanding, Compressible Supercapacitor Electrode. *Acs Applied Materials & Interfaces* **2014,** *6* (7), 5228-5234; (e) Feng, H. X.; Wang, B.; Tan, L.; Chen, N. L.; Wang, N. X.; Chen, B. Y., Polypyrrole/hexadecylpyridinium chloride-modified graphite oxide composites: Fabrication, characterization, and application in supercapacitors. *J Power Sources* **2014,** *246*, 621-628; (f) Chen, G. F.; Su, Y. Z.; Kuang, P. Y.; Liu, Z. Q.; Chen, D. Y.; Wu, X.; Li, N.; Qiao, S. Z., Polypyrrole Shell@3D-Ni Metal Core Structured Electrodes for High-Performance Supercapacitors. *Chem-Eur J* **2015,** *21* (12), 4614-4621; (g) Cai, X. Y.; Lim, S. H.; Poh, C. K.; Lai, L. F.; Lin, J. Y.; Shen, Z. X., High-performance asymmetric pseudocapacitor cell based on cobalt hydroxide/graphene and polypyrrole/graphene electrodes. *J Power Sources* **2015,** *275*, 298-304; (h) Shao, M.; Li, Z.; Zhang, R.; Ning, F.; Wei, M.; Evans, D. G.; Duan, X., Hierarchical Conducting Polymer@Clay Core–Shell Arrays for Flexible All-Solid-State Supercapacitor Devices. *Small* **2015**, 1613-6829; (i) Chuan Xia, W. C., Xianbin Wang, Mohamed N. Hedhili, Nini Wei, Husam N. Alshareef, Highly Stable Supercapacitors with Conducting Polymer Core-Shell Electrodes for Energy Storage Applications. *Advanced Energy Materials* **2015,** *5* (8), 1614-6840.

57. Liu, T.; Finn, L.; Yu, M.; Wang, H.; Zhai, T.; Lu, X.; Tong, Y.; Li, Y., Polyaniline and Polypyrrole Pseudocapacitor Electrodes with Excellent Cycling Stability. *Nano Lett* **2014,** *14* (5), 2522-2527.

58. (a) Meng, C.; Liu, C.; Chen, L.; Hu, C.; Fan, S., Highly Flexible and All-Solid-State Paperlike Polymer Supercapacitors. *Nano Lett* **2010,** *10* (10), 4025-4031; (b) Frackowiak, E., Carbon materials for supercapacitor application. *Physical Chemistry Chemical Physics* **2007,** *9* (15), 1774-1785; (c) Wang, G.; Zhang, L.; Zhang, J., A review of electrode materials for electrochemical supercapacitors. *Chemical Society Reviews* **2012,** *41* (2), 797-828.

59. (a) Qian, H.-S.; Yu, S.-H.; Luo, L.-B.; Gong, J.-Y.; Fei, L.-F.; Liu, X.-M., Synthesis of Uniform Te@Carbon-Rich Composite Nanocables with Photoluminescence Properties and Carbonaceous Nanofibers by the Hydrothermal Carbonization of Glucose. *Chem Mater* **2006,** *18* (8), 2102-2108; (b) Zhang, L.; Zhang, G.; Wu, H. B.; Yu, L.; Lou, X. W., Hierarchical Tubular Structures Constructed by Carbon-Coated SnO2 Nanoplates for Highly Reversible Lithium Storage. *Adv. Mater.* **2013,** *25* (18), 2589-2593; (c) Titirici, M.-M.; Antonietti, M., Chemistry and materials options of sustainable carbon materials made by hydrothermal carbonization. *Chemical Society Reviews* **2010,** *39* (1), 103-116; (d) Zhang, W.-M.; Hu, J.-S.; Guo, Y.-G.; Zheng, S.-F.; Zhong, L.-S.; Song, W.-G.; Wan, L.-J., Tin-Nanoparticles Encapsulated in Elastic Hollow Carbon Spheres for High-Performance Anode Material in Lithium-Ion Batteries. *Adv. Mater.* **2008,** *20* (6), 1160-1165.

60. Zheng, H.; Zhai, T.; Yu, M.; Xie, S.; Liang, C.; Zhao, W.; Wang, S. C. I.; Zhang, Z.; Lu, X., TiO2@C core-shell nanowires for high-performance and flexible solid-state supercapacitors. *Journal of Materials Chemistry C* **2013,** *1* (2), 225-229.

61. Roe, R.-J., *Methods of X-ray and Neutron Scattering in Polymer Science*. Oxford University Press: 2000.

62. Mao, X. W.; Rutledge, G. C.; Hatton, T. A., Polyvinylferrocene for Noncovalent Dispersion and Redox-Controlled Precipitation of Carbon Nanotubes in Nonaqueous Media. *Langmuir* **2013,** *29* (31), 9626-9634.

63. Simionescu, C. I.; Cianga, I.; Ivanoiu, M.; Airinei, A.; Grigoras, M.; Radu, I., Oxidative polymerization of some monomers with pyrrole moieties—an UV–vis absorption spectroscopy study. *European Polymer Journal* **1999,** *35* (10), 1895-1905.

64. Karachevtsev, V. A.; Plokhotnichenko, A. M.; Karachevtsev, M. V.; Leontiev, V. S., Decrease of carbon nanotube UV light absorption induced by π–π-stacking interaction with nucleotide bases. *Carbon* **2010,** *48* (13), 3682-3691.

65. Salahi, S.; Iashkenari, M. S.; Abbaszadeh, M.; Pousti, M.; Ghorbani, M., Synthesis and representation of a new structure for polypyrrole-chitosan nanocomposite and investigation of effect of intermolecular interaction. *Synthetic Met* **2014,** *197*, 154-158.

66. Guan, L. H.; Shi, Z. J.; Li, M. X.; Gu, Z. N., Ferrocene-filled single-walled carbon nanotubes. *Carbon* **2005,** *43* (13), 2780-2785.

67. (a) Wittstock, G.; Emons, H.; Heineman, W. R., Electron transfer through an immunoglobulin layer via an immobilized redox mediator. *Electroanal* **1996,** *8* (2), 143-146; (b) Turkmen, E.; Bas, S. Z.; Gulce, H.; Yildiz, S., Glucose biosensor based on immobilization of

glucose oxidase in electropolymerized poly(o-phenylenediamine) film on platinum nanoparticles-polyvinylferrocenium modified electrode. *Electrochim Acta* **2014,** *123*, 93-102.

68. Zhu, Y.; Li, N.; Lv, T.; Yao, Y.; Peng, H.; Shi, J.; Cao, S.; Chen, T., Ag-Doped PEDOT:PSS/CNT composites for thin-film all-solid-state supercapacitors with a stretchability of 480%. *J Mater Chem A* **2018,** *6* (3), 941-947.

69. Edberg, J.; Inganas, O.; Engquist, I.; Berggren, M., Boosting the capacity of all-organic paper supercapacitors using wood derivatives. *J Mater Chem A* **2018,** *6* (1), 145-152.

70. He, W.; Wang, C.; Zhuge, F.; Deng, X.; Xu, X.; Zhai, T., Flexible and high energy density asymmetrical supercapacitors based on core/shell conducting polymer nanowires/manganese dioxide nanoflakes. *Nano Energy* **2017,** *35*, 242-250.

71. Potphode, D. D.; Mishra, S. P.; Sivaraman, P.; Patri, M., Asymmetric supercapacitor devices based on dendritic conducting polymer and activated carbon. *Electrochim Acta* **2017,** *230*, 29-38.

72. Huang, M.; Li, F.; Zhao, X. L.; Luo, D.; You, X. Q.; Zhang, Y. X.; Li, G., Hierarchical ZnO@MnO2 Core-Shell Pillar Arrays on Ni Foam for Binder-Free Supercapacitor Electrodes. *Electrochim Acta* **2015,** *152*, 172-177.

73. Krishnan, S. G.; Reddy, M. V.; Harilal, M.; Vidyadharan, B.; Misnon, I.; Ab Rahim, M. H.; Ismail, J.; Jose, R., Characterization of MgCo2O4 as an electrode for high performance supercapacitors. *Electrochim Acta* **2015,** *161*, 312-321.

74. Gao, F.; Shao, G. H.; Qu, J. Y.; Lv, S. Y.; Li, Y. Q.; Wu, M. B., Tailoring of porous and nitrogen-rich carbons derived from hydrochar for high-performance supercapacitor electrodes. *Electrochim Acta* **2015,** *155*, 201-208.

75. Kim, M.; Kim, J., Redox Deposition of Birnessite-Type Manganese Oxide on Silicon Carbide Microspheres for Use as Supercapacitor Electrodes. *Acs Applied Materials & Interfaces* **2014,** *6* (12), 9036-9045.

76. Yao, W.; Wang, J.; Li, H.; Lu, Y., Flexible alpha-MnO2 paper formed by millimeter-long nanowires for supercapacitor electrodes. *J Power Sources* **2014,** *247*, 824-830.

77. Deng, J. C.; Kang, L. T.; Bai, G. L.; Li, Y.; Li, P. Y.; Liu, X. G.; Yang, Y. Z.; Gao, F.; Liang, W., Solution combustion synthesis of cobalt oxides (Co3O4 and Co3O4/CoO) nanoparticles as supercapacitor electrode materials. *Electrochim Acta* **2014,** *132*, 127-135.

78. Zhu, J.; Tang, S. C.; Xie, H.; Dai, Y. M.; Meng, X. K., Hierarchically Porous MnO2 Microspheres Doped with Homogeneously Distributed Fe3O4 Nanoparticles for Supercapacitors. *Acs Applied Materials & Interfaces* **2014,** *6* (20), 17637-17646.

79. Hou, S. C.; Zhang, G. H.; Zeng, W.; Zhu, J.; Gong, F. L.; Li, F.; Duan, H. G., Hierarchical Core-Shell Structure of ZnO Nanorod@NiO/MoO2 Composite Nanosheet Arrays for High-Performance Supercapacitors. *Acs Applied Materials & Interfaces* **2014,** *6* (16), 13564-13570.

80. Chen, M. X.; Wang, H.; Li, L. Z.; Zhang, Z.; Wang, C.; Liu, Y.; Wang, W.; Gao, J. P., Novel and Facile Method, Dynamic Self-Assemble, To Prepare SnO2/rGO Droplet Aerogel with Complex Morphologies and Their Application in Supercapacitors. *Acs Applied Materials & Interfaces* **2014,** *6* (16), 14327-14337.

81. Foo, C. Y.; Sumboja, A.; Tan, D. J. H.; Wang, J. X.; Lee, P. S., Flexible and Highly Scalable V2O5-rGO Electrodes in an Organic Electrolyte for Supercapacitor Devices. *Advanced Energy Materials* **2014,** *4* (12).

82. Ramasamy, K.; Gupta, R. K.; Palchoudhury, S.; Ivanov, S.; Gupta, A., Layer-Structured Copper Antimony Chalcogenides (CuSbSexS2-x): Stable Electrode Materials for Supercapacitors. *Chem Mater* **2015,** *27* (1), 379-386.

83. Tian, W.; Mao, X.; Brown, P.; Rutledge, G. C.; Hatton, T. A., Electrochemically Nanostructured Polyvinylferrocene/Polypyrrole Hybrids with Synergy for Energy Storage. *Adv Funct Mater* **2015,** *25* (30), 4803-4813.

84. Yuan, X. X.; Ding, X. L.; Wang, C. Y.; Ma, Z. F., Use of polypyrrole in catalysts for low temperature fuel cells. *Energ Environ Sci* **2013,** *6* (4), 1105-1124.

85. Rodenas, T.; Luz, I.; Prieto, G.; Seoane, B.; Miro, H.; Corma, A.; Kapteijn, F.; Llabrés i Xamena, F. X.; Gascon, J., Metal–organic framework nanosheets in polymer composite materials for gas separation. *Nature Materials* **2014,** *14*, 48.

86. Wen, L.; Xu, R.; Mi, Y.; Lei, Y., Multiple nanostructures based on anodized aluminium oxide templates. *Nature Nanotechnology* **2016,** *12*, 244.

87. (a) Dubal, D. P.; Caban-Huertas, Z.; Holze, R.; Gomez-Romero, P., Growth of polypyrrole nanostructures through reactive templates for energy storage applications. *Electrochim Acta* **2016,** *191*, 346-354; (b) Yanai, N.; Uemura, T.; Ohba, M.; Kadowaki, Y.; Maesato, M.; Takenaka, M.; Nishitsuji, S.; Hasegawa, H.; Kitagawa, S., Fabrication of Two-Dimensional Polymer Arrays: Template Synthesis of Polypyrrole between Redox-Active Coordination Nanoslits. *Angew Chem Int Edit* **2008,** *47* (51), 9883-9886.

88. Tong, G.; Guan, J.; Zhang, Q., In Situ Generated Gas Bubble-Directed Self-Assembly: Synthesis, and Peculiar Magnetic and Electrochemical Properties of Vertically Aligned Arrays of High-Density Co3O4 Nanotubes. *Adv Funct Mater* **2013,** *23* (19), 2406-2414.

89. (a) Lu, G.; Li, C.; Shi, G., Polypyrrole micro- and nanowires synthesized by electrochemical polymerization of pyrrole in the aqueous solutions of pyrenesulfonic acid. *Polymer* **2006,** *47* (6), 1778-1784; (b) Wei, Z.; Wan, M., Hollow Microspheres of Polyaniline Synthesized with an Aniline Emulsion Template. *Adv Mater* **2002,** *14* (18), 1314-1317; (c) Ahn, K.-J.; Lee, Y.; Choi, H.; Kim, M.-S.; Im, K.; Noh, S.; Yoon, H., Surfactant-Templated Synthesis of Polypyrrole Nanocages as Redox Mediators for Efficient Energy Storage. *Scientific Reports* **2015,** *5*, 14097.

90. (a) Qu, L.; Shi, G.; Chen, F. e.; Zhang, J., Electrochemical Growth of Polypyrrole Microcontainers. *Macromolecules* **2003,** *36* (4), 1063-1067; (b) Qu, L.; Shi, G.; Yuan, J.; Han, G.; Chen, F. e., Preparation of polypyrrole microstructures by direct electrochemical oxidation of pyrrole in an aqueous solution of camphorsulfonic acid. *Journal of Electroanalytical Chemistry* **2004,** *561*, 149-156; (c) Qu, L.; Shi, G., Hollow microstructures of polypyrrole doped by poly(styrene sulfonic acid). *Journal of Polymer Science Part A: Polymer Chemistry* **2004,** *42* (13), 3170-3177.

91. Koizumi, Y.; Shida, N.; Ohira, M.; Nishiyama, H.; Tomita, I.; Inagi, S., Electropolymerization on wireless electrodes towards conducting polymer microfibre networks. *Nature Communications* **2016,** *7*, 10404.

92. Bae, W. J.; Kim, K. H.; Jo, W. H.; Park, Y. H., A Water-Soluble and Self-Doped Conducting Polypyrrole Graft Copolymer. *Macromolecules* **2005,** *38* (4), 1044-1047.

93. Nabid, M. R.; Entezami, A. A., A novel method for synthesis of water-soluble polypyrrole with horseradish peroxidase enzyme. *J Appl Polym Sci* **2004,** *94* (1), 254-258.

94. Kamide, K.; Iijima, H.; Matsuda, S., Thermodynamics of Formation of Porous Polymeric Membrane by Phase Separation Method I. Nucleation and Growth of Nuclei. *Polymer Journal* **1993,** *25*, 1113.

95. (a) Azzaroni, O.; Schilardi, P. L.; Salvarezza, R. C.; Arvia, A. J., Smoothening Mechanism of Thiourea on Silver Electrodeposition. Real Time Imaging of the Growth Front Evolution. *Langmuir* **1999,** *15* (4), 1508-1514; (b) Yang, T.; Han, Y., Quantitatively Relating Diffusion and Reaction for Shaping Particles. *Crystal Growth & Design* **2016,** *16* (5), 2850-2859; (c) Libbrecht, K. G.; Tanusheva, V. M., Electrically Induced Morphological Instabilities in Free Dendrite Growth. *Physical Review Letters* **1998,** *81* (1), 176-179.

96. Wang, M.; Yin, X.-B.; Vekilov, P. G.; Peng, R.-W.; Ming, N.-B., Intrinsic instability of the concentration field in diffusion-limited growth and its effect on crystallization. *Physical Review E* **1999,** *60* (2), 1901-1905.

97. (a) Kaufman, J. H.; Melroy, O. R.; Abraham, F. F.; Nazzal, A. I., Growth instability in diffusion controlled polymerization. *Solid State Communications* **1986,** *60* (9), 757-761; (b) Sato, K.; Oaki, Y.; Imai, H., Phase separation of composite materials through simultaneous polymerization and crystallization. *Npg Asia Materials* **2017,** *9*, e377; (c) Kaufman, J. H.; Nazzal, A. I.; Melroy, O. R.; Kapitulnik, A., Onset of fractal growth: Statics and dynamics of diffusion-controlled polymerization. *Physical Review B* **1987,** *35* (4), 1881-1890.

98. Goeppert, A.; Czaun, M.; May, R. B.; Prakash, G. K. S.; Olah, G. A.; Narayanan, S. R., Carbon Dioxide Capture from the Air Using a Polyamine Based Regenerable Solid Adsorbent. *Journal of the American Chemical Society* **2011,** *133* (50), 20164-20167.

99. (a) Hughes, M.; Chen, G. Z.; Shaffer, M. S. P.; Fray, D. J.; Windle, A. H., Electrochemical Capacitance of a Nanoporous Composite of Carbon Nanotubes and Polypyrrole. *Chem Mater* **2002,** *14* (4), 1610-1613; (b) El-Kady, M. F.; Strong, V.; Dubin, S.; Kaner, R. B., Laser Scribing of High-Performance and Flexible Graphene-Based Electrochemical Capacitors. *Science* **2012,** *335* (6074), 1326-1330.

100. (a) Park, J. S.; Ikeda, K., Variations of formaldehyde and VOC levels during 3 years in new and older homes. *Indoor Air* **2006,** *16* (2), 129-135; (b) Ochs, S. d. M.; Furtado, L. d. A.; Cerqueira, W. V.; Pereira Netto, A. D., Characterization of the variation of carbonyl compounds concentrations before, during, and after the renovation of an apartment at Niterói, Brazil. *Environmental Science and Pollution Research* **2016,** *23* (15), 15605-15615; (c) Missia, D. A.; Demetriou, E.; Michael, N.; Tolis, E. I.; Bartzis, J. G., Indoor exposure from building materials: A field study. *Atmospheric Environment* **2010,** *44* (35), 4388-4395.

101. (a) Yang, C.-H.; Wender, S. H., Identification of aromatic aldehydes in cigarette smoke and in tobacco. *Phytochemistry* **1964,** *3* (1), 17-22; (b) Hoberman, H. D.; George, R. C. S.,

Reaction of tobacco smoke aldehydes with human hemoglobin. *Journal of Biochemical Toxicology* **1988,** *3* (2), 105-119.

102. (a) Van Hoof, F.; Janssens, J.; Van Dijck, H., Formation of linear aldehydes during surface water preozonization and their removal in water treatment in relation to mutagenic activity and sum parameters. *Science of The Total Environment* **1985,** *47* (Supplement C), 187-194; (b) Liu, C.; Tang, X.; Kim, J.; Korshin, G. V., Formation of aldehydes and carboxylic acids in ozonated surface water and wastewater: A clear relationship with fluorescence changes. *Chemosphere* **2015,** *125* (Supplement C), 182-190; (c) Dąbrowska, A.; Nawrocki, J.; Szeląg-Wasielewska, E., Appearance of aldehydes in the surface layer of lake waters. *Environmental Monitoring and Assessment* **2014,** *186* (7), 4569-4580.

103. (a) Schauer, J. J.; Kleeman, M. J.; Cass, G. R.; Simoneit, B. R. T., Measurement of Emissions from Air Pollution Sources. 3. C1−C29 Organic Compounds from Fireplace Combustion of Wood. *Environmental Science & Technology* **2001,** *35* (9), 1716-1728; (b) Altemose, B.; Gong, J.; Zhu, T.; Hu, M.; Zhang, L.; Cheng, H.; Zhang, L.; Tong, J.; Kipen, H. M.; Strickland, P. O.; Meng, Q.; Robson, M. G.; Zhang, J., Aldehydes in Relation to Air Pollution Sources: A Case Study around the Beijing Olympics. *Atmospheric environment (Oxford, England : 1994)* **2015,** *109*, 61-69.

104. (a) Altshuller, A. P., Production of aldehydes as primary emissions and from secondary atmospheric reactions of alkenes and alkanes during the night and early morning hours. *Atmospheric Environment. Part A. General Topics* **1993,** *27* (1), 21-32; (b) Lin, Y. C.; Schwab, J. J.; Demerjian, K. L.; Bae, M.-S.; Chen, W.-N.; Sun, Y.; Zhang, Q.; Hung, H.-M.; Perry, J., Summertime formaldehyde observations in New York City: Ambient levels, sources and its contribution to HOx radicals. *Journal of Geophysical Research: Atmospheres* **2012,** *117* (D8), n/a-n/a.

105. Millar, J. D., Carcinogenicty of Acetaldehyde and Malonaldehyde, and Mutagenicity of Related Low-Molecular-Weight Aldehydes. Control, C. f. D., Ed. National Institute for Occupational Safety and Health, Centers for Disease Control: Current Intelligence Bulletins, 1991; Vol. 55.

106. Antwi-Boampong, S.; BelBruno, J. J., Detection of formaldehyde vapor using conductive polymer films. *Sensors and Actuators B: Chemical* **2013,** *182*, 300-306.

107. (a) Zheng, W.; Razal, J. M.; Spinks, G. M.; Truong, V.-T.; Whitten, P. G.; Wallace, G. G., The Role of Unbound Oligomers in the Nucleation and Growth of Electrodeposited Polypyrrole and Method for Preparing High Strength, High Conductivity Films. *Langmuir* **2012,** *28* (29), 10891-10897; (b) Hwang, B. J.; Santhanam, R.; Lin, Y. L., Nucleation and Growth Mechanism of Electropolymerization of Polypyrrole on Gold/Highly Oriented Pyrolytic Graphite Electrode. *J Electrochem Soc* **2000,** *147* (6), 2252-2257.

108. Asavapiriyanont, S.; Chandler, G. K.; Gunawardena, G. A.; Pletcher, D., The electrodeposition of polypyrrole films from aqueous solutions. *Journal of Electroanalytical Chemistry and Interfacial Electrochemistry* **1984,** *177* (1), 229-244.

109. Yu, J. G.; Le, Y.; Cheng, B., Fabrication and CO2 adsorption performance of bimodal porous silica hollow spheres with amine-modified surfaces. *Rsc Adv* **2012,** *2* (17), 6784-6791.

110. Thordarson, P., Determining association constants from titration experiments in supramolecular chemistry. *Chem Soc Rev* **2011,** *40* (3), 1305-1323.

111. Agnes, M.; Nitti, A.; Vander Griend, D. A.; Dondi, D.; Merli, D.; Pasini, D., A chiroptical molecular sensor for ferrocene. *Chemical Communications* **2016,** *52* (77), 11492-11495.

112. (a) Yamamoto, K.; Imaoka, T.; Chun, W.-J.; Enoki, O.; Katoh, H.; Takenaga, M.; Sonoi, A., Size-specific catalytic activity of platinum clusters enhances oxygen reduction reactions. *Nature Chemistry* **2009,** *1*, 397; (b) Bai, Y. C.; Wu, F. C.; Liu, C. Q.; Li, W.; Guo, J. Y.; Fu, P. Q.; Xing, B. S.; Zheng, J., Ultraviolet absorbance titration for determining stability constants of humic substances with Cu(II) and Hg(II). *Anal Chim Acta* **2008,** *616* (1), 115-121.

113. Bhattacharya, S.; Mandal, S. S., Interaction of surfactants with DNA. Role of hydrophobicity and surface charge on intercalation and DNA melting. *Biochimica et Biophysica Acta (BBA) - Biomembranes* **1997,** *1323* (1), 29-44.

114. Pan, X.; Wang, G.; Lay, C. L.; Tan, B. H.; He, C.; Liu, Y., Photoluminescence from Amino-Containing Polymer in the Presence of CO2: Carbamato Anion Formed as a Fluorophore. **2013,** *3*, 2763.

115. (a) Schmidt, E.; Zhang, H.; Chang, C. K.; Babcock, G. T.; Oertling, W. A., Room Temperature Binding of CO to Cobaltous Porphyrin π Cation Radical: Spectroscopic Characterization of Mono and Bis CO Complexes with Cobaltic Porphyrin. *Journal of the American Chemical Society* **1996,** *118* (12), 2954-2961; (b) Yamamoto, K.; Higuchi, M.; Shiki, S.; Tsuruta, M.; Chiba, H., Stepwise radial complexation of imine groups in phenylazomethine dendrimers. *Nature* **2002,** *415*, 509; (c) Kim, J.; Swager, T. M., Control of conformational and interpolymer effects in conjugated polymers. *Nature* **2001,** *411*, 1030.

116. (a) Shetty, A. S.; Zhang, J.; Moore, J. S., Aromatic π-Stacking in Solution as Revealed through the Aggregation of Phenylacetylene Macrocycles. *Journal of the American Chemical Society* **1996,** *118* (5), 1019-1027; (b) Yajima, T.; Maccarrone, G.; Takani, M.; Contino, A.; Arena, G.; Takamido, R.; Hanaki, M.; Funahashi, Y.; Odani, A.; Yamauchi, O., Combined Effects of Electrostatic and π–π Stacking Interactions: Selective Binding of Nucleotides and Aromatic Carboxylates by Platinum(II)–Aromatic Ligand Complexes. *Chemistry – A European Journal* **2003,** *9* (14), 3341-3352.

117. Crank, J., *The mathematics of diffusion*. 2nd ed.; Clarendon Press: Oxford, 1975; p 414.

118. Wilke, C. R.; Chang, P., Correlation of diffusion coefficients in dilute solutions. *AIChE Journal* **1955,** *1* (2), 264-270.

119. Deen, W. M., *Analysis of Transport Phenomena*. Oxford University Press, Inc.: New York, 2012; p 664.

120. Crowell, E. P.; Powell, W. A.; Varsel, C. J., Characterization and Determination of Aldehydes by the Ultraviolet Spectral Changes Resulting from Acetal Formation. *Analytical Chemistry* **1963,** *35* (2), 184-189.

121. Mao, X. W.; Simeon, F.; Achilleos, D. S.; Rutledge, G. C.; Hatton, T. A., Metallocene/carbon hybrids prepared by a solution process for supercapacitor applications. *J Mater Chem A* **2013,** *1* (42), 13120-13127.

122. Medany, S. S.; Ismail, K. M.; Badawy, W. A., Kinetics of the electropolymerization of aminoanthraquinone from aqueous solutions and analytical applications of the polymer film. *Journal of Advanced Research* **2012,** *3* (3), 261-268.

123. Allen J. Bard, L. R. F., *Electrochemical Methods: Fundamentals and Applications*. 2nd ed.; John Wiley & Sons, INC.: 2001.

124. Zheng, M.; Jagota, A.; Semke, E. D.; Diner, B. A.; McLean, R. S.; Lustig, S. R.; Richardson, R. E.; Tassi, N. G., DNA-assisted dispersion and separation of carbon nanotubes. *Nature Materials* **2003,** *2*, 338.

125. Clark, K. D.; Nacham, O.; Yu, H.; Li, T.; Yamsek, M. M.; Ronning, D. R.; Anderson, J. L., Extraction of DNA by Magnetic Ionic Liquids: Tunable Solvents for Rapid and Selective DNA Analysis. *Analytical Chemistry* **2015,** *87* (3), 1552-1559.

126. Luo, X.; Cui, X. T., Electrochemically controlled release based on nanoporous conducting polymers. *Electrochemistry Communications* **2009,** *11* (2), 402-404.

127. Wang, X.; Gu, X.; Yuan, C.; Chen, S.; Zhang, P.; Zhang, T.; Yao, J.; Chen, F.; Chen, G., Evaluation of biocompatibility of polypyrrole in vitro and in vivo. *Journal of Biomedical Materials Research Part A* **2004,** *68A* (3), 411-422.

128. (a) Yousef Elahi, M.; Bathaie, S. Z.; Kazemi, S. H.; Mousavi, M. F., DNA immobilization on a polypyrrole nanofiber modified electrode and its interaction with salicylic acid/aspirin. *Analytical Biochemistry* **2011,** *411* (2), 176-184; (b) Qiu, Y.-J.; Reynolds, J. R., Dopant anion controlled ion transport behavior of polypyrrole. *Polymer Engineering & Science* **1991,** *31* (6), 417-421; (c) Ren, X.; Pickup, P. G., Ion transport in polypyrrole and a polypyrrole/polyanion composite. *The Journal of Physical Chemistry* **1993,** *97* (20), 5356-5362.

129. Radi, A.-E.; Eissa, A.; Nassef, H. M., Voltammetric and spectroscopic studies on the binding of the antitumor drug dacarbazine with DNA. *Journal of Electroanalytical Chemistry* **2014,** *717-718* (Supplement C), 24-28.

130. (a) Qian, T.; Zhou, X.; Yu, C.; Wu, S.; Shen, J., Highly dispersed carbon nanotube/polypyrrole core/shell composites with improved electrochemical capacitive performance. *J Mater Chem A* **2013,** *1* (48), 15230-15234; (b) Qian, T.; Yu, C.; Wu, S.; Shen, J., In situ polymerization of highly dispersed polypyrrole on reduced graphite oxide for dopamine detection. *Biosensors and Bioelectronics* **2013,** *50* (Supplement C), 157-160.

131. Almaqwashi, A. A.; Paramanathan, T.; Rouzina, I.; Williams, M. C., Mechanisms of small molecule–DNA interactions probed by single-molecule force spectroscopy. *Nucleic Acids Research* **2016,** *44* (9), 3971-3988.

132. Carter, M. T.; Rodriguez, M.; Bard, A. J., Voltammetric studies of the interaction of metal chelates with DNA. 2. Tris-chelated complexes of cobalt(III) and iron(II) with 1,10-phenanthroline and 2,2'-bipyridine. *Journal of the American Chemical Society* **1989,** *111* (24), 8901-8911.

133. Dang, X.-J.; Nie, M.-Y.; Tong, J.; Li, H.-L., Inclusion of the parent molecules of some drugs with β-cyclodextrin studied by electrochemical and spectrometric methods. *Journal of Electroanalytical Chemistry* **1998,** *448* (1), 61-67.

134. Saoudi, B.; Despas, C.; Chehimi, M. M.; Jammul, N.; Delamar, M.; Bessière, J.; Walcarius, A., Study of DNA adsorption on polypyrrole: interest of dielectric monitoring. *Sensors and Actuators B: Chemical* **2000,** *62* (1), 35-42.

135. (a) Ibrahim, M. S.; Shehatta, I. S.; Al-Nayeli, A. A., Voltammetric studies of the interaction of lumazine with cyclodextrins and DNA. *Journal of Pharmaceutical and Biomedical Analysis* **2002,** *28* (2), 217-225; (b) Lal, B.; Badshah, A.; Altaf, A. A.; Tahir, M. N.; Ullah, S.; Huq, F., Synthesis, characterization and antitumor activity of new ferrocene incorporated N,N[prime or minute]-disubstituted thioureas. *Dalton Transactions* **2012,** *41* (48), 14643-14650; (c) Altaf, A. A.; Hashmat, U.; Yousaf, M.; Lal, B.; Ullah, S.; Holder, A. A.; Badshah, A., Synthesis and characterization of azo-guanidine based alcoholic media naked eye DNA sensor. *Royal Society Open Science* **2016,** *3* (11); (d) Zhao, G.-C.; Zhu, J.-J.; Zhang, J.-J.; Chen, H.-Y., Voltammetric studies of the interaction of methylene blue with DNA by means of β-cyclodextrin. *Anal Chim Acta* **1999,** *394* (2), 337-344.

136. Melzak, K. A.; Sherwood, C. S.; Turner, R. F. B.; Haynes, C. A., Driving Forces for DNA Adsorption to Silica in Perchlorate Solutions. *Journal of Colloid and Interface Science* **1996,** *181* (2), 635-644.

137. Biebricher, A. S.; Heller, I.; Roijmans, R. F. H.; Hoekstra, T. P.; Peterman, E. J. G.; Wuite, G. J. L., The impact of DNA intercalators on DNA and DNA-processing enzymes elucidated through force-dependent binding kinetics. *Nature Communications* **2015,** *6*, 7304.

138. Wang, J.; Lopez Paz, J. L.; Jiang, M., Probing the Barrier Properties of Self-Assembled Monolayers Using Flow Amperometry. *Langmuir* **1999,** *15* (5), 1884-1886.

139. Wang, J.; Rivas, G.; Jiang, M.; Zhang, X., Electrochemically Induced Release of DNA from Gold Ultramicroelectrodes. *Langmuir* **1999,** *15* (19), 6541-6545.

140. Patolsky, F.; Katz, E.; Bardea, A.; Willner, I., Enzyme-Linked Amplified Electrochemical Sensing of Oligonucleotide−DNA Interactions by Means of the Precipitation of an Insoluble Product and Using Impedance Spectroscopy. *Langmuir* **1999,** *15* (11), 3703-3706.

141. (a) Tiwari, I.; Gupta, M.; Pandey, C. M.; Mishra, V., Gold nanoparticle decorated graphene sheet-polypyrrole based nanocomposite: its synthesis, characterization and genosensing application. *Dalton Transactions* **2015,** *44* (35), 15557-15566; (b) Maeda, M.; Mitsuhashi, Y.; Nakano, K.; Takagi, M., DNA-Immobilized Gold Electrode for DNA-Binding Drug Sensor. *Analytical Sciences* **1992,** *8* (1), 83-84; (c) Degefa, T. H.; Kwak, J., Electrochemical impedance sensing of DNA at PNA self assembled monolayer. *Journal of Electroanalytical Chemistry* **2008,** *612* (1), 37-41; (d) Mehdinia, A.; Habib Kazemi, S.; Zahra Bathaie, S.; Alizadeh, A.; Shamsipur, M.; Mousavi, M. F., Electrochemical studies of DNA immobilization onto the azide-terminated monolayers and its interaction with taxol. *Analytical Biochemistry* **2008,** *375* (2), 331-338.

142. (a) Lee, H.-M.; Chan, D. S.-H.; Yang, F.; Lam, H.-Y.; Yan, S.-C.; Che, C.-M.; Ma, D.-L.; Leung, C.-H., Identification of natural product Fonsecin B as a stabilizing ligand of c-myc G-quadruplex DNA by high-throughput virtual screening. *Chemical Communications* **2010,** *46* (26), 4680-4682; (b) Evans, G. A., Molecular cloning: A laboratory manual. Second edition. Volumes 1, 2, and 3. Current protocols in molecular biology. Volumes 1 and 2. *Cell 61* (1), 17-18.

143. Marmur, J., A procedure for the isolation of deoxyribonucleic acid from micro-organisms. *Journal of Molecular Biology* **1961,** *3* (2), 208-IN1.

144. Zhang, L.; Aboagye, A.; Kelkar, A.; Lai, C.; Fong, H., A review: carbon nanofibers from electrospun polyacrylonitrile and their applications. *Journal of Materials Science* **2014,** *49* (2), 463-480.

145. (a) Mao, X.; Yang, X.; Rutledge, G. C.; Alan Hatton, T., Ultra-Wide-Range Electrochemical Sensing Using Continuous Electrospun Carbon Nanofibers with High Densities of States. *ACS Applied Materials & Interfaces* **2014,** *6* (5), 3394-3405; (b) Mao, X.; Simeon, F.; Rutledge, G. C.; Hatton, T. A., Electrospun Carbon Nanofiber Webs with Controlled Density of States for Sensor Applications. *Adv Mater* **2013,** *25* (9), 1309-1314.

146. Wu, Z.; Pan, D.; Fan, X.; Qian, B., Thermal shrinkage behavior of preoxidized polyacrylonitrile fibers during carbonization. *J Appl Polym Sci* **1987,** *33* (8), 2877-2884.

147. (a) Ma, X.; Yuan, C.; Liu, X., Mechanical, Microstructure and Surface Characterizations of Carbon Fibers Prepared from Cellulose after Liquefying and Curing. *Materials* **2014,** *7* (1), 75; (b) Fei, J.; Luo, W.; Huang, J.; Ouyang, H.; Wang, H.; Cao, L., Effect of hydrothermal modified carbon fiber through Diels-Alder reaction and its reinforced phenolic composites. *Rsc Adv* **2015,** *5* (79), 64450-64455; (c) Li, J.; Vergne, M. J.; Mowles, E. D.; Zhong, W.-H.; Hercules, D. M.; Lukehart, C. M., Surface functionalization and characterization of graphitic carbon nanofibers (GCNFs). *Carbon* **2005,** *43* (14), 2883-2893.

148. Kim, G. T.; Ahn, Y. C.; Lee, J. K., Characteristics of Nylon 6 nanofilter for removing ultra fine particles. *Korean Journal of Chemical Engineering* **2008,** *25* (2), 368-372.

149. Sakai, K.; Iwamura, S.; Sumida, R.; Ogino, I.; Mukai, S. R., Carbon Paper with a High Surface Area Prepared from Carbon Nanofibers Obtained through the Liquid Pulse Injection Technique. *ACS Omega* **2018,** *3* (1), 691-697.